



UNIVERSITÀ DEGLI STUDI DI TRIESTE
e
UNIVERSITÀ CA' FOSCARI DI VENEZIA

XXXII CICLO DEL DOTTORATO DI RICERCA IN
CHIMICA

METAL NANOSTRUCTURES DECORATED WITH
SILVER NANOSTARS: A NOVEL HIGHLY
EFFICIENT SERS SUBSTRATE FOR DYES AND
PIGMENTS DETECTION

Settore scientifico-disciplinare: **CHIM/01**

DOTTORANDA
MARIA SOLE ZALAFFI

Maria Sole Zalaffi

COORDINATORE
PROF. BARBARA MILANI

Barbara Milani

SUPERVISORE DI TESI
PROF. PAOLO UGO

Paolo Ugo

ANNO ACCADEMICO 2018/2019

Abstract

The detection of artistic molecules such as dyes and/or pictorial binders employed in the field of Cultural Heritage requires more and more sensitive techniques. The surface enhanced Raman spectroscopy (SERS) represents a valuable option due to its ability to reveal molecules adsorbed or bound onto nanostructured interfaces. In order to maximize the enhancement of the Raman effect, different Ag and Au nanomaterials were bound together to produce hierarchical structures. In particular, silver nanostars (AgNSs) were chosen because of the strong enhancement caused by their anisotropic shape and they were prepared by one-pot chemical synthesis. The AgNSs were used to decorate two different gold nanostructures, namely Au nanowires (AuNWs) and sphere segment void (SSV) structured surfaces. The AuNWs were obtained in the shape of ensembles of nanoelectrodes by templated electroless deposition in nanoporous membranes while the SSV substrates were prepared via gold electrodeposition by using a monolayer of polystyrene spheres as template.

The enhancement of the Raman effect was tested at first through the employment of benzenethiol, a well known Raman probe. Thereafter, cochineal lake, in particular, was chosen as target owing to its use throughout the history of art. Lakes are complex coloring pigments in which an organic dye (e.g. cochineal, madder or kermes) is adsorbed onto solid particles of inorganic salts. This composite structure, composed by an organic molecule chelated by metallic ions, makes the Raman detection of lakes extremely challenging. However, the described issue is overcome by employing highly sensitive SERS substrates as those prepared in the context of this thesis.

We compared the magnitude of the enhancements obtained with different SERS substrates: standing alone AgNSs, AuNWs ensembles and SSV substrates and hierarchical nanostructures composed by AgNSs combined to AuNWs (AgNSs@AuNWs) (Figure α -a) and to SSV substrates (AgNSs@SSV) (Figure α -b). Particularly strong enhancements were recorded in the case of the

AgNSs@SSV substrates, showing the high potential of the so called particle-in-cavity (PIC) architecture. Concluding, we synthesized highly effective hierarchical nanostructures whose future employment lies in the production of extremely sensitive SERS biosensors to be applied in the detection of artistic dyes and binders.

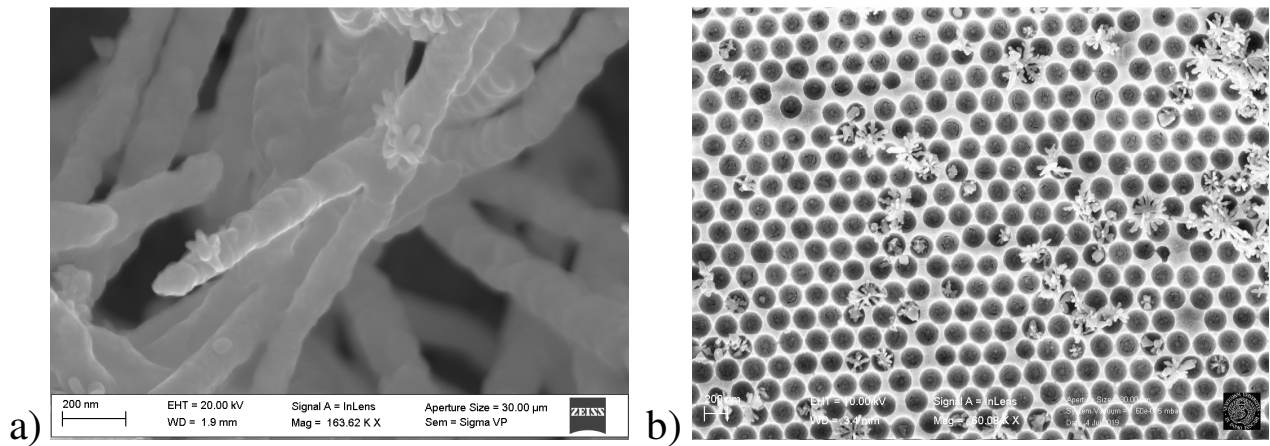


Figure a Field emission - scanning electron microscopy pictures of AgNSs a) bound to a AuNWs ensemble and b) hosted inside the cavities of an SSV substrate.

Abbreviations

AgNSs: silver nanostars

AgNPs: silver nanospheres

AuNWs: gold nanowires

BEM: boundary element method

BT: benzenethiol

CA: carminic acid

CE: counter electrode

CL: cochineal lake-pigment

CS: cross-section

CTAB: cetyl-trimethylammonium bromide

CuNWs: copper nanowires

DCM: dichloromethane

DLS: dynamic light scattering

DMF: dimethylformamide

EC-SERS: electrochemical – surface enhanced Raman spectroscopy

EM: electromagnetic

EDS: energy dispersive spectroscopy

FE-SEM: field emission scanning electron microscopy

GC: glassy carbon

GC-MS: gas chromatography - mass spectrometry

Glu: glucose

HOMO: highest occupied molecular orbital

HPLC-DAD: high pressure liquid chromatography – diode-array detector

HRP: horseradish peroxidase

HV: high voltage

IR: infrared

LFIEF: local field enhancement factor

LFIA: lateral flow immunoassay

LSPR: local surface plasmon resonance

LUMO: lowest unoccupied molecular orbital

NEE: nanoelctrodes ensemble

NPs: nanoparticles

Raman/SERS bands: s = strong; m = medium; w = weak; sh = shoulder; br = broad

RE: reference electrode

REF: Raman enhancement factor

RF: radio frequency

SEM: scanning electron microscopy

SERS: surface enhanced Raman spectroscopy/scattering

SR: signal ratios

SSV: sphere segment void

PB: pigment blue

PC: polycarbonate

PVP: polyvinylpyrrolidone

TEM: transmission electron microscopy

TLC: thin layer chromatography

UV: ultraviolet

Vis: visible

WD: working distance

WE: working electrode

XRF: X-ray fluorescence spectroscopy

Index

• Aims of the research	1
References.....	3
• Chapter 1- General introduction	6
1.1 SERS: a promising diagnostic technique applied to Cultural Heritage.....	6
1.1.1 Classical Raman spectroscopy vs. SERS.....	9
1.2 Introduction to Raman spectroscopy.....	11
1.2.1 Molecular spectroscopy.....	11
1.2.2 Vibrational spectroscopy.....	11
1.2.3 Raman spectroscopy.....	13
1.3 Surface enhanced Raman spectroscopy	16
1.3.1 Optical properties of metals.....	16
1.3.2 Enhancement of Raman signal and quenching of fluorescence.....	19
1.3.3 Intensification mechanism of the SERS effect.....	21
1.4 Synthesis of nanomaterials: soft and hard template, electroless and electrochemical deposition.....	25
1.4.1 Electroless soft template synthesis of nanoparticles.....	25

1.4.2 Electroless and electrochemical hard template synthesis of high aspect ratio nanomaterials.....	27
1.4.3 Electrochemical hard template synthesis of nanostructured surfaces.....	32
1.5 Hierarchical structures of nanomaterials.....	33
1.6 The application of SERS to Cultural Heritage.....	34
1.6.1 Identification of dyes and lake-pigments.....	34
1.6.2 SERS sensors for the detection of protein-based binders.....	36
References.....	39
• Chapter 2- Preparation of Ag nanostars and first applicative tests..	45
Part A: Preparation of Ag nanostars for SERS measurements.....	45
2.1 Introduction.....	45
2.2 Materials and methods.....	47
2.2.1 Materials.....	47
2.2.2 Synthesis of Ag nanostars.....	47
2.2.3 Synthesis of Ag nanospheres.....	48
2.2.4 Preparation of the samples for the Raman analysis.....	48
2.2.5 Instrumentation.....	48
2.3 Results and discussion.....	50

2.3.1 Synthesis and characterization of AgNSs and AgNPs by UV-Vis spectroscopy, dynamic light scattering and field emission - scanning electron microscopy.....	50
2.3.2 SERS characterization with benzenethiol as Raman probe.....	54
2.3.3 Summary.....	56
Part B: Application of AgNSs: case study.....	56
2.5 Case study: the “ <i>Madonna della Misericordia</i> ” from the National Gallery of Parma.....	56
2.5.1 Introduction.....	56
2.5.2 Materials and methods.....	58
2.5.3 Cross sections analysis.....	59
2.5.4 Conclusions.....	67
References.....	69
• Chapter 3- Hierarchical nanostructures based on Ag nanostars @ Au nanowires for the SERS detection of lake-pigments.....	72
3.1 Introduction.....	72
3.2 Materials and methods.....	74
3.2.1 Materials.....	74
3.2.2 Synthesis of AgNSs and AgNPs.....	74
3.2.3 Membrane templated preparation of AuNWs.....	74
3.2.4 Preparation of the samples for the Raman analysis.....	76
3.2.5 Instrumentation.....	77
3.3 Results and discussion.....	79

3.3.1 Characterization of the AuNWs by UV-Vis spectroscopy and FE-SEM.....	79
3.3.2 Preparation and FE-SEM characterization of AgNPSs@AuNWs hierarchical structures.....	81
3.3.3 Boundary element method simulations.....	82
3.3.4 SERS characterization with benzenethiol as Raman probe.....	84
3.3.5 Application to cochineal lake-pigment detection.....	86
3.4 Conclusions.....	89
References.....	89
• Chapter 4- Hierarchical nanostructures based on Ag nanostars@Cu nanowires (AgNSs@CuNWs).....	93
4.1 Introduction.....	93
4.1.1 Electrochemical template deposition of quasi-monodimensional nanomaterials.....	94
4.2 Materials and methods.....	96
4.2.1 Materials.....	96
4.2.2 Synthesis of AgNSs.....	96
4.2.3 Electrochemical deposition of CuNWs.....	96
4.2.4 Preparation of the samples for the Raman analysis.....	97
4.2.5 Instrumentation.....	98
4.3 Results and discussion.....	99
4.3.1 Voltammetric study of Cu ²⁺ ions reduction.....	99
4.3.2 Optimization of copper nanowires deposition in nanoporous membranes.....	100
4.3.3 SERS on CuNWs and AgNSs@CuNWs substrates.....	104
4.4 Conclusions.....	106

References.....	107
• Chapter 5- Hierarchical nanostructures composed by sphere	
segment void substrates decorated with Ag nanostars.....	109
5.1 Introduction.....	109
5.1.1 SSV substrates.....	109
5.1.2 Particle-in-cavity architectures.....	112
5.2 Materials and methods.....	113
5.2.1 Materials.....	113
5.2.2 Synthesis of AgNSs.....	114
5.2.3 Synthesis of SSV.....	114
5.2.4 Preparation of the samples for the Raman analysis.....	118
5.2.5 Instrumentation.....	120
5.3 Results and discussion.....	121
5.3.1 Characterization of the 600 and 220 nm size SSV substrates with or without AgNSs with FE-SEM.....	121
5.3.2 Evaluation of the Raman enhancement by means of benzenethiol as Raman probe.....	125
5.3.3 Detection of madder lake-pigment.....	126
5.3.4 Detection of cochineal lake-pigment and comparison with pure carminic acid.....	127
5.3.5 Application to indigo.....	129
5.4 Conclusions.....	130
References.....	131

• Chapter 6- Comparison with different nanomaterials.....	134
6.1 Comparison between AgNSs@CuNWs and AgNSs@AuNWs.....	134
6.2 AgNSs@AuNWs vs. AgNs@SSV.....	135
6.3 The performances of 600 and 220 nm SSV.....	137
6.4 Conclusions.....	140
References.....	140
• Chapter 7 - Concluding remarks.....	141
7.1 Final comments and future prospects.....	141
References.....	144
• Appendices	
A - Cochineal lake-pigment.....	146
References.....	148
B - Madonna della Misericordia: visual and non-invasive analyses.....	149
References.....	151
• Acknowledgements	152

Aims of the research

This thesis focuses on the preparation of novel nanostructured substrates and their application as surface enhanced Raman spectroscopy (SERS) sensors for analytical and diagnostics purposes in the Cultural Heritage field. The importance of scientific analyses on works of art has become more and more crucial in the articulate processes of conservation and restoration. Moreover, the complexity of artistic materials, composed by mixed organic and inorganic substances which are often found aged and in minimal quantities, requires extremely sensitive but user friendly analytical tools. For this reason, the request of effective non-invasive or micro-invasive diagnostic strategies has steadily increased. Aims of this research is indeed the preparation of sensitive SERS-based sensors for reliable diagnostics, easily applicable *in situ* or in the laboratory.

SERS [1,2] is a technique which exploits the strong enhancement of the Raman scattering of molecules adsorbed onto metal nanoparticles and nanostructured surfaces. Since the Raman signal can be intensified by several orders of magnitudes, SERS is increasingly employed for the extremely sensitive detection of molecules whose signals are hardly collected by employing the normal Raman technique, reading extremely low concentration levels, down to the single molecule level [3]. Interesting applications and improvements of this technique are nowadays directed towards the development of more sensitive SERS substrates based on metal nanostructures chemically functionalized [4] or hierarchically organized [5,6]. In particular, it was observed that the Raman enhancement generated by spherical nanoparticles (NPs) and other isotropic nanomaterials can be further increased by using nanomaterials with different shapes characterized by anisotropic features [7,8], such as gold sphere segment void nanostructures [9,10] or arrays of macroporous nanostructures produced on bundles of optical fibers [11]. Very high amplification effects have been observed with star-shaped nanostructures [12], including Au [13] and Ag [14,15] nanostars (AgNSs). Moreover, coupling nanomaterials made of different metals in organized

hierarchical nanostructures produces even larger enhancements of the Raman effect [16,17,18], such as in the case of the so called particle-in-cavity architecture [19,20].

The aim of this thesis is the synthesis and optimization of hierarchical nanostructures to be used as improved SERS substrates for Cultural Heritage applications. The here studied structures are composed by two kinds of anisotropic nanomaterials, namely AgNSs bound onto high aspect ratio Au [21,22] or Cu [23] nanowires (Au/CuNWs) and Au macroporous surfaces named sphere segment void surfaces (SSV) [9,10]. The nanomaterials are synthesized separately and then assembled together by cysteamine bridges [24,25]. This bifunctional thiol (Figure β -a) was chosen due to its ability to bind gold by means of its sulphhydryl group and silver with the amine one (Figure β -b).

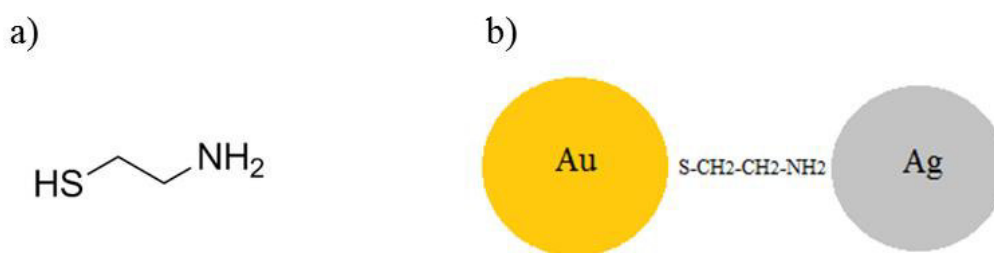


Figure β a) Structural formula of cysteamine and b) scheme showing the interaction between the sulphhydryl function and gold and the amine function with silver.

It is worth to note that this kind of nanostructures is suitable for further functionalization for instance with biochemical receptors such as immunoproteins, in order to eventually develop novel SERS biomolecular sensors [26]. Specific chemical [27] and immunochemical [28] bonds between the functionalized NPs and the analyte can be employed, even in the context of an innovative combination of SERS with a microfluidic approach [29] or thin layer chromatography (TLC) [30].

In the context of this research, a specific class of colorants was chosen as target analytes, namely lake-pigments and, among these, cochineal lake in particular. Lakes are characterized by an intrinsic complexity since they present an organic component (the colorant) fixed onto an inorganic substrate (alum, clay or hydroxides). This presence of mixed organic and inorganic substances is typical of artworks and perfectly display the challenging feature of examining Cultural Heritage materials: samples composed by extremely heterogeneous matrices where the colorants are found in tiny amounts. Besides, even the sampling further complicate the analysis: scratched powders, solvent extracted dyes or binders and transversal microsamples taken by means of scalpel must be the most limited in order to guarantee a proper conservation of the work of art. This is the reason why more and more sensitive analytical techniques are required. SERS-based sensors offer a promising solution to these issues. In the following chapters several experimental strategies will be described, according to specific circumstances: concentrated nanoparticles, applied directly onto cross sections, dispersions of lakes and colorants, mimicking extracted analytes from real samples, were adsorbed onto standing alone or hierarchical structured nanomaterials. In this way, by proposing several analytical protocols which can be customized to case studies, we hope to facilitate the diagnostics of Cultural Heritage which is not trivial at all.

References

- [1] M. Fleischmann, P.J. Hendra, A.J. McQuillan, *Chem. Phys. Lett.* **1974**, 26 (2), 163.
- [2] E.C. Le Ru, E. Blackie, M. Meyer, P.G. Etchegoin, *J. Phys. Chem. C* **2007**, 111 (37), 13794.
- [3] H.M. Lee, S.M. Jin, H.M. Kim, Y.D. Suh, *Phys. Chem. Chem. Phys.* **2013**, 15, 5276.
- [4] L. Litti, N. Rivato, G. Fracasso, P. Bontempi, E. Nicolato, P. Marzola, A. Venzo, M. Colombatti, M. Gobbo, M. Meneghetti, *Nanoscale* **2018**, 10, 1272.
- [5] Y. Zhao, X. Li, Y. Liu, L. Zhang, F. Wang, Y. Lu, *Sens. Actuators B* **2017**, 247, 850.

- [6] W.J. Anderson, K. Nowinska, T. Hutter, S. Mahajan, M. Fischlenchner, *Nanoscale* **2018**, *10*, 7138.
- [7] L. Shao, A.S. Susha, L.S. Cheung, T.K. Sau, A.L. Rogach, J. Wang, *Langmuir* **2012**, *28*, 8979.
- [8] C.G. Khoury, T. Vo-Dinh, *J. Phys. Chem. C* **2008**, *112*, 18849.
- [9] N.G. Tognalli, A. Fainstein, E.J. Calvo, M. Abdelsalam, P.N. Bartlett, *J. Phys. Chem. C* **2012**, *116*, 3414.
- [10] A. Celiktas, M.A. Ghanem, P.N. Bartlett, *J. Electroanal. Chem.* **2012**, *670*, 42.
- [11] M. Zamuner, D. Talaga, F. Deiss, V. Guieu, A. Kuhn, P. Ugo, N. Sojic, *Adv. Funct. Mater.* **2009**, *19 (44)*, 3129.
- [12] P.S. Kumar, I. Pastoriza-Santos, B. Rodriguez-Gonzales, F.J. García de Abajo, L.M. Luis-Marzan, *Nanotechnology* **2007**, *19*, 015606.
- [13] A. Guerrero-Martínez, S. Barbosa, I. Pastoriza-Santos, L.M. Liz-Marzan, *Curr. Opin. Colloid Interface Sci.* **2011**, *16*, 118.
- [14] Y. Wang, P.H.C. Camargo, S.E. Skrabalak, H. Gu, Y. Xia, *Langmuir* **2008**, *24*, 12042.
- [15] A. García-Leis, J.V. García-Ramos, S. Sánchez-Cortés, *J. Phys. Chem. C* **2013**, *117*, 7791.
- [16] X. Guo, Z. Guo, Y. Jin, Z. Liu, W. Zhang, D. Huang, *Microchim. Acta* **2012**, *178*, 229.
- [17] K. Kim, J.K. Yoon, *J. Phys. Chem. B* **2005**, *109*, 20731.
- [18] K. Kwan, H.S. Lee, *J. Phys. Chem. B* **2005**, *109 (40)*, 18929.
- [19] J.D. Speed, R.P. Johnson, J.T. Hugall, N.N. Lal, P.N. Bartlett, J.J. Baumberg, A.E. Russell, *Chem. Commun.* **2011**, *47*, 6335.
- [20] F.M. Huang, D. Wilding, J.D. Speed, A.E. Russell, P.N. Bartlett, J.J. Baumberg, *Nano Lett.* **2011**, *11*, 1221.
- [21] V.P. Menon, C.R. Martin, *Anal. Chem.* **1995**, *67*, 1920.

- [22] P. Ugo, L.M. Moretto, *Template Deposition of Metals*. In C. Zosky (ed.), *Handbook of Electrochemistry*, **2007**, chapter 16.2, Elsevier, Amsterdam, The Netherlands.
- [23] A.M. Stortini, L.M. Moretto, A. Mardegan, M. Ongaro, P. Ugo, *Sens. Actuator B-Chem.* **2015**, *207*, 186.
- [24] J.B. Shein, L.M.H. Lai, P.K. Eggers, M.N. Paddon-Row, J.J. Gooding, *Langmuir* **2009** *25*, 11121.
- [25] M. Silvestrini, P. Ugo, *Anal. Bioanal. Chem.* **2013**, *405*, 995.
- [26] N. Banaei, A. Foley, J.M. Houghton, Y. Sun, B. Kim, *Nanotechnology* **2017**, *28*, 455101.
- [27] L. Litti, A. Ramundo, F. Biscaglia, G. Toffoli, M. Gobbo, M. Meneghetti, *J. Colloid. Interface Sci.* **2019**, *533*, 621.
- [28] F. Bertorelle, M. Pinto, R. Zappon, R. Pilot, L. Litti, S. Fiameni, G. Conti, M. Gobbo, G. Toffoli, M. Colombatti, G. Fracasso, M. Meneghetti, *Nanoscale* **2018**, *10*, 976.
- [29] D. Calzavara, D. Ferraro, L. Litti, G. Cappozzo, G. Mistura, M. Meneghetti, M. Pierno, *Adv. Cond. Matter Phys.* **2018**, *Volume 2018*, Article ID 2849175, 9 pages.
- [30] G. Sciutto, S. Prati, I. Bonacini, L. Litti, M. Meneghetti, R. Mazzeo, *Anal. Chim. Acta* **2017**, *991*, 104.

Chapter 1

General introduction

1.1 SERS: a promising diagnostic technique applied to Cultural Heritage

The analysis of materials composing works of art has long been a fundamental issue. Moreover, the pursuit of techniques which are non-destructive or requiring the least amount of sample, can be considered the main challenge of the current research in the conservation field. The establishment of a scientific approach to the problems of conservation and restoration of cultural heritage, has prompted the development of portable and user friendly analytical devices suitable to provide quick, but reliable chemical information to the restorer while progressing during the restoration work. Analytical diagnostics on a work of art is indeed fundamental for restoration as well as for conservation purposes or for dating and certifying the authenticity of an ancient artefact. Analysing the chemical nature of the materials of which the work of art is made is indeed crucial to the above aims. While facing these tasks, it is important to take into account that the majority of works of art are objects with a complex nature being composed of different materials, often assembled in multiple layers and/or twisted together. A typical example of such a complexity is provided by the microscopic structure of the cross section of a paint (see Figure 1.1), composed indeed by five or even more superimposed layers, each one with its typical composition and each one requiring a specific analytical approach to be identified and classified [1]. Some of these layers are themselves composite materials: in particular, the pictorial layer is made by pigments (inorganic oxides and salts and/or organic dyes or pigments) bound and dispersed in the binder, the latter being a glue of animal or vegetal origin for tempera paints or a drying oil for oil paintings. Moreover, fillers or emulsifiers or preservatives or other additives can be present, depending on the period of production, painter, following restoration intervention etc.

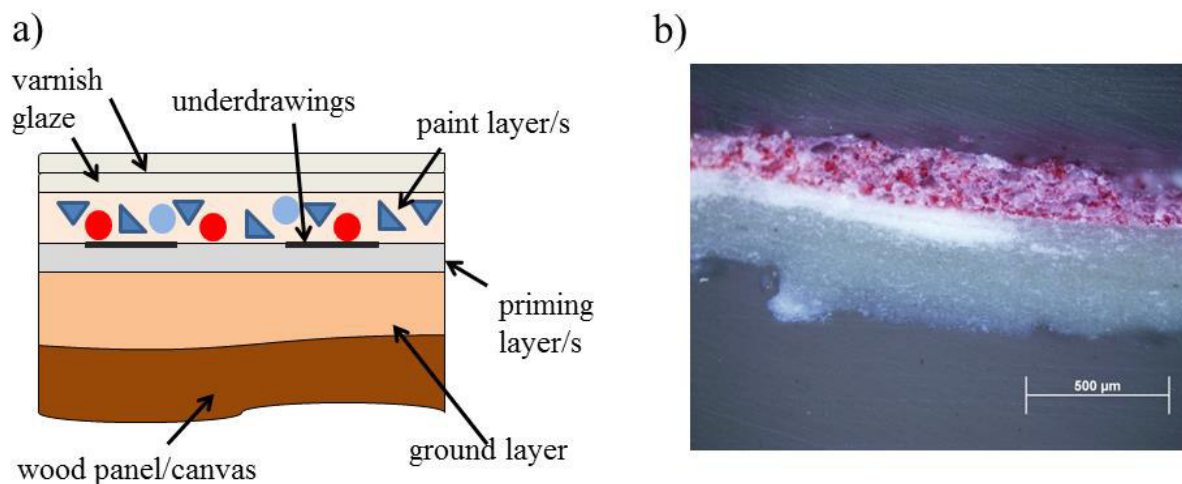


Figure 1.1 a) Scheme of a cross section showing all the layers composing a painting. The support, wood panel or canvas, is covered with the ground layer. Then the surface is further levelled by the priming layer where the underdrawings are made. On top, one or several painting layers can be found, made of pigments and/or dyes embedded in oil or tempera binders. Eventually, one or more layers of glaze and varnish coat the painting; b) optical microscopy image of a cross section sampled from a painting mock-up and embedded in a resin block. The optical microscopy analysis reveal the presence of the ground layer, made of gypsum and animal glue, and a paint layer composed by cochineal lake and lead white in egg tempera.

Consequently, when studying an artistic object, it is necessary to keep in mind that it must not be considered in a one-dimensional way, but as a 3D layered system. In order to better analyse its chemical composition in the three spatial coordinates, it is necessary to perform a micro-sampling to obtain a fragment containing all the layers forming the work of art (see Figure 1.1-b). This micro sample, or cross section, once embedded in salt or in resin, can be easily used as a base to perform many and repeatable analyses which can be physical, such as the optical microscopy documentation in visible (Vis) and ultraviolet (UV) light, and chemical. Concerning the latter, it is fundamental to distinguish between elemental analyses based on spot tests, X-rays fluorescence spectroscopy

(XRF), scanning electron microscopy (SEM) and the molecular ones such as staining tests, gas chromatography and mass spectrometry (GC-MS), high pressure liquid chromatography (HPLC) infrared (IR) spectroscopy or Raman spectroscopy. The detailed procedure to apply all the different analytical techniques starting from the less invasive to the more destructive ones can be found elsewhere [1]. Often, in order to obtain information on a certain component it is required to combine the information provided by different techniques. This allows one to overcome identification doubts and the instrumental limits of an individual analytical technique. For instance, in the case of a proteinaceous binder in a paint layer, which can be egg yolk vs. whole egg vs. animal glue or other, a quick and non-destructive technique such as IR spectroscopy not always provides conclusive information [2] so that it is often necessary to perform micro-destructive analyses by GC-MS [3] or HPLC-DAD [4] in order to distinguish the different proteins which characterize the above binders. These problems can be overcome to the aim of providing a quick, but reliable chemical information in the course of a restoration work, by an alternative approach based on the use of analytical sensors suitable to detect the presence or absence and, possibly, the amount of a specific target analyte. A sensor is an analytical device consisting of a molecular recognition element that is brought into contact with the sample and closely associated (connected or integrated) with a transducer that provides a signal useful for the detection and quantification of the concentration of the target analyte [5]. Substantially, a chemical sensor differs from a biosensor on the basis of the nature of the recognition layer that is made by a synthetic receptor for the former and a biological component for the latter. Independently on this, the advantage of using a sensor can be summarized in its capability of providing quick, reliable and specific analytical information while cancelling or minimizing the chemical steps necessary for performing the analysis. Moreover, when the sensor is intrinsically characterized by high sensitivity and low detection limits, the amount of sample needed can be lowered to an almost negligible amount, from few micrograms up to a maximum of hundred micrograms.

In the present context, we focus on the development of advanced vibrational spectroscopic techniques based on the optical properties of metal nanoparticles and nanomaterials, namely the surface enhanced Raman spectroscopy (SERS) [6,7]. Thanks to its promising qualities, it can also be used to produce analytical sensors, such as the SERS-based optical ones, characterized by high selectivity and extremely high analytical sensitivity. Note that, in the last years, SERS has witnessed significant improvements in analytical performances which, together with the smart use of nanomaterials, has allowed to obtain always more and more efficient and sensitive Raman based [8] sensing devices.

1.1.1 Classical Raman spectroscopy vs. SERS

The detection of pigments, dyes and binders by means of (micro) Raman spectroscopy performed *in situ* or on artistic samples, with or without previous extraction, resulted of great interest, allowing to perform the analysis directly on the sample without prior chemical or mechanical treatment. Moreover, the strong presence of Raman peaks in the ‘finger print’ region of the spectra allows to perform the detection and quantitative analysis of many pigments [9], even of different crystalline structures with high spatial resolution (up to 1 μm). All these features and, above all, its non-destructiveness make Raman spectroscopy an efficient diagnostic technique, easily performed *in situ* directly on the sample. On the other hand, Raman spectroscopy presents some disadvantages hampering its use for every kind of materials. As a matter of fact, Raman scattering is weak (spectroscopic cross-section of 10^{-28} cm^2/mol) and it can be easily covered by the much more intense fluorescence emission of the molecules (spectroscopic cross-section of 10^{-16} cm^2/mol), especially organics with conjugated electronic structures. The low sensitivity and the interference by fluorescence emission, limit the detection of organic molecules which can be found in very little amount in the works of art. It is worth stressing that some artistic materials are characterized by an intrinsic complexity, as it is the case of some natural lakes, composed by organic molecules bound to inorganic salts, or of complex matrices where the organic binder interacts with inorganic

pigments. On account of that, the attention has long been focusing on the development, optimization and comparison of analytical methodologies based on the improvement of the performances enhancement of the vibrational spectroscopy techniques in order to increase the sensitivity of the analysis. A valuable solution to these issues is offered by SERS. This effect, observed for the first time by Fleischmann, Hendra and McQuillan in 1973 [6], has been developed into a sensitive analytical technique which takes advantage of the great enhancement of the Raman signal by the proximity of the analyte with metal nanostructures and nanoparticles, mainly of silver, gold and copper. Indeed, the Raman scattering of molecules in close contact with a nano-structured metal surface excited by visible light experiences an enhancement up to an order of 10^6 . The origin of this phenomenon is mainly electromagnetic, caused by the occurrence of surface plasmon resonance, namely the excitation of the collective electrons of the metal by an external electric field. Since the intensity of Raman scattering is proportional to the square of the energy of the electric field, increasing the latter means to increase the Raman signal to both the excitation and the emission processes. As a result, Raman scattering is intensified and its enhancement is estimated by the Raman enhancement factor, defined as [7]:

$$REF = (I_{SERS} N_{Raman} P_{Raman} t_{Raman}) / (I_{Raman} N_{SERS} P_{SERS} t_{SERS}) \quad (1.1)$$

Where, subscripts Raman and SERS indicate data for the reference sample (i.e. with no adsorption on nanostructures) and adsorbed on the nanostructured material, respectively. N indicates the number of molecules illuminated by the laser beam and I denotes the peak intensity measured at the wave number where the SERS effect is high. Finally P and t are respectively the laser power and the exposure time.

Note that also the interference caused by fluorescence, is overcome by the SERS technique since the nanoparticles absorb most of the fluorescence photons emitted by the molecule, acting as quenchers and lowering the radiation efficiency [10].

1.2 Introduction to Raman spectroscopy

1.2.1 Molecular spectroscopy

The combination of atoms in a molecule generates a specific series of energetic states and therefore unique spectra reflecting the transitions between them. Indeed, a given molecule will absorb only those photons having energies that correspond exactly to the energy gap between two energetic states and each absorption will give rise to a specific spectral line. Molecular spectroscopy investigates the changes of the energetic states which correspond to the energy of the photons absorbed. When the photon belongs to microwave spectral region it will cause the nuclei in the molecule to rotate, processes studied by the rotational spectroscopy. Instead, in the case of a more energetic photon with an infrared-visible frequency, the excited molecule reaches a new vibrational state. This phenomenon involves the change of the relative position of atoms through the vibration of their chemical bonds and it is studied by the vibrational spectroscopy. Eventually, if the photon belongs to visible-ultraviolet region it promotes the molecule to a new electronic excited state, phenomenon investigated by UV-Vis and fluorescence spectroscopy [11]. Vibrational spectroscopy is the object of this thesis and between the two most important techniques of this branch, Infrared and Raman spectroscopy, the last one represents the election technique.

1.2.2 Vibrational spectroscopy

A molecule can be considered as set of spherical masses joined by springs following the Hooke's law, equation meaning that the elastic force F required to compress or extend a spring is proportional to its stiffness k multiplied by the variation in length dx :

$$F = -kdx \quad (1.2)$$

In a molecular group a large number of vibrational modes may occur and each vibration requires a quantized amount of energy to be performed. The following illustrates the main kinds of vibrations ordered from the most energy requiring one to the least:

- Stretching vibrations (ν): variation of the length of a bond between two atoms. When the movements of chemical bonds are towards the same direction is defined symmetric and asymmetric when they are opposite. Generally the asymmetric one is the most energetic vibration;
- Bending (scissoring) vibrations (δ): in-plane symmetric change of the angle formed by three atoms;
- Wagging vibrations (γ): out-of-plane symmetric change of the angle between the plane formed by the three atoms involved in the movement and that of the molecule;
- Rocking vibrations (ρ): in-plane asymmetric change of the angle between the plane formed by the three atoms involved in the movement and that of the molecule;
- Twisting vibrations (τ): out-of-plane asymmetric change of the angle between the plane formed by the three atoms involved in the movement and that of the molecule.

Each vibration generates a band in the spectrum that can be classified according to the following parameters:

- Position: it represents the energy of the vibration and it is measured in wavenumbers (cm^{-1}). It depends on two factors: the bond strength and the mass of the atoms involved. Indeed, according to the following equation the frequency ν of a vibration is inversely proportional to the reduced mass [$\mu = \frac{m_a m_b}{m_a + m_b}$ (1.3)] of the two atoms a,b involved dividing the force constant f :

$$\nu = \frac{1}{2\pi} \sqrt{\frac{f}{\mu}} \quad (1.4)$$

Resuming high wavenumbers belong to strong bonds, such as the triple or double ones, and to light atoms that generate a low reduced mass;

- Intensity: the relative intensity of bands depends on the change of polarizability α involved in that particular vibration. The more strong it is the more intense the band results. Especially strong ones are provoked by polar bonds;
- Broadness: the broadness of bands depends on intermolecular interactions such as the hydrogen bonding. In this way the polarity of a molecule may broaden consistently a band generated by the same chemical functions.

Each band is the result of a molecular vibration or, in other words, of the transition between quantized vibrational energy states. The different ways in which a molecule may vibrate, called the vibrational modes, are calculated using the formula $3N - 6$ ($3N - 5$ for the linear molecules) (1.5), where N represents the number of atoms composing the molecule. The result is the number of degrees of freedom of a molecule for a fixed point in space [11,12].

1.2.3 Raman spectroscopy

Raman spectroscopy is based on the inelastic scattering of a monochromatic incident light. This physical phenomenon, discovered by the Indian physician C.V. Raman in 1921 [11], can provide a unique fingerprint of each molecule: its Raman spectrum. A Raman band corresponds exactly to the difference between the energy of the incident photon and the scattered one and its frequency depends specifically on the electronic configuration of each molecule. When a sample is illuminated by a monochromatic light of frequency ν_0 the majority of the impinging photons are absorbed, reflected or transmitted. Just a small fraction interacts with the analyzed molecules via its oscillating electric field, making them reach virtual excited states. Indeed, the molecules are not achieving a new electronic state but intermediate levels between the excited and the ground state, called for this reason “virtual”. This condition is very unstable and the molecules decay

instantaneously to the ground state by one of the here exposed different processes, well exemplified through the simplified Jablonski diagram in Figure 1.2 [11]:

- Rayleigh scattering: the molecule relaxes to its ground vibrational state emitting a photon of the same energy as the incident ones. This is an elastic phenomenon occurring in most cases which does not give information about the molecule itself. It can be expressed by the following equation where $h\nu_I$ is the scattered photon and $h\nu_0$ is the incident one:

$$h\nu_I = h\nu_0 \quad (1.6)$$

- Stokes and anti-Stokes scattering: a very small fraction of the impinging photons (approximately 1 in 10^6) is scattered inelastically by the molecule which does not return to its ground vibrational state. It can decay to a higher vibrational level of its ground electronic state emitting a photon with a lower energy than the incident ones. This process is called Stokes scattering and can be expressed by the following equation where $h\nu$ is the energy difference between the excited and the ground vibrational state:

$$h\nu_I = h\nu_0 - h\nu \quad (1.7)$$

The anti-Stokes scattering is a less common temperature-dependent phenomenon that requires the molecule to be originally in an excited vibrational state. In this way, during the decaying process the molecule reaches its ground vibrational level emitting a photon which is more energetic than the impinging ones:

$$h\nu_I = h\nu_0 + h\nu \quad (1.8)$$

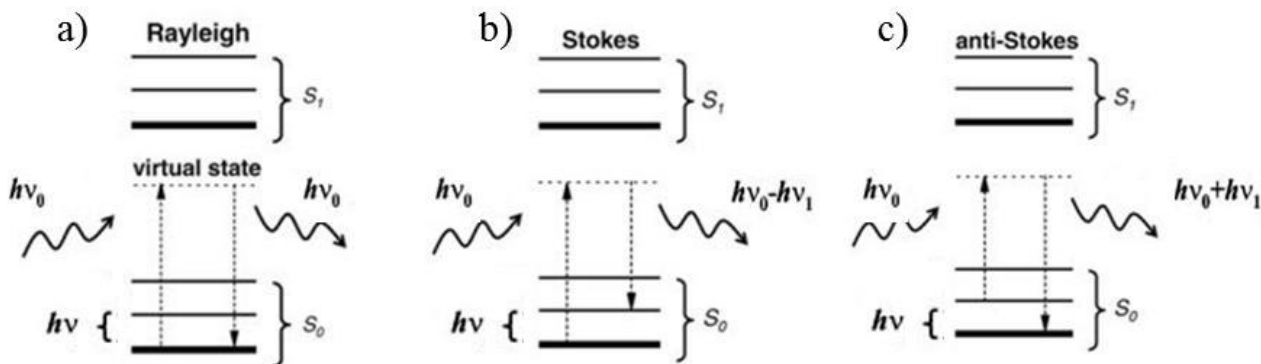


Figure 1.2 Simplified Jablonski diagram illustrating the Rayleigh (a) and Raman (b,c) scattering processes. A molecule is excited by impinging photons of energy $h\nu_0$. The scattered photons $h\nu_1$ have a) the same energy in the case of the Rayleigh scattering, b) an energy diminished of the gap between the excited vibrational state and the ground one ($h\nu$) in the Stokes scattering or c) an energy increased of the same energy $h\nu$ in the anti-Stokes one. Adapted from [11].

Generally, the Raman spectra show only the Stokes scattering portion in a Cartesian coordinate system reporting in abscissa the energy of the photons reaching the detector in wavenumber ($1/\lambda$ in cm^{-1}) and in ordinate their relative intensity. Each band corresponds to a permitted vibration. The gross selection rule is that the vibration process must involve a change of polarizability α of the molecule itself, defined as the average electric dipolar moment per unit of volume of the sample. This means that the polarizability measures the tendency of a charge distribution, that is the electron cloud of the atoms in a molecule, to be distorted by an external electric field. In the case of vibrational Raman spectroscopy the specific selection rule $\Delta\nu = \mp 1$ which involves the variation of the vibrational energy levels. It depends strictly on the change in polarizability since if it remains the same, the vibrational transition can't take place [11,12].

1.3 Surface enhanced Raman spectroscopy

1.3.1 Optical properties of metals

SERS is a technique which takes advantage of the optical properties of metal nanoparticles and nanomaterials, which are able to intensify the Raman signal emitted by molecules in their proximity. Materials are optically characterized by their dielectric function $\varepsilon(\omega)$ and their refractive index $n(\omega)$ which depends on the frequency of the light ω . These values are linked by the following equation [13]:

$$n(\omega) = \sqrt{\varepsilon(\omega)} \quad (1.9)$$

For transparent materials these parameters are positive and real numbers. Instead, materials of different nature present frequency-dependent ε and n with complex values, expressible by a real and an imaginary function. The real part of the dielectric function is large and negative while the imaginary one is limited and positive. If we take into consideration just the real part, the dielectric function of metals can be described by the *lossless Drude model* as function of the frequency ω and of the wavelength λ :

$$\varepsilon = \varepsilon_{\infty} \left(1 - \frac{\omega_R^2}{\omega^2}\right) = \varepsilon_{\infty} \left(1 - \frac{\lambda^2}{\lambda_R^2}\right) \quad (1.10)$$

where ω_R is the plasma frequency of the metal [13]. This value is the frequency at which the conduction electrons naturally oscillate and is proportional to the square root of the free electrons in the metal. However, the real metals are not lossless and the imaginary part of the dielectric function determines the absorption of light. A metal like Ag reflects almost totally the impinging photons because its imaginary part is approximately zero [$\text{Im}[\varepsilon(\lambda)] = 0$] (1.11). Conversely, the imaginary function of Au is characterized by higher values for wavelengths lower than 600 nm which causes the absorption of photons of that spectral region and the typical golden color of this metal.

Geometry-induced resonances, made possible by the characteristic electronic structure of coinage metals, are the base of the SERS technique. Indeed, the fact that metals have a wide-range negative $\text{Re}[\varepsilon(\lambda)]$ makes them ideal to satisfy the resonance conditions for many objects having different geometries [13]. Generally, SERS substrate are composed by particles that can be approximately described as nanospheres with a diameter ranging between 20 and 100 nm. Size is another fundamental issue since increasing this parameter causes a red-shift of the surface plasmon resonance, up to the complete damping of the phenomenon.

Let us consider a metal nanosphere. When an external electric field E interacts with a metal NP an induced dipole μ is produced. This last depends on the dielectric function of the embedding medium, generally the air ($\varepsilon_M = 1$), and on the wavelength-dependent one of the metal, $\varepsilon(\lambda)$:

$$\mu \propto \frac{\varepsilon(\lambda) - \varepsilon_M}{\varepsilon(\lambda) + 2\varepsilon_M} \quad (1.12)$$

when $\varepsilon(\lambda) = -2\varepsilon_M$ (1.13) the denominator equals zero, the induced dipole tends to infinite. In detail, the real part of the dielectric function satisfies the condition $[\text{Re}[\varepsilon(\lambda)] = -2\varepsilon_M$ (1.14)], only limited by the imaginary function whose influence, especially for Ag, can be considered as negligible. As a consequence, the system will show a large response called dipolar localized surface plasmon resonance (LSPR) of the sphere [13].

Therefore, when the wavelength of the incident field satisfies the boundary conditions for the resonance ($\lambda \sim \lambda_R$), the surface of the sphere will undergo a strong local field enhancement. This last can be calculated with the local field enhancement factor (LFIEF) which is the ratio of the normalized value of the local field intensity at position r and depending on the incident wavelength λ , proportional to the square of the local electric field energy $E(r, \lambda)$, to the intensity of the incoming field $E_0(r, \lambda)$ at that point:

$$\text{LFIEF}(r, \lambda) = \frac{|E(r, \lambda)|^2}{|E_0(r, \lambda)|^2} \quad (1.15)$$

In other words, the LFIEF is a dimensionless parameter expressing the change in local intensity caused by the presence of objects that perturb the electric field of light. In the case of a sphere it will be maximum at the two extremities of the axis passing through its center, where the external field and the induced dipole add up (Figure 1.3). If a molecule is placed at those positions, it experiences the consistent enhancement of the local field, allowing the SERS effect to have place [13].

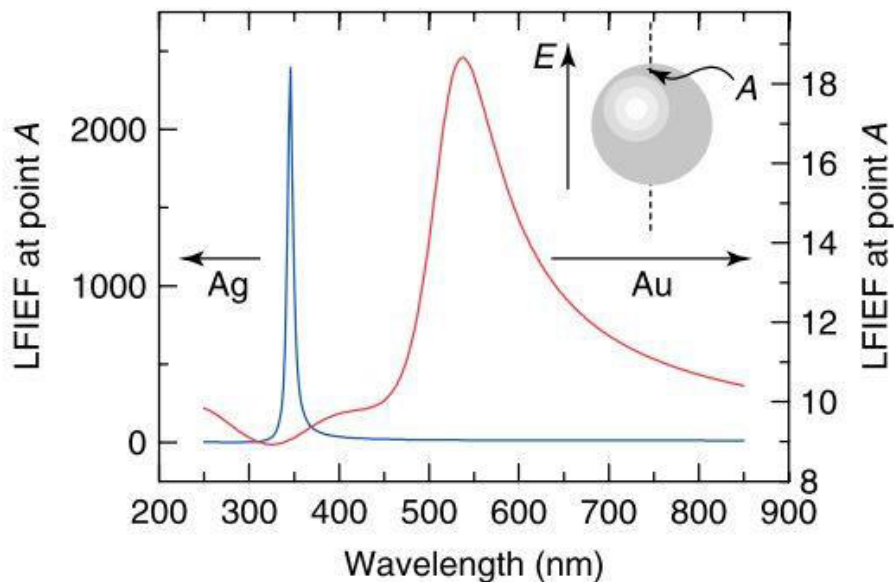


Figure 1.3 Plot representing the LFIEF at point A in a sphere of Ag and Au. When the resonance conditions are satisfied [$\text{Re}[\varepsilon(\lambda)] = -2$ in air (1.16)] the enhancement of the local field reaches its maximum. In the case of Ag the resonant wavelength is at around 350 nm, while that of Au is approximately at 550 nm. The LFIEF of Ag is much more stronger due to its low level of absorption compared to that of Au. Adapted from [13].

Among the metals studied in Figure 1.4, Ag is the most suitable one and is in fact widely used for SERS and plasmonics. Au and Cu are also suitable, but only at longer wavelengths (typically more than 600 nm). At such wavelengths, the optical absorption of gold in fact becomes comparable to

that of silver. Au is certainly the most promising in this category and should therefore be the material of choice for applications beyond 600 nm (in the red and near IR). Instead, Ag, whose absorption is the lowest especially below 600 nm, can be used for large field enhancement applications (such as single-molecule detection) [11].

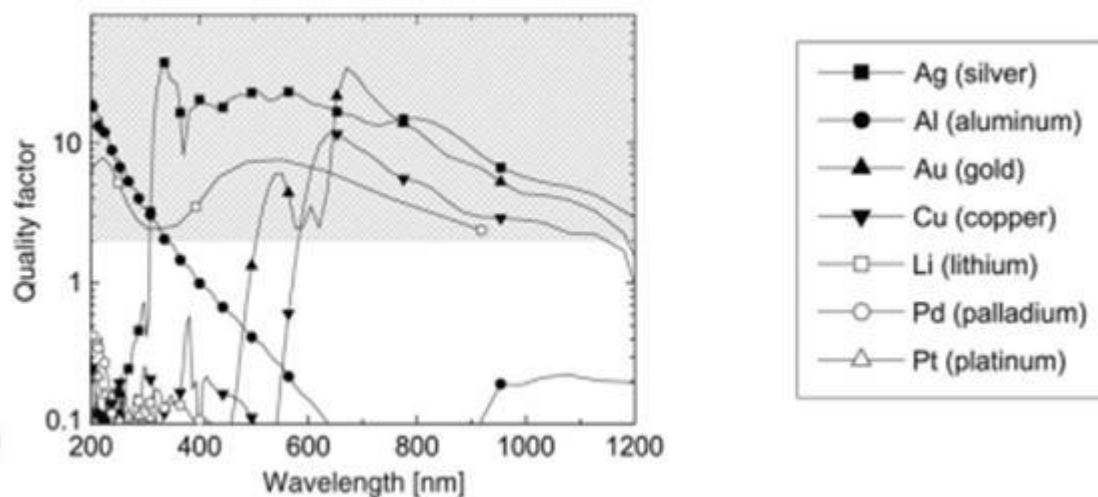


Figure 1.4 Diagram showing the approximate quality factors of localized surface plasmon resonances in the extended visible range for nanoparticles of a selection of metals in air. The shaded area is the area of interest to many plasmonic applications. Adapted from [11].

1.3.2 Enhancement of Raman signal and quenching of fluorescence

A molecule in the proximity of metal nanoparticles can experience not only the enhancement of its Raman scattering but also of its emitted fluorescence. However, the effect of the local field enhancement on these two phenomena is very different in dependence on their own nature [11-14]. Stokes Raman scattering is an instantaneous process which does not involve the absorption of a photon. Indeed, an incoming photon excites the molecule to a virtual state and during the relaxation, the photon is scattered with a lower energy, leaving the molecule in a different vibrational level of its ground state. On the other hand, fluorescence is a stepwise phenomenon based on the absorption of a photon by which the molecule reaches a new electronic state (S_1). Then the molecule undergoes

a series of passages through the vibrational substructure of S_1 , the first singlet state, and only after the photon is re-emitted, allowing the relaxation to the ground singlet state S_0 . The fundamental difference between these two phenomena is that while in Raman scattering the absorption of the incident photon and its re-emission are instantaneous, in fluorescence these two processes are separate in time. As a consequence, both phenomena will be positively affected in the absorption of the incoming photons since the absorption cross section σ_{abs} of the molecule is increased time the LFIEF. Otherwise, in the emission process only Raman scattering receives a benefit which involves an enhancement of its intensity proportional to the forth power of the incident electric field ($|E^4|$). The emission process in fluorescence, on the other hand, is disconnected from the absorption one. For this reason, the only possible effect of the environment on emission is to modify the relative contribution of radiative and non-radiative decay, the so called *quantum yield* or *radiative efficiency* η . Generally, the presence of a metallic surface inhibits the radiative decay providing channels of absorption of the emitted photons. In this way, the combination of the enhanced absorption and the low radiative efficiency ($0 \geq \eta \leq 1$) produces a strong quenching of the fluorescence for a molecule in the proximity of a metal substrate [13].

Summarizing, it is important to underline that the Raman scattering enhancing factor (REF) is the result of an average over the different spatial collocations of molecules on a SERS substrate. Indeed, low and high enhancements depends strictly on the relative positions of the metal NPs and of the molecules adsorbed on them. Especially strong intensifications of the local field may occur in the so-called *hot spots*, located in the gaps between dimers of NPs. In these special regions the respective induced dipoles of the two NPs interact and produce a coupled plasmon resonance which involve the consistent increasing of LFIEF and a red-shift in the resonant wavelength. On the other hand, nearby areas may experiment a negative interaction of the two induced dipoles, weakening the local field. Average REFs are in the range of 10^4 - 10^7 , standard values for this enhanced vibrational spectroscopic technique [11-14].

1.3.3 Intensification mechanism of the SERS effect

The SERS effect is basically caused by two mechanisms: the electromagnetic and the chemical one. The first one is a long-range effect due to the optical properties of nanostructured metal surfaces while the second one is a short-range effect caused by the charge transfer between the chemisorbed species and the SERS substrate. These two phenomena do not contribute the same to the SERS intensification of the Raman scattering. Indeed, the electromagnetic effect contributes in an order of magnitude of 10^{10} while the chemical one of 10^2 [14]. In order to explain how they work, it is necessary to consider the origin of the Raman effect. When the electric field, E , of an incoming photon interacts with a molecule of polarizability α , it induces a magnetic dipolar moment, μ according to the expression [11,12]:

$$\mu = \alpha E \quad \left[\mu = \frac{cm^2}{v} \frac{v}{m} = cm \right] \quad (1.17)$$

The molecular vibrations change the polarizability since it depends on the coordinates of the nuclei, vibrating around their equilibrium positions. The intensity of the Raman effect, that is to say the number of photons emitted, is proportional to the square of the applied electric field times the square of the polarizability [13]:

$$I_{\text{Raman}} \propto E^2 \alpha^2 \quad (1.18)$$

Concerning the electromagnetic effect, the intensification of the Raman scattering is caused by an electric field enhancement in proximity of the metal surface. Instead, in the chemical effect the polarizability of the adsorbed molecule is modified itself.

Figure 1.5 shows how the Raman effect intensification by electromagnetic mechanism works [41]. The electric field that affects the molecule adsorbed onto the NPs, in position r , corresponds to the sum of that belonging to the laser radiation (E_0) and the one scattered by the metal itself (E_S). The photons of these two components have the same frequency ω_0 and, when it coincides with the

surface plasmon resonance of the metal, the scattered field by the metal is strongly enhanced of a g factor. In this case it is reasonable to approximate the total electric field affecting the molecule with that scattered by the metal substrate. These concepts may be summarized by the following expressions:

$$E_{\text{TOT}}(r, \omega_0) = E_0(r, \omega_0) + E_S(r, \omega_0) \quad (1.19)$$

$$E_{\text{TOT}}(r, \omega_0) \cong E_S(r, \omega_0) = g E_0(r, \omega_0) \quad (1.20)$$

This impinging electric field will induce a dipolar magnetic moment in the molecule according to its polarizability in line to the equation:

$$\mu(r, \omega_0) = \alpha_R E_{\text{TOT}}(r, \omega_0) \quad (1.21)$$

Consequently, the emitted Raman radiation of frequency ω_R will have an electric field with an energy E_R proportional to $\alpha_R E_S$. In its turn, the energy of the Raman photons will be intensified by the NPs of a factor g' in the same way of those of the laser radiation so that the total electric field scattered will corresponds to:

$$E_{\text{TOT}}(r, \omega_R) = E_R(r, \omega_R) + E_{RS}(r, \omega_R) \quad (1.22)$$

$$E_{\text{TOT}}(r, \omega_R) \cong E_{RS}(r, \omega_R) = g' E_R(r, \omega_R) \quad (1.23)$$

In this way the resulting energy of the electric field scattered or, in other words, of the enhanced Raman effect corresponds to (Figure 1.5):

$$E_{\text{SERS}} \cong E_{RS} \propto g' E_R \propto g' \alpha_R E_S \propto g g' \alpha_R E_0 \quad (1.24)$$

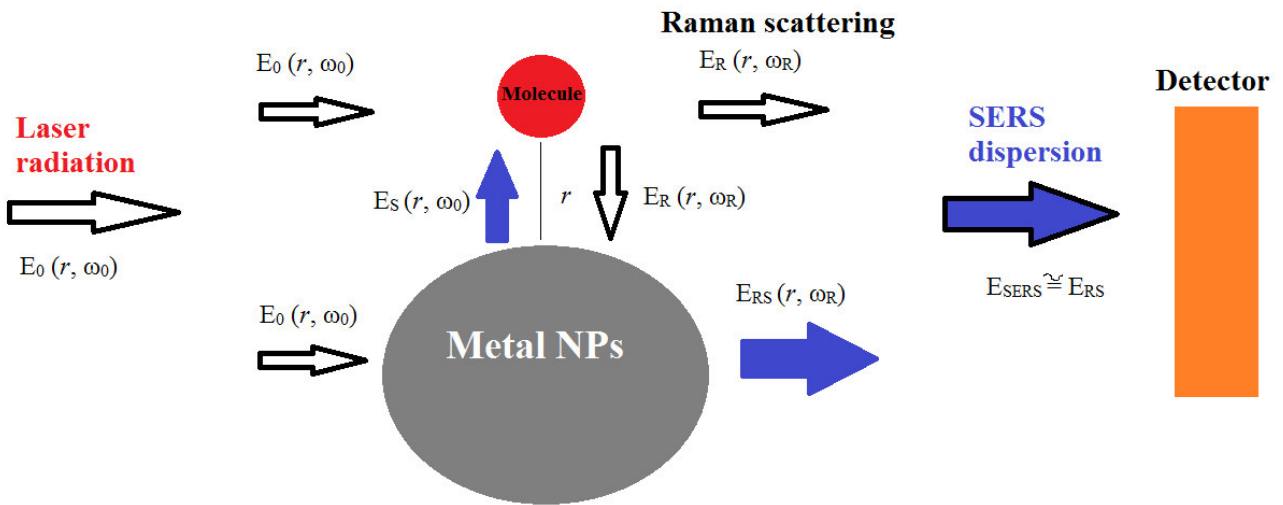


Figure 1.5 Scheme exemplifying the SERS electromagnetic effect. The electric field affecting the molecule adsorbed onto the NPs, in position r , corresponds to the sum of that belonging to the laser radiation (E_0) and the one scattered by the metal itself (E_S). The total Raman scattering radiation which is recorded by the detector is the sum of that emitted by the molecule (E_R) and the one enhanced by the NPs (E_{RS}). Approximating, the total energy of the SERS dispersion corresponds to E_{RS} . Adapted from [15].

The intensity of the scattered photons due to SERS effect will result proportional to the intensity of the incident electric field multiplied by the square of the enhancing factors and the polarizability of the molecule:

$$I_{SERS} \cong (g g')^2 \alpha_R^2 E_0 \quad (1.25)$$

Generally the difference between the frequency of the impinging photons and the Raman ones is negligible so that it is possible to approximate the enhancing factor of the impinging radiation and that of the scattered one. In this way, the amplification of the incident radiation results multiplied by

the fourth power of the enhancing factor, g^4 . It is important to define the G intensification factor in order to understand the relation between the SERS and Raman intensity of the scattered photons:

$$G = \frac{I_{SERS}}{I_{Raman}} = \frac{\alpha_R}{\alpha_{R0}} (gg')^2 \quad (1.26)$$

where I_{Raman} is the intensity of the scattered electric field without the metal and α_{R0} the polarizability of the molecule in absence of the SERS substrate.

The other phenomenon causing the SERS effect is the chemical one, exemplified in Figure 1.6 [14,15]. Unlike the electromagnetic (EM) mechanism which produces a global intensification of the Raman spectrum, the chemical mechanism causes a selective enhancing of bands according to the vibrational modes produced by a specific molecular symmetry. Moreover, it is not a long-range effect like the EM one which involves even the farthest molecules, but it occurs just when the analytes are in close contact with the NPs. In detail, when the interaction between the adsorbate and the metal is weak a *physisorption* occurs, involving a slight modification of the polarizability of the molecule. In this case the SERS spectrum is very similar to the Raman one. On the other hand, if the interaction is strong enough to allow a *chemisorption*, the molecules form a complex with the metal in which new electronic transitions can take place, implying different levels of energy of the adsorbates. In this way, the electrons belonging to the HOMO (highest occupied molecular orbital) of the adsorbate pass to its LUMO (lowest unoccupied molecular orbital) or to the Fermi level of the metal (Figure 1.6). The second option is the most common, promoted by a stronger molecule-NPs interaction which generates a strong connection between their molecular orbitals. The charge transfer is likely to occur the most when the molecule presents π electrons, prone to be yielded and, in this way, involved in this process.

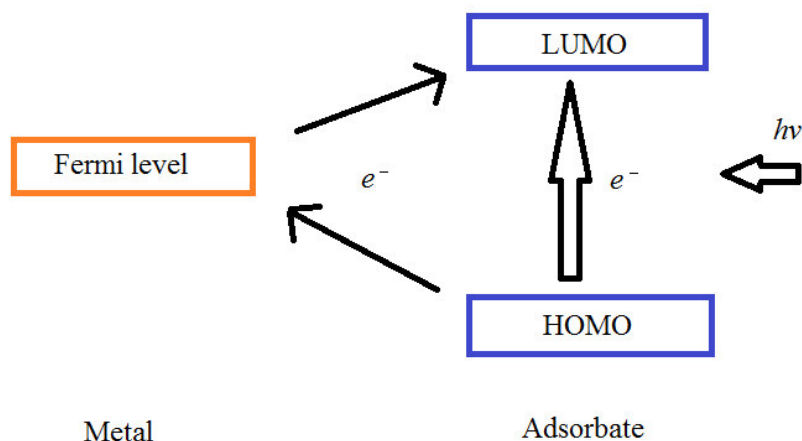


Figure 1.6 Scheme exemplifying the chemical mechanism of the SERS effect. When the molecule is chemisorbed on the metal their external orbitals are prone to overlap. In this way, an impinging photon of energy $h\nu$ may promote the excitation of an electron from the HOMO orbital of the molecule to the LUMO one with a direct passage or through the intermediate Fermi level of the metal. Adapted from [14].

1.4 Synthesis of nanomaterials: soft and hard template, electroless and electrochemical deposition

1.4.1 Electroless soft template synthesis of nanoparticles

The soft template synthesis is a method which requires the presence of molecules on the surface of crystalline seeds, so directing the shape to the developing NPs [16]. This role is played by the so called capping agent which can even act as reducing agent at a same time. Indeed, in the electroless synthesis, the reduction of the metal ions in water solution is operated by a molecule which acts as electron donor, undergoing oxidation. Metal NPs present an interface characterized by residual positive charges, due to a deficiency of electrons in the superficial atoms. This charge is neutralized by negative ions, generally deriving from the salts used to prepare the colloid. In this way a double

ionic layer is generated around the NP: an inner layer named Stern and a diffuse layer (see Figure 1.7). Obviously, electric interactions between adsorbed anions and the metal surface are stronger in Stern layer. This electric attraction is lower in the diffuse layer up to disappearing totally throughout the bulk solution. The electric potential, called zeta (ζ) potential, is preferentially measured between the Stern and diffuse layer, where it is maximum (Figure 1.7) [12,14]. The ζ potential is fundamental not only to understand some properties of NPs such as stability and mobility, but also during their synthesis, where the role of the capping agent is ruled by an equilibrium of charges at the interface between NPs and solution.

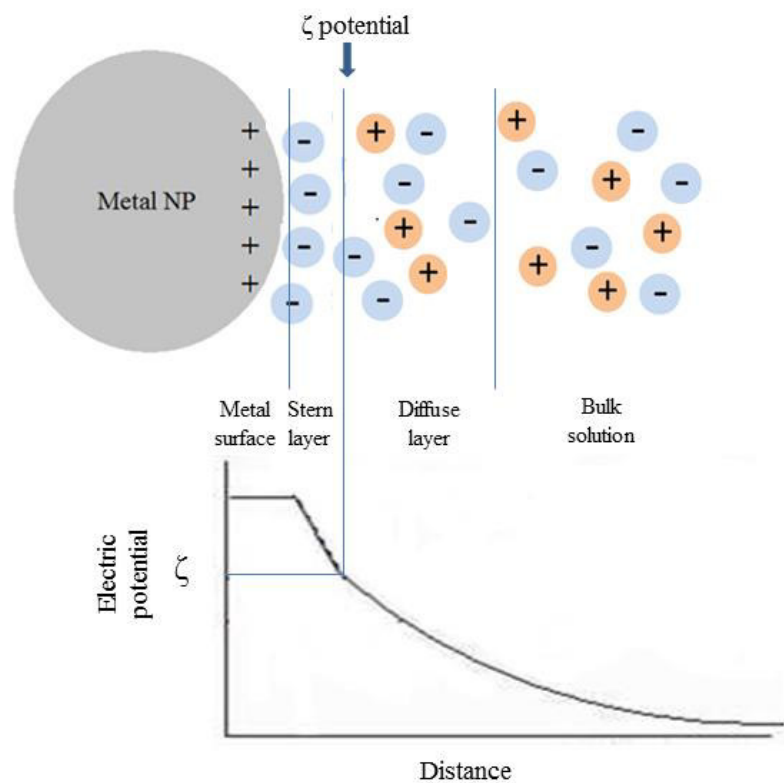


Figure 1.7 Scheme showing the distribution of electric charges and the curve of the electric potential between the surface of the metal and the bulk solution. The ζ potential is found between the Stern and diffuse layers. Adapted from [12,14].

The occurring chemical reaction can be illustrated in this way:



At first the reduced metal atoms get together forming clusters which, in turn, aggregate to give birth to nanoparticles. Using this method we are likely to produce NPs with a spheroidal shape, even if, employing particular techniques and capping agents, it is possible to obtain different morphologies. Several reducing agents are employed: ascorbic acid ($C_6H_8O_6$), sodic borohydride ($NaBH_4$), sodium citrate tribasic dehydrate ($C_6H_5Na_3O_7 \cdot 2H_2O$), pure hydroxylamine (NH_2OH) and hydroxylamine hydrochloride ($NH_2OH \cdot HCl$). After the reduction process the oxidized products from the reducing agent can remain on the surfaces of the NPs and act as intereferents. In the case of citrate, molecules such as 1,3-acetonedicarboxylic acid ($C_5H_6O_5$) and acetoacetic acid ($C_4H_6O_3$) are likely to be found. This shortcoming is overcome when hydroxylamine is employed since its oxidation products are gaseous H_2O and N_2 which are dispersed without leaving residues in the colloid [15].

As already introduced, the Raman enhancement generated by spherical nanoparticles and other isotropic nanomaterials can be further increased by employing nanomaterials characterized by anisotropic features [17-20], reaching REF up to 10^8 [21] (see Chapter 2).

1.4.2 Electroless and electrochemical hard template synthesis of high aspect ratio nanomaterials

The hard template synthesis of high aspect ratio nanomaterials, e.g., nanowires, is a method based on the use of a template as a mold for the oriented growth of metal structures which trace the shape of its pores [16]. This method was first developed by G.E. Possin, in 1970 [22], and then optimized [23,24]. Nanoporous membranes of different materials are employed to this aim, mainly of alumina and polycarbonate. The alumina membranes, prepared through controlled anodization of aluminum,

are characterized by dense and ordered pores, hexagonally organized in a fragile matrix (Figure 1.8-a) [25]. The polycarbonate membranes whose porosity is obtained by bombarding the polymeric film with high-energy ions (track-etching technique) and then a chemical etching in alkaline solution [26]. Extremely flexible, they present a sparse and irregular porosity (Figure 1.8-b).

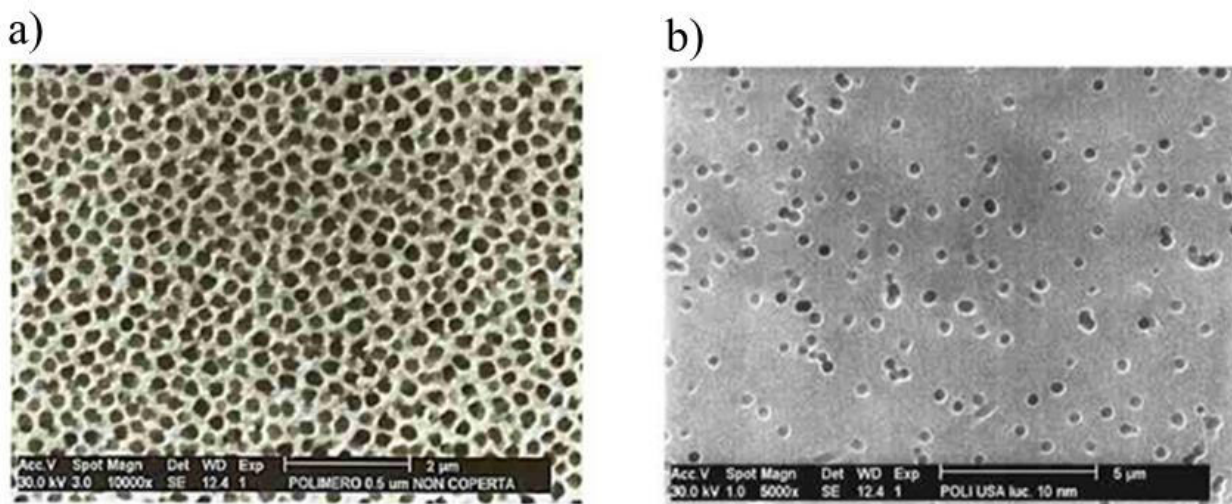


Figure 1.8 SEM images of an A) alumina and a B) polycarbonate nanoporous membrane.

Electroless deposition

The electroless template deposition of metals requires a chemical which acts as reducing agent and the kinetic of this reaction, namely the electron transfer from the reducer to the metal ions, must be slow. If the reducing agent is adsorbed on the surface and pores of the template, the deposition starts from the pore walls and then continues inwards. For this reason, if the deposition time is stopped in the early steps, it is possible to obtain hollow nanomaterials, such as nanotubes [27]. Instead, when the process is let proceed until completion, typically around 24 h, the pore structures are filled completely, becoming wires. This is what happens during the electroless growth of Au nanowires (AuNWs) using track-etched polycarbonate membranes as templates [28,29]. The membrane is first sensitized with Sn^{2+} , then it is dipped in a Ag^+ solution and eventually in solution of a Au^+ salt. The following step is the addition of formaldehyde which reduces progressively Au^+ .

The metallic gold substitutes galvanically the Ag seeds previously formed into the pores, producing the nanowires, at the same time covering the outer faces of the membrane. After the deposition, the gold in excess is removed from one face by peeling and then, the template can be removed partially [30] or totally [31] to expose the wires. The templated electroless deposition of AuNWs in the shape of nanoelectrodes ensembles (NEE) is illustrated in Figure 1.9 [32]. This kind of substrate, once freed from the template membrane by etching, is suitable to SERS measurements and further functionalization procedures. This procedure has been extensively used in the context of this thesis (see Chapter 3).

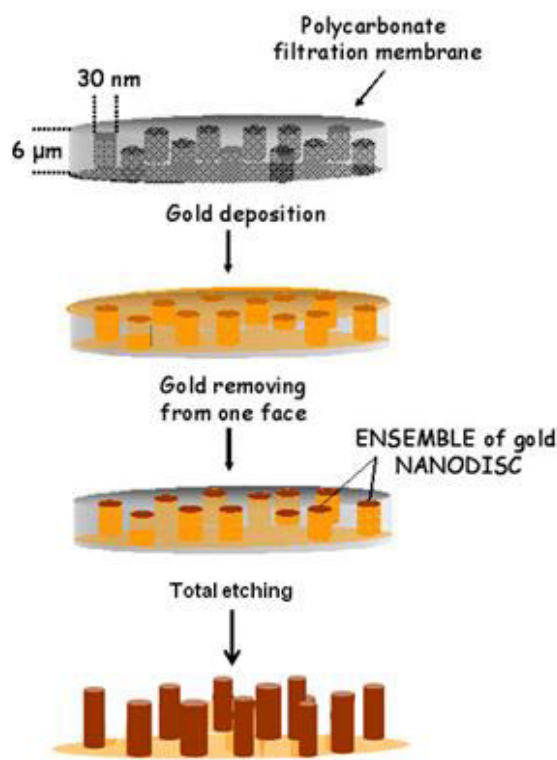


Figure 1.9 Schemes summarizing the steps used to produce AuNWs via electroless reduction of gold in track etched polycarbonate membrane, which is thereafter etched in order to create a 3D structure.

Electrochemical deposition

In order to perform the electrochemical deposition of a metal inside a nanoporous non-conductive membrane it is necessary to make one face of the membrane conductive. This can be achieved by sputtering a metal layer on one face of the membrane or by creating an intimate contact between the membrane and a solid metal surface or by combining both methods [33]. The so prepared membrane is placed into an electrochemical cell where it acts as cathode (working electrode -WE-), in presence of an anode (counter electrode -CE-) and eventually, a reference electrode (RE) (Figure 1.10) [32]. The metal ions in solution are reduced to metal at the interface between the electrolyte in the pores and the underlying metal electrode, by the application of a suitable reducing potential. Therefore, the pores are filled from the bottom to the top. The final result is an ensemble of solid wires whose matrix can be etched to expose them partially or completely.

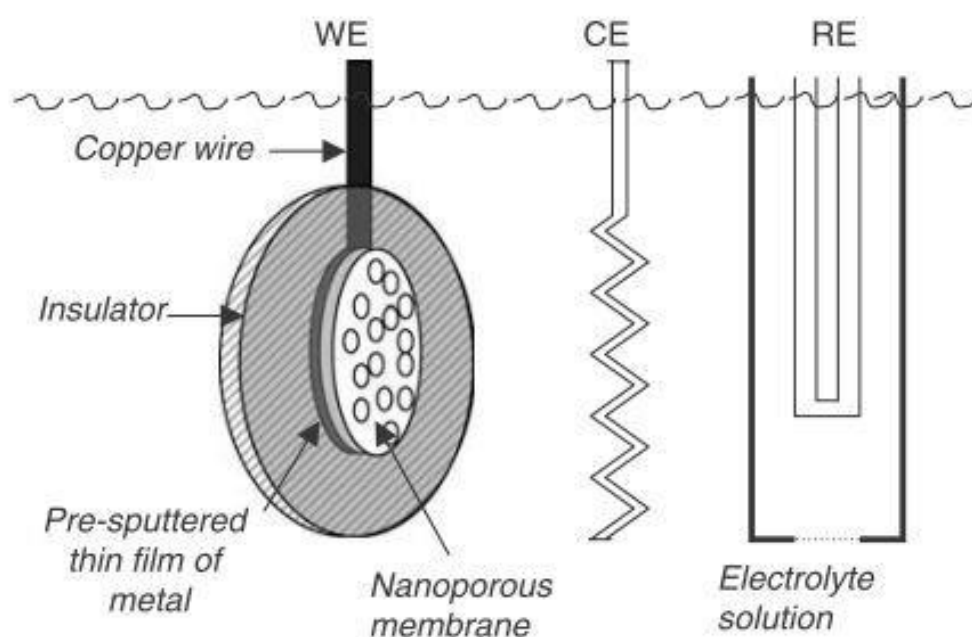


Figure 1.10 Scheme of the electrochemical cell for the templated deposition of metal nanowires. The pre-sputtered membrane is attached to the surface of the working electrode. The electrodeposition is carried out in presence of a counter and a reference electrode, in a electrolyte solution composed by the metal precursor. Adapted from [32].

This kind of deposition is called potentiostatic when involves the application of a constant reducing potential. Figure 1.11 shows the typical chronoamperogram -current (I) vs time (t)- which shows how the current changes with time for electrodeposition within a porous substrate, containing pores ideally with the same diameter and length. Typically three different steps of the deposition are observed: I) the NWs start growing into the pores with a low current, however the exposed surface is constant; II) the pores are completely filled and the current increases steadily because the exposed surface increases; III) further metal is deposited on the outer surface and the current reaches a novel plateau, because the exposed surface is again constant, corresponding to the outer surface of the membrane [34].

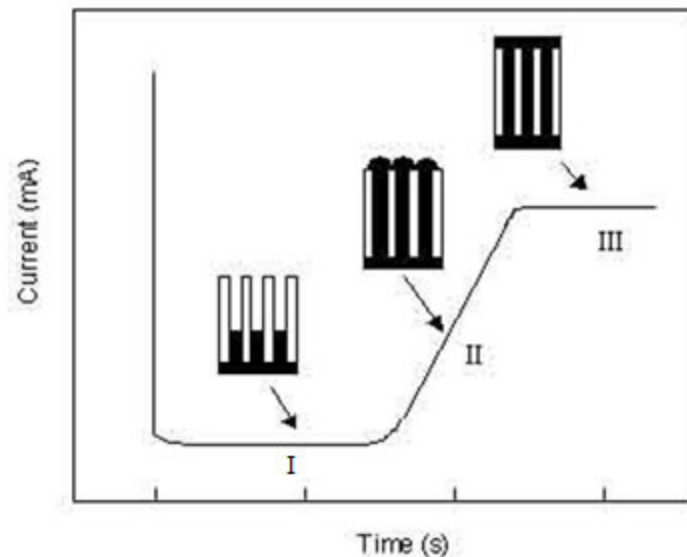
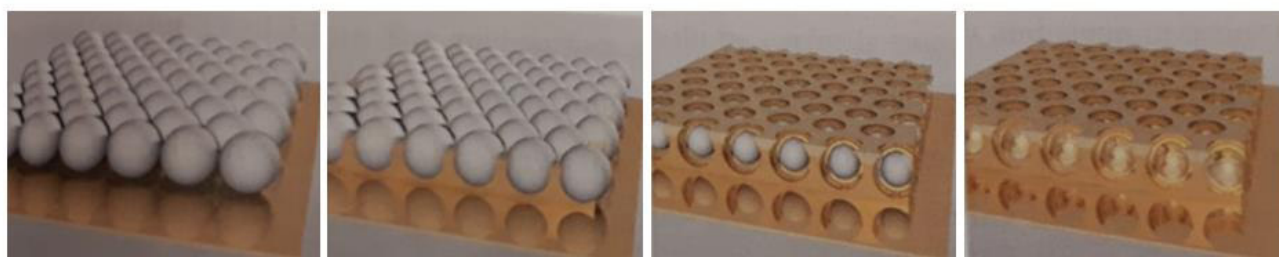


Figure 1.11 Chronoamperogram showing the trend of the current during the deposition of NWs within high aspect ratio nanopores.

In particular, in the following I will focus on the electrochemical deposition of copper nanowires. Copper indeed resulted particularly attractive for the templated deposition of nanowires (CuNWs) [33] due to its low cost, its affinity for the electrode surface and its ability to enhance the Raman signal, especially when using an excitation laser towards the red and near IR [11] (see Chapter 4).

1.4.3 Electrochemical hard template synthesis of nanostructured surfaces

The advantage of synthesizing a nanostructured surface is to obtain an ordered and homogeneous substrate, characterized by the repetition of the same structures in the space. Different procedures can be followed to achieve such a structure, for instance the nanolithography [35]. However, in this context we will focus on the electrodeposition of ordered nanomaterials by hard template synthesis. This method is based on the deposition of a metallic layer in presence of a mold which can be removed successively. An appropriate example is represented by the sphere segment void (SSV) surfaces [36-38], employed as SERS substrate in this thesis (see Chapter 5). These substrates are thin layer metal film decorated with an ordered arrangement of spherical cavities obtained from a monolayer of closed packed polystyrene spheres, successively removed by chemical dissolution (Figure 1.12). The so prepare nanostructured surface is an efficient SERS substrate, characterized by anisotropic nanomaterials which alternate ridges and cavities and act as light harvesters [39,40].



1) Nanosphere template 2) Electrodeposition 3) Dissolution of spheres 4) SSV surface

Figure 1.12 Steps for the preparation of an SSV substrate: 1) a closed-packed monolayer of polystyrene spheres is used as template; 2) the electrodeposition of gold reach $0.5d$ of the spheres, that is to say the 50% of their diameter; 3) the deposition is stopped when the gold height is the 80% of the spheres; 4) the spheres are dissolved in dimethylformamide leaving a SSV surface.

1.5 Hierarchical structures of nanomaterials

As above introduced, a remarkable improvement of the SERS technique is represented by the production and development of hierarchically organized nanomaterials [41,42] which can also be chemically functionalized [43] with different analytical purposes. A first advantage is the further promotion of plasmonic effect operated by bimetallic structures, reaching REF in the order of 10^5 [58]. Secondly, the contemporary presence of two metals can result favorable, such as in the case of hierarchical structures made of Ag and Au, through which the strong enhancement caused by Ag and the affinity of Au for biological samples can be exploited at the same time [44]. Considerable SERS effects have been observed for hierarchically organized nanostructures prepared by electrosynthesis of metal or metal oxide sub-nanostructures on ensembles of gold nanowire electrodes or by depositing AgNPs on vertically aligned semiconductor nanorods [45]. Significant REFs were produced by hierarchical nanostructures made of spherical AgNP on flat gold [46], starry-shaped AuNPs arrays on Ag films [47], AgNPs assembled on powdered copper substrates [48]. Hierarchical 3D SERS substrates were prepared by depositing a monolayer of Ag nanocubes on micropylramids of silver functionalized with 4-methylbenzenethiol SERS probe [49]. SERS active nanosphere arrays composed by Ag underlayer and Au overlayer were systematically constructed to detect 2-naphthalenethiol dye as Raman probe [50]. Au:Ag bimetallic structures were deposited on glassy carbon electrodes to measure uric acid quantitatively by means of electrochemical-surface enhanced Raman spectroscopy (EC-SERS) [51]. SSV surfaces were already combined to spherical AgNPs in the so called particle-in-cavity (PIC) architectures. Extremely strong field enhancement were observed, $3.1 \cdot 10^4$ times more intense than the one produced by the bare cavities (Figure 1.13) [39,40]. Indeed, the cavities act effectively as light harvesters and the nanoparticles further focus the optical fields near the surface, enhancing dramatically the Raman effect. As already discussed, the Raman enhancement generated by isotropic nanomaterials can be increased by using nanoparticles with anisotropic geometries such as

AgNSs, as it was experimented in the context of this thesis by coupling the AgNSs to SSV surfaces (see Chapter 5).

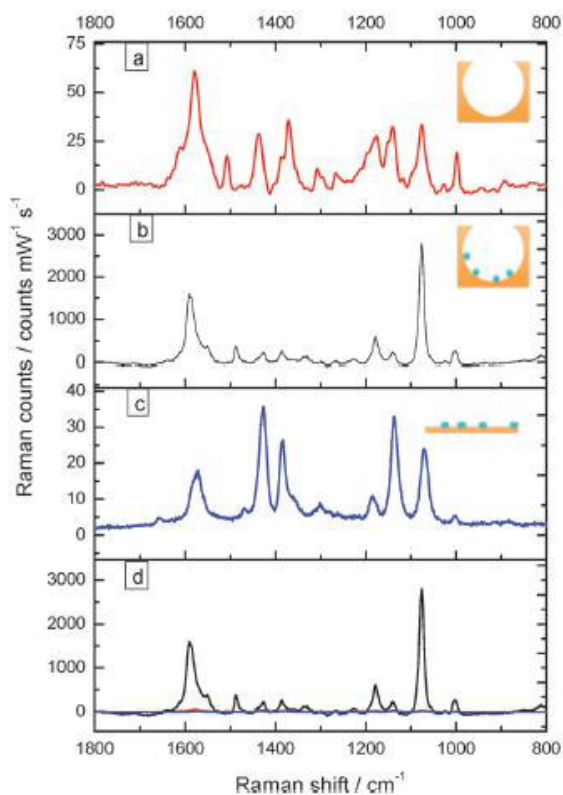


Figure 1.13 SERS spectra of 4-mercaptoaniline monolayer on a 600 nm SSV 0.75d substrate a) as such, b) after soaking in AgNP solution for 2h, c) on flat Au with NPs and d) all three spectra on the same scale to illustrate the differences in enhancements. Adapted from [39].

1.6 The application of SERS to Cultural Heritage

1.6.1 Identification of dyes and lake-pigments

By means of Raman spectroscopy most inorganic pigments can be identified, even *in situ*. Moreover, by coupling a microscope with the Raman spectrometer it is possible to operate on micro areas, enhancing the effectiveness of this technique [52,53]. However, due to the scarceness of the results when our target molecule is organic, like in the case of dyes, lakes and binders, using the SERS technique becomes necessary. On this basis, the SERS technique has been recently applied in

the field of cultural heritage to study organic colorants using different samples (solid micro-samples, fibres) taken from artistic objects (paintings, pottery, statues, textiles), while few studies have been devoted to the application of SERS on cross sections. In some preliminary studies, many colorants have been detected as pure molecules in solution [15,54,55], mock panels [15] and dyed fibres [15,56-58]. Lakes have been investigated as well. Lakes are complex colouring pigments in which an organic dye is adsorbed onto solid particles of inorganic salts. For instance, anthraquinone dyes such as cochineal, madder or kermes, when adsorbed onto alum particles, generate the relevant lakes (Figure 1.14). Particular attention has been given to the red lakes which have been studied in solution [56] and in real samples through the application of colloidal silver nanoparticles on grains of embedded pigments [53,59-61] and on sections of works of art [62].

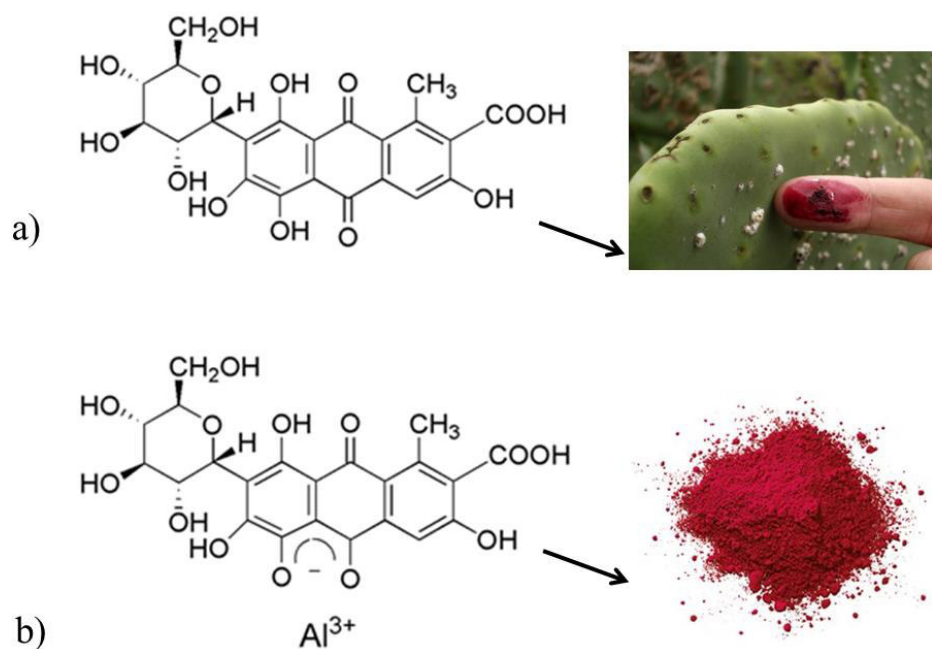


Figure 1.14 Structural formulas and examples of colouring application of carminic acid as a dye and as cochineal lake. Details: a) structural formula of carminic acid. This colorant is extracted from scale insects which live in waxy white coatings on cactus; b) interaction between carminic acid and Al^{III} ion from the KAl(SO₄)₂·12H₂O particles. In this way the colorant is fixed on an inorganic substrate and it can be used as red lake in paintings.

The nanoparticles most widely used for the SERS purpose are typically AgNPs prepared following the citrate reduction method proposed by P.C. Lee and D. Meisel [63]. This kind of SERS substrate was used to detect natural and synthetic colorants in solution [15,54,64] and in grains embedded in various binding media with a previous extraction or hydrolysis [59] or without [56,61]. It was also applied on pre-treated fibres [15,65] or on textile samples as such [56,58]. This Ag-based colloid was tested on mock panel as well [15,54] and on multi-layered real fragments taken from works of art [62]. However, for the preparation of AgNPs also other reducing agents were employed such as sodium borohydride [53] and hydroxylamine hydrochloride [15,55]. A particularly strong enhancement has been observed when anisotropic nanomaterials are employed, such as starry-shaped silver nanostars [19]. Photo-reduced AgNPs have been studied and used as well [15,66]. The photo-reduction process was performed directly on fibre without any previous extraction or hydrolysis procedure for the detection of flavonoids [67] and anthraquinone-based dyes [58]. Thin layer chromatography has been employed to separate dyes consequently analysed by *in situ* photo-reduced silver NPs from silver iodide (AgI) [68]. Up to now, few papers dealt with the characterization of colorants in painting cross sections. The studies carried out involved the detection of red lakes [69,70] and a chalcone dye [71]. The SERS substrate generally employed was citrate-reduced silver colloid and, in one case, an UV-photoreduced Ag colloid [72]. The SERS substrate was applied directly onto the cross section, apart from the last case in which its paint layer was laser-ablated and then the μ -sample was adsorbed onto an vapour-deposited Ag film [73].

1.6.2 SERS sensors for the detection of protein-based binders

As discussed in the introduction, a painting is a multilayer matrix and the pictorial layer itself is a complex system composed by pigments dispersed in a binding medium. The nature of the binder determines the working behaviour of the paint and the final characteristics of the work of art, not only from an aesthetic viewpoint, but also as far as durability and conservation are concerned.

Western artists have been using a variety of binders including animal glue, casein, egg, drying oils, resins, natural gums up to, more recently, synthetic materials such as acrylic and vinyl polymers. The detection of binders has long represented a fundamental issue in the study of cultural heritage materials. Vibrational spectroscopic techniques (e.g. IR and Raman spectroscopy) have been widely employed for a preliminary identification of the binders. However, their lack of specificity in the identification of the biological provenience of these macromolecules makes the use of chromatography (e.g. GC/MS and HPLC) necessary for a more precise diagnosis [1]. A valuable alternative is represented by the immunoassay approach. Indeed, the high specificity of the immunochemical bond between antigens and their antibodies is exploited to guarantee the precise recognition of the employed binders and embodies the focus of this method. The aim of this research path is to develop cheap, easy-to-use and the least invasive biosensors as diagnostic tools for conservators. Once established the key-lock bond, its presence can be revealed by many techniques, such as the electrochemical [74], colorimetric, fluorescent and chemiluminescent ones. Among the methods based on optical detection, the chemiluminescent approach gave the best results in terms of sensitivity. Indeed, the use of enzyme-labeled antibodies in the presence of a chemiluminescent substrate (e.g. horseradish peroxidase - HRP - reacts with luminol when hydrogen peroxides added, generating photons emission) allowed the simultaneous detection of ovalbumin [75] and casein on cross sections [76] of real samples. A promising alternative to this approach is represented by SERS, whose potentialities have not been exploited at their maximum yet. Indeed, NPs can be bound to specific antibodies for the target proteins and to a Raman-probe by means of functional thiols. In this way, the so called SERS nano-tags can be employed even directly on cross sections. Once bound onto the surface, the nano-tags are mapped using the SERS technique, revealing the distribution of the protein in the cross section [77,78] (Figure 1.15).

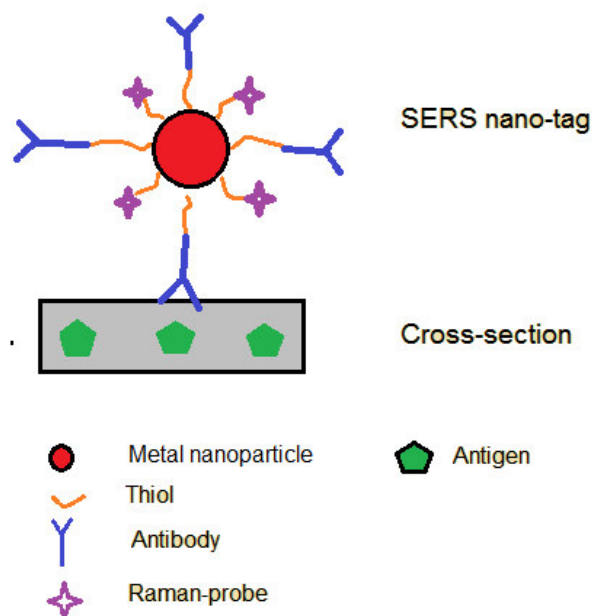


Figure 1.15 Scheme representing a SERS nano-tag. The NPs are functionalized by thiols to specific bond of the antibody for the target protein labelled by a Raman-probe to map the distribution of the protein.

Interesting prospects in this area can be opened by combining SERS detection with lateral flow immunoassay (LFIA) to substitute typical fluorescence detection methods [79]. A recently developed LFIA demonstrated the possibility to detect the presence two proteins (ovalbumin and collagen) in artworks at the same time, based on the use of disposable cartridges and a chemiluminescent detection system [80] (Figure 1.16).

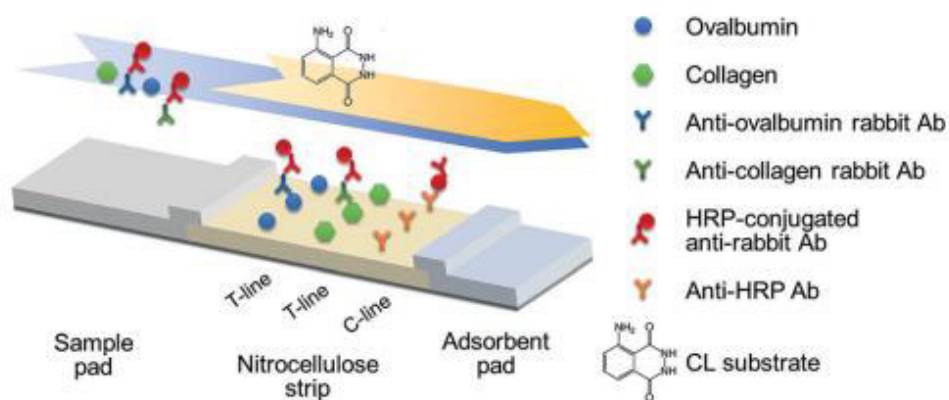


Figure 1.16 LFIA for the simultaneous detection of ovalbumin and collagen by means of a chemiluminescent revealing system. Adapted from [80].

The extraordinary positive results achieved by means of SERS make it an optimum candidate as a substitute detection technique in such an approach. Indeed, a SERS substrate immunochemically functionalized and labeled with a Raman-probe could represent a promising biosensor to be employed on site, taking advantage of the strong Raman enhancement produced by anisotropic Ag nanostars [19], able to create a larger number of SERS hot spots than spherical NPs. Moreover, in order to maximize the intensification of the electromagnetic field, Ag nanoparticles and nanostars can be deposited on gold nanostructures [32,38], creating complex nanomaterials hierarchically organized [39,40]. A so-organized portable device would offer a fast, user-friendly and effective solution to most on site diagnostics issues, not only in the field of cultural heritage, but also in medical, pharmaceutical and food industry contexts.

References

- [1] D. Pinna, M. Galeotti, and R. Mazzeo, *Scientific examination for the investigation of paintings. A handbook for restorers* **2011**, Centro Di Firenze, Italy.
- [2] C. Gaetani, G. Gheno, M. Borroni, K. D. Wael, L. M. Moretto, P. Ugo, *Electrochim. Acta* **2019**, *312*, 72.
- [3] M. P. Colombini, R. Fuoco, A. Giacomelli, B. Muscatello, *Stud. Conserv.* **1998**, *43 (1)*, 33.
- [4] W. Fremout, J. Sanyova, S. Saverwyns, P. Vandenabeele, L. Moens, *Anal. Bioanal. Chem.* **2009**, *393*, 1991.
- [5] D. R. Thevenot, K. Toth, R. A. Durst, G. S. Wilson, *Pure Appl. Chem.* **1999**, *71*, 2333.
- [6] M. Fleischmann, P.J. Hendra, A.J. McQuillan, *Chem. Phys. Lett.* **1974**, *26 (2)*, 163.
- [7] E.C. Le Ru, E. Blackie, M. Meyer, P.G. Etchegoin, *J. Phys. Chem. C* **2007**, *111 (37)*, 13794.
- [8] P. A. Mosier-Boss, *Nanomaterials* **2017**, *7*, 142.

- [9] R. Wiesinger, L. Pagnin, M. Anghelone, L. M. Moretto, E. F. Orsega, M. Schreiner, *Angew. Chem. Int. Ed.* **2018**, *57*, 7401.
- [10] S. Schlucker, *Surface Enhanced Raman Spectroscopy: Analytical Biophysical and Life Science Applications* **2011**, WILEY-VCH, Weinheim, Germany.
- [11] E. Le Ru, P.G. Etchegoin, *Principles of surface enhanced Raman spectroscopy and related plasmonics effects* **2009**, Elsevier, Oxford, United Kingdom.
- [12] P. Atkins, J. de Paula, *Chimica fisica* **2012**, Zanichelli, Bologna, Italy.
- [13] S. Schlucker ed., *Surface Enhanced Raman Spectroscopy: Analytical Biophysical and Life Science Applications* **2011**, Wiley-VCH, Weinheim, Germany.
- [14] R.F. Aroca, M.C. Vallete, J.V. García-Ramos, S. Sánchez-Cortés, J.A. Sánchez-Gil, P. Sevilla, *Amplificación plasmónica de espectros Raman y de fluorescencia SERS y SEF sobre nanoestructuras metálicas* **2014**, ed. CSIC, Madrid, Spain.
- [15] M.V. Canamares, *Espectroscopia Raman sobre superficies metálicas nanoestructuradas (SERS) aplicada al estudio de pigmentos del Patrimonio Histórico Artístico* Ph.D. thesis **2005**, Universidad Complutense de Madrid.
- [16] Y. Xie, D. Kocaeve, C. Chen, Y. Kocaeve, *Journal of Nanomaterials*, Volume **2016**, Article ID 2302595, 10 pages.
- [17] A. Guerrero-Martínez, S. Barbosa, I. Pastoriza-Santos, L.M. Liz-Marzan, *Curr. Opin. Colloid Interface Sci.* 2011,16, 118.
- [18] Y. Wang, P.H.C. Camargo, S.E. Skrabalak, H. Gu, Y. Xia, *Langmuir* 2008, 24, 12042.
- [19] A. García-Leis, J.V. García-Ramos, S. Sánchez-Cortés, *J. Phys. Chem. C* 2013, 117, 7791.
- [20] L. Rodríguez-Lorenzo, R.A. Alvarez-Puebla, I.Pastoriza-Santos, S. Mazzucco, O. Stéphan, M. Kociak, L.M. Liz-Marzán, F.J. García de Abajo, *J. Am. Chem. Soc.* **2009**, *131*, 4616.

- [21] L. Litti, J. Reguera, F.J. García de Abajo, M. Meneghetti, L.M. Liz-Marzán, *Nanoscale Horiz.* **2019**.
- [22] G.E. Possin, *Rev. Sci. Instrum.* **1970**, *41*, 772.
- [23] W.D. Williams, N. Giordano, *Rev. Sci. Instrum.* **1984**, *55*, 410.
- [24] R.M. Penner, C.R. Martin, *Anal. Chem.* **1987**, *59*, 2625.
- [25] J.W. Diggle, T.C. Downie, C.W. Goulding, *Chem. Rev.* **1969**, *69*, 365.
- [26] P. Apel, *Radiat. Meas.* **2001**, *34*, 559.
- [27] M. Wirtz, C.R. Martin, *Adv. Mater.* **2003**, *15*, 455.
- [28] V.P. Menon, C.R. Martin, *Anal. Chem.* **1995**, *67*, 1920.
- [29] M. De Leo, F.C. Pereira, L.M. Moretto, P. Scopece, S. Polizzi, P. Ugo, *Chem. Mater.* **2007**, *19*(24), 5955.
- [30] M. De Leo, A. Kuhn, P. Ugo, *Electroanalysis* **2007**, *19*(2-3), 227.
- [31] S. Yu, N. Li, J. Wharton, C. R. Martin, *Nano Lett.* **2003**, *3*(6), 815.
- [32] P. Ugo, L.M. Moretto, *Template Deposition of Metals. In C. Zosky (ed.), Handbook of Electrochemistry*, **2007**, chapter 16.2, Elsevier, Amsterdam, The Netherlands.
- [33] A.M. Stortini, L.M. Moretto, A. Mardegan, M. Ongaro, P. Ugo, *Sens. Actuator B-Chem.* **2015**, *207*, 186.
- [34] T.M. Whitney, P.C. Searson, J.S. Jiang, C.L. Chien, *Science* **1993**, *261*, 1316.
- [35] L.M. Moretto, M. Tormen, M. De Leo, A. Carpentiero, P. Ugo, *Nanotechnology* **2011**, *22*, 185305.
- [36] N.G. Tognalli, A. Fainstein, E.J. Calvo, M. Abdelsalam, P.N. Bartlett, *J. Phys. Chem. C* **2012**, *116*, 3414.

- [37] A. Celiktas, M.A. Ghanem, P.N. Bartlett, *J. Electroanal. Chem.* **2012**, 670, 42.
- [38] S. Mahajan, R.M. Cole, B.F. Soares, S.H. Pelfrey, A.E. Russell, J.J. Baumberg, P.N. Bartlett, *Phys. Chem. C* **2009**, 113(21), 9284.
- [39] J.D. Speed, R.P. Johnson, J.T. Hugall, N.N. Lal, P.N. Bartlett, J.J. Baumberg, A.E. Russell, *Chem. Commun.* **2011**, 47, 6335.
- [40] F.M. Huang, D. Wilding, J.D. Speed, A.E. Russell, P.N. Bartlett, J.J. Baumberg, *Nano Lett.* **2011**, 11, 1221.
- [41] Y. Zhao, X. Li, Y. Liu, L. Zhang, F. Wang, Y. Lu, *Sens. Actuators B* **2017**, 247, 850.
- [42] W.J. Anderson, K. Nowinska, T. Hutter, S. Mahajan, M. Fischlenchner, *Nanoscale* **2018**, 10, 7138.
- [43] L. Litti, N. Rivato, G. Fracasso, P. Bontempi, E. Nicolato, P. Marzola, A. Venzo, M. Colombatti, M. Gobbo, M. Meneghetti, *Nanoscale* **2018**, 10, 1272.
- [44] X. Guo, Z. Guo, Y. Jin, Z. Liu, W. Zhang, D. Huang, *Microchim. Acta* **2012**, 178, 229.
- [45] M. Ongaro, A. Gambirasi, M. Favaro, P. Ugo, *Electrochim. Acta* **2012**, 78, 539.
- [46] K. Kim, J.K. Yoon, *J. Phys. Chem. B* **2005**, 109, 20731.
- [47] H. Tang, G. Meng, Q. Huang, Z. Zhang, Z. Huang, C. Zhu, *Adv. Funct. Mater.* **2012**, 22, 218.
- [48] S. Park, J. Lee, H. Ko, *ACS Appl. Mater. Interfaces* **2017**, 17, 44088.
- [49] Q. Zhang, Y.H. Lee, I.Y. Phang, C.K. Lee, X.Y. Ling, *Small* **2014**, 10 (31), 2703.
- [50] C.Y. Fu, K.W. Kho, U.S. Dinish, Z.Y. Kohe, O. Malini, *J. Raman Spectrosc.* **2012**, 43, 977.
- [51] L. Zhao, J. Blackburn, C.L. Brosseau, *Anal. Chem.* **2015**, 87, 441.
- [52] C. Clementi, V. Ciocan, M. Vagnini, B. Doherty, M. L. Tabasso, C. Conti, B. G. Brunetti, C. Miliani, *Anal. Bioanal. Chem.* **2011**, 401, 1815.
- [53] E.V. Elslande, S. Lecomte, A.L. Ho, *J. Raman Spectrosc.* **2008**, 39 (8), 1001.
- [54] M. Leona, J. Stengerand, E. Ferloni, *J. Raman Spectrosc.* **2006.**, 37(10), 981.

- [55] M.V. Cañamares, M. Leona, *Lasers in the Conservation of Artworks* **2008**, Taylor & Francis Group, London.
- [56] C.L. Brosseau, A. Gambardella, F. Casadio, C.M. Grzywacz, J. Wouters, R.P.V. Duyne, *Anal. Chem.* **2009**, *81*, 7443.
- [57] K.L. Wustholz, C.L. Brosseau, F. Casadio, R.P. Van Duyne, *Phys. Chem. Chem. Phys.* **2009**, *11*, 7350.
- [58] Z. Jurasekova, E. del Puerto, G. Bruno, J.V. García-Ramos, S. Sánchez-Cortés, C. Domingo, *J. Raman Spectrosc.* **2010**, *41(11)*, 1455.
- [59] F. Pozzi, J.R. Lombardi, M. Leona, *Heritage Sci.* **2013**, *1*, 23.
- [60] C.L. Brosseau, K.S. Rayner, F. Casadio, C.M. Grzywacz, R.P. Van Duyne, *Analytical Chemistry* **2009**, *81*, 7443.
- [61] C.L. Brosseau, F. Casadio, *J. Spectrosc.*, **42**, 1305 (2011).
- [62] C. Daher, L. Drieu, L. Bellot-Gurlet, A. Percot, C. Paris, A. L. Hô, *J. Raman Spectrosc.* **2013**, *45(11-12)*, 1207.
- [63] P.C. Lee, D. Meisel, *J. Phys. Chem.* **1982**, *86*, 3391.
- [64] J. Chang, M. V. Cañamares, M. Aydin, W. Vetter, M. Schreiner, W.Q. Xu, J.R. Lombardi, *J. Raman Spectrosc.* **2009**, *40(11)*, 1557.
- [65] M. V. Cañamares, M. Leona, M. Bouchard, C.M. Grzywacz, J. Wouters, K. Trentelman, *J. Raman Spectrosc.* **2010**, *40(4)*, 391.
- [66] Z. Jurasekova, S. Sánchez-Cortés, M. Tamba, A. Torregiani, *Vib. Spectrosc.* **2011**, *57*, 42.
- [67] Z. Jurasekova, C. Domingo, J.V. García-Ramos, S. Sánchez-Cortés, *J. Raman Spectrosc.* **2008**, *39*, 1309.
- [68] G. Sciutto, S. Prati, I. Bonacini, L. Litti, M. Meneghetti, R. Mazzeo, *Anal. Chim. Acta* **2017**, *991*, 04.
- [69] A. Idone, M. Aceto, E. Diana, L. Appolonia, M. Gulmini, *J. Raman Spectrosc.* **2014**, *45(11-12)*, 1127.
- [70] K. A. Frano, H. E. Mayhew, S.A. Svoboda, K.L. Wustholz, *Analyst* **2014**, *139*, 6450.
- [71] A. Daveri, B. Doherty, P. Moretti, C. Grazia, A. Romani, E. Fiorin, G. Brunetti, M. Vagnini, *Spectrochim. Acta Part A* **2015**, *135*, 398.
- [72] K. Retko, P. Ropreta, R.C. Korošec, *J. Raman Spectrosc.* **2014**, *45(11-12)*, 1140.
- [73] A. Cesaratto, M. Leona, J. R. Lombardi, D. Comelli, A. Nevin, P. Londero, *Angew. Chem.* **2014**, *53(52)*, 14373.
- [74] F. Bottari, P. Oliveri, P. Ugo, *Biosens. Bioelectron.* **2014**, *52*, 403.

- [75] M. Zangheria, M. Mirasoli, S. Prati, R. Mazzeo, A. Roda, M. Guardigli, *Microchem. J.* **2016**, *124*, 247.
- [76] G. Sciutto, L. S. Dolci, A. Buragina, S. Prati, M. Guardigli, R. Mazzeo, A. Roda, *Anal. Bioanal. Chem.* **2011**, *399*, 2889.
- [77] J. Arslanoglu, S. Zaleski, and J. Loike, *Anal. Bioanal. Chem.* **2011**, *399*, 2997.
- [78] G. Sciutto, L. Litti, C. Lofrumento, S. Prati, M. Ricci, M. Gobbo, A. Roda, E. Castellucci, M. Meneghetti, R. Mazzeo, *Analyst* **2013**, *138*, 4532.
- [79] L. Cartechini, M. Vagnini, M. Palmieri, L. Pitzurra, T. Mello, J. Mazurek, G. Chiari, *Acc. Chem. Res.* **2010**, *43(6)*, 867.
- [80] G. Sciutto, M. Zangheri, L. Anfossi, M. Guardigli, S. Prati, M. Mirasoli, F. D. Nardo, C. Baggiani, A. Roda, *Angew. Chem.* **2018**, *130(25)*, 7507.

Chapter 2

Preparation of Ag nanostars and first applicative tests

Part A: Preparation of Ag nanostars for SERS measurements

2.1 Introduction

The SERS technique is widely employed in different fields to detect several substances by enhancing their Raman signals. Various types of silver and gold nanomaterials can be employed as SERS substrates. As introduced in Chapter 1, remarkable amplification effects are produced by anisotropic star-shaped nanostructures such as Au [1] and Ag [2,3] nanostars. Due to their starry shape composed of a central core and many pods, these particular nanoparticles are expected to absorb UV-Vis light in different spectral regions, namely around 380 nm and towards the near infrared region. In this way, not only the generation of SERS hot spots is promoted when excited with red-light laser beams but also enhancements of the Raman effect up to 10^8 are observed [4,5]. This is thanks to the presence of tips which are responsible for the SERS efficiency while the enhancement at the spherical core is two orders of magnitude smaller (Figure 2.1) [6].

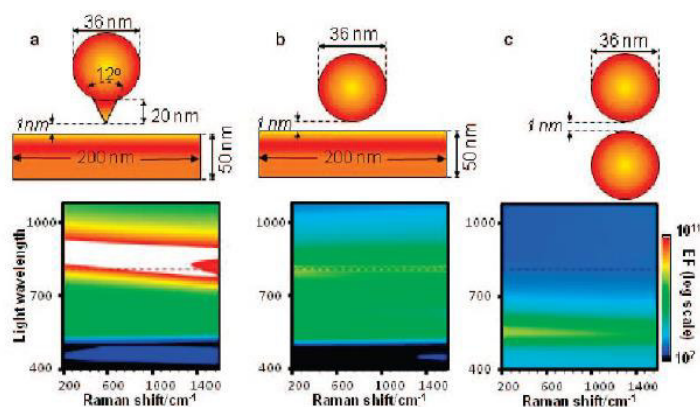


Figure 2.1 Calculated SERS enhancement factors as a function of Raman shift and laser wavelength for three different nanostructured Au configurations, schematically represented: a) a

sphere with a tip near a plate, b) a sphere near a plate and c) a Au sphere dimer. At the bottom: measured and calculated enhancement factors for all these systems at selected Raman bands. Adapted from [6].

Gold and silver nanostars (Au/AgNSs) can be obtained employing different reagents and reduction methodologies. AuNSs were synthesized by seeded-growth method, through the chemical reduction of the metallic precursor (HAuCl_4) by means of ascorbic acid, hydroxylamine and dimethylformamide - DMF - with a capping agent (cetyl-trimethylammonium bromide - CTAB -, citrate, polyvinylpyrrolidone – PVP -) and additive (AgNO_3) [4,7,8]; by one-pot synthesis, using citrate and ascorbic acid, in the presence of a capping agent (thiols, PVP) and additive (NaOH) [9,10]; by electrosynthesis without [11] and with [12] in the presence of a templating agent. AgNSs were prepared carrying out reduction of $\text{Ag}(\text{NH}_3)_2$ with ascorbic acid, in the presence of silver seeds and PVP as stabilizer and citrate as reaction trigger [13], or by one-pot synthesis [14]. In particular, this last method appeared a valuable option due to its feasibility and reproducibility. The protocol described by A. García-Leis *et al.* [3], adopted in the experimental context of this thesis, involves the reduction of the metallic precursor (AgNO_3) by a reducing agent (hydroxylamine) in the presence of a capping agent (trisodium citrate) and additive (NaOH). In the first part of this Chapter, the spectral characteristics and analytical performances of AgNSs are compared to those of spherical silver nanoparticles (AgNPs). Benzenethiol (BT), used as SERS probe, was adsorbed on the structures and relevant Raman spectra recorded and compared with SERS signals obtained on flat macro-gold with or without AgNPs or AgNSs. Experimental results indicate that the largest SERS enhancement is observed when BT is bound onto AgNSs, confirming this kind of SERS substrate can be effective for the sensitive SERS detection of adsorbed organics, even of complex structure, such as dyes and lake-pigments employed in the field of cultural heritage. Indeed, a case study is exposed in the second part of Chapter 2, illustrating how AgNSs can be applied to a cross section of a real painting for diagnostics purposes.

2.2 Materials and methods

2.2.1 Materials

All the chemicals used in the preparation of the AgNSs were purchased from Sigma-Aldrich. Silver nitrate (AgNO_3); sodium citrate tribasic dihydrate ($\text{C}_6\text{O}_7\text{H}_5\text{Na}_3 \times 2\text{H}_2\text{O}$); sodium hydroxide (NaOH); hydroxylamine in solution (NH_2OH ; 50% w/v in water). The flat macro-gold slides were made by a specialized lab by vapor deposition of a 10 nm chromium adhesion layer followed by 200 nm of gold onto standard glass microscope slides.

2.2.2 Synthesis of Ag nanostars

AgNSs were synthesized according to the method proposed by A. García-Leis *et al.* [3]. Four solutions are required:

- Sodium hydroxide solution: NaOH (0.02 g) dissolved in milliQ water (10 mL) to get a 0.05 M solution.
- Hydroxylamine solution: NH_2OH (18 μL) at 50% w/v in milliQ water (5 mL).
- Silver nitrate solution: AgNO_3 (0.0017 g) dissolved in milliQ water (10 mL) to obtain a $1 \cdot 10^{-3}$ M solution.
- Trisodium citrate solution: of $\text{C}_6\text{H}_5\text{O}_7\text{Na}_3 \cdot 2\text{H}_2\text{O}$ (0.114 g) is dissolved in milliQ water (10 mL) to get a 0.045 M solution.

500 μL of the NaOH and 500 μL of the hydroxylamine solutions are mixed in a flask and stirred at 670 rpm with magnetic stirrer for one minute. Then, 9 mL of the AgNO_3 solution are added and the mixture is kept under stirring for 5 minutes. Afterwards, 100 μL of the citrate solution are dropped in the flask, stirring for approximately 15 minutes, i.e. up to acquire a dark green color. The reduction of Ag^+ ions is operated by hydroxylamine but this process, led at room temperature, is very slow. In order to make the long arms of these spiky nanoparticles grow faster citrate is added. The complete growth of the star-shaped NPs, starting from a spherical faceted morphology, takes more or less 48 hours.

2.2.3 Synthesis of Ag nanospheres

AgNPs were synthesized colloid adapting the method described by P.C. Lee and D. Meisel [15,16]. Briefly, $1 \cdot 10^{-3}$ M AgNO_3 solution is heated up to boiling then, 1 mL of 0.045 M trisodium citrate solution is added and the mixture is kept under reflux at around 100 °C for one hour. During this procedure, a colloidal dispersion is formed, assuming a matt appearance and a light beige color.

2.2.4 Preparation of the samples for the Raman analysis

The macro-gold slides employed for the benzenethiol (BT) (Figure 2.2) [17,18] detection were treated as follows:

1. overnight immersion in 10 mM cysteamine water solution [19,20];
2. overnight immersion in the colloidal suspension of nanoparticles (AgNPs or AgNSs);
3. overnight immersion in 10^{-2} mM BT ethanolic solution [21].

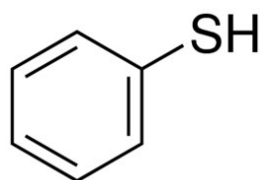


Figure 2.2 Structural formula of benzenethiol.

2.2.6 Instrumentation

SERS and Raman spectroscopy

The Raman spectra were measured on macro-gold, with or without Ag nanospheres and AgNSs, using a handheld Metrohm Raman spectrometer model MIRA M-3, 785 nm laser at its maximum power (100 mW). The post-processing of the spectra was performed with the OriginLab software.

UV-Visible absorption spectroscopy

UV-Vis absorbance spectra were recorded with a Perkin-Elmer Lambda 40 spectrophotometer equipped with a Peltier-Elmer PTP6 (Peltier temperature programmer) apparatus. The Ag colloids samples were diluted 1:3 in water.

Transmission electron microscopy (TEM)

Transmission electron microscopy (TEM) and high resolution TEM (HRTEM) images were measured using a JEOL 3010 high resolution electron microscope (0.17 nm point-to-point resolution at Scherzer defocus), operating at 300 kV, equipped with a Gatan slow-scan CCD camera (model 794) and an Oxford Instrument EDS microanalysis detector Model 6636. Drops of colloidal solutions were deposited on Holey-Carbon Copper grids and let dry at room temperature before analysis.

Field-emission scanning electron microscopy (FE-SEM)

The SEM analysis were performed using a Sigma-VP Carl Zeiss field-emission scanning electron microscope. Solid samples were immobilized on stubs by means of conductive tape in order to prevent the charging of the surfaces.

Dynamic light scattering (DLS)

The DLS measurements [22] were performed at room temperature with a Zetasizer Nano ZS (Malvern Instruments) equipped with a green laser ($\lambda = 532$ nm) and backscatter detector at 175° . The average size was evaluated as an intensity distribution. This analysis gives a good description of the size that is comparable with other methods of analysis for spherical and monomodal samples, *i.e.* with polydispersity below a value of 0.1.

2.3 Results and discussion

2.3.1 Synthesis and characterization of AgNSs and AgNPs by UV-Vis spectroscopy, dynamic light scattering and field emission - scanning electron microscopy

Figure 2.3 shows the absorption spectra of the colloidal suspension of AgNSs [16] prepared at three different pH values, while their macroscopic optical properties and TEM images are shown in Figure 2.4. The results obtained indicate that a slightly acidic pH (≈ 6.6) prevents the formation of any colloids (Figure 2.3-a), as confirmed by the transparent suspension obtained (Figure 2.4-i). A slightly basic pH (≈ 8.1) generates a colloid whose spectrum is characterized by a band at around 370 nm followed by a light but progressive increase in absorbance which starts approximately for $\lambda > 550$ nm (Figure 2.3-b). Comparison with the literature supports the formation of AgNS since the absorption at 370 nm can be due to the core while the broad increase in absorbance at longer wavelengths can be attributed to the tips [17]. This colloid presents a dark green color (Figure 2.4-i) and, as shown by TEM analysis, is indeed composed by a monodisperse suspension of AgNSs (Figure 2.4-ii). Eventually, the colloidal suspension at strongly basic pH value (≈ 11.4) shows an absorption spectrum which presents a strong band at 430 nm and a shoulder at 380 nm (Figure 2.3-c). Its color is greyish-beige (Figure 2.4-i) and the TEM image reveals a polydisperse system, composed by AgNSs and nanospheres (Figure 2.4-iii). Elemental microanalysis confirmed Ag as the main element present in the samples.

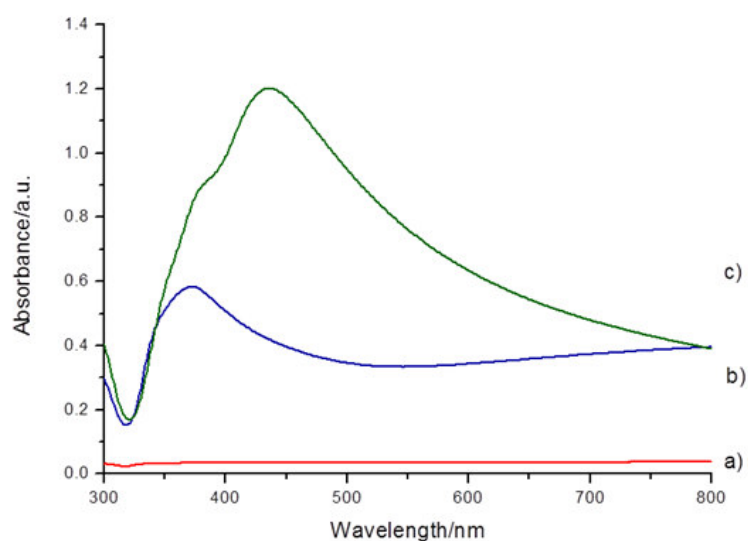


Figure 2.3 UV-Vis absorption spectra of AgNSs prepared at different pH values: a) pH 6.6, b) pH 8.1, c) pH 11.4.

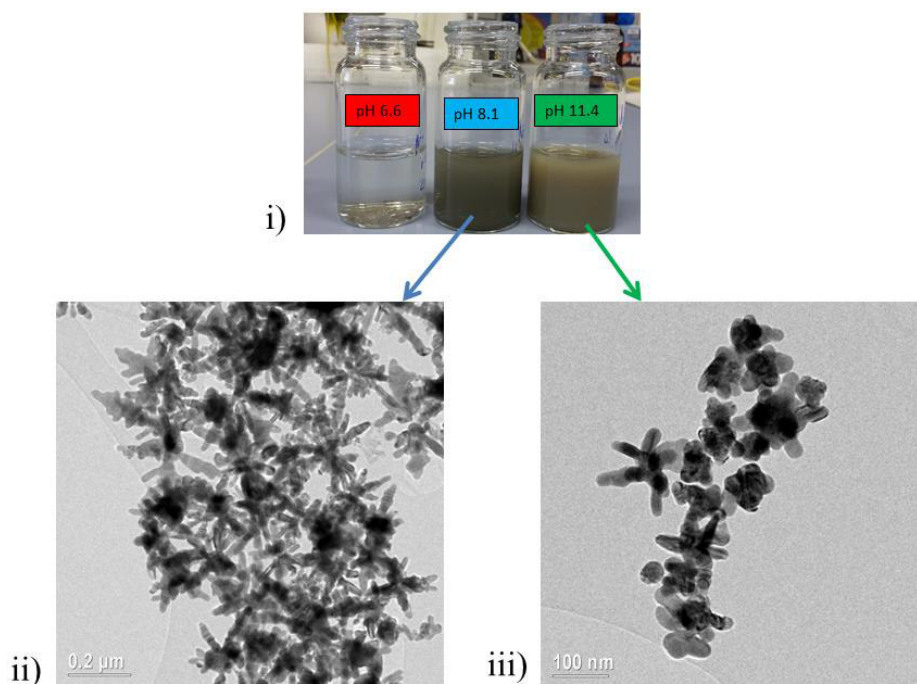


Figure 2.4 i) Photograph showing the macroscopic appearance of the colloidal suspension of Ag nanoparticles obtained at the indicated pH, namely from left pH 6.6, 8.1, 11.4; TEM images of the nanoparticles obtained at ii) pH 8.1 and iii) pH 11.4.

For comparison purposes (see below), silver nanoparticles of quasi-spherical shape are prepared by reduction of AgNO_3 with trisodium citrate [15,16] obtaining NPs with an average diameter of 20-50 nm which tend to assume a polyhedral shape (see Figure 2.5-A). Relevant UV-Vis spectrum (Figure 2.6) is characterized by a sharp maximum of absorbance at around 430 nm with absorbance going to zero for approximately $\lambda \approx 600$ nm, in agreement with the literature [16]. Figure 2.5-B shows the TEM images of a typical AgNS obtained at pH 8.1, which presents a central core of around 50 nm as diameter and a variable number of pods arranged in an octahedral structure reaching an overall dimension of approximately 200 nm. The growth starts from spherical seeds of Ag reduced by hydroxylamine, then, in the following 48 hours, the pods start taking shape thanks to the presence of citrate ions that direct the growth of the branches [16].

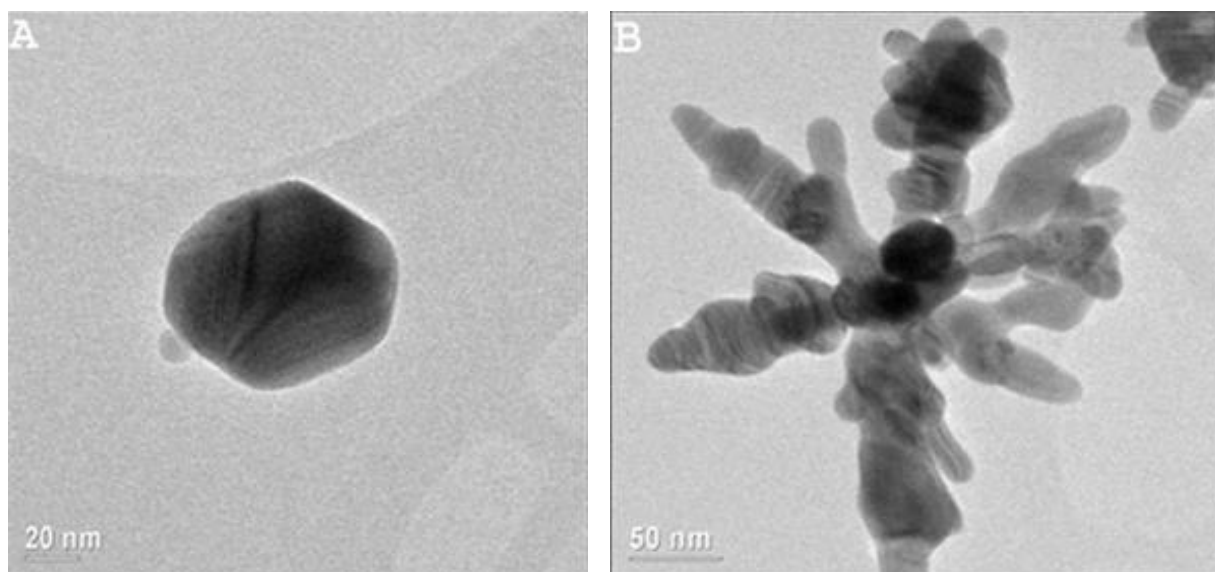


Figure 2.5 TEM images of A) a Ag nanosphere; B) a AgNS.

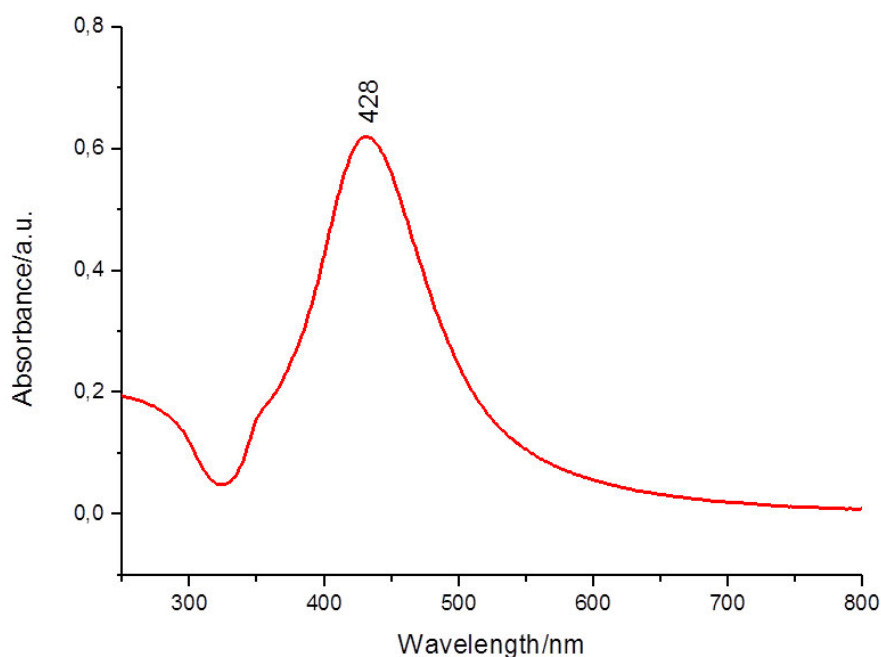


Figure 2.6 UV-Vis absorption spectrum of AgNPs, characterized by the absorption maximum at around 430 nm.

The average size, the polydispersity and the zeta potential are evaluated by using dynamic light scattering (DLS) measurements [22]. Figure 2.7 presents the size distribution reported as intensities, showing an average diameter of 200 nm for the AgNSs (Figure 2.7-a) and 70 nm for the AgNPs (Figure 2.7-b). The polydispersity index (PdI) presents a lower value for the nanospheres (0.258) and a higher value for the nanostars, in agreement with their simpler and better defined shape (0.504). Both AgNSs and AgNPs exhibit a negative zeta potential, -44 and -33 mV respectively, which can be attributed to the presence of residual citrate on their surface. This feature agrees with the observed stability of the obtained colloidal dispersions of AgNPs and AgNSs, which do not aggregate.

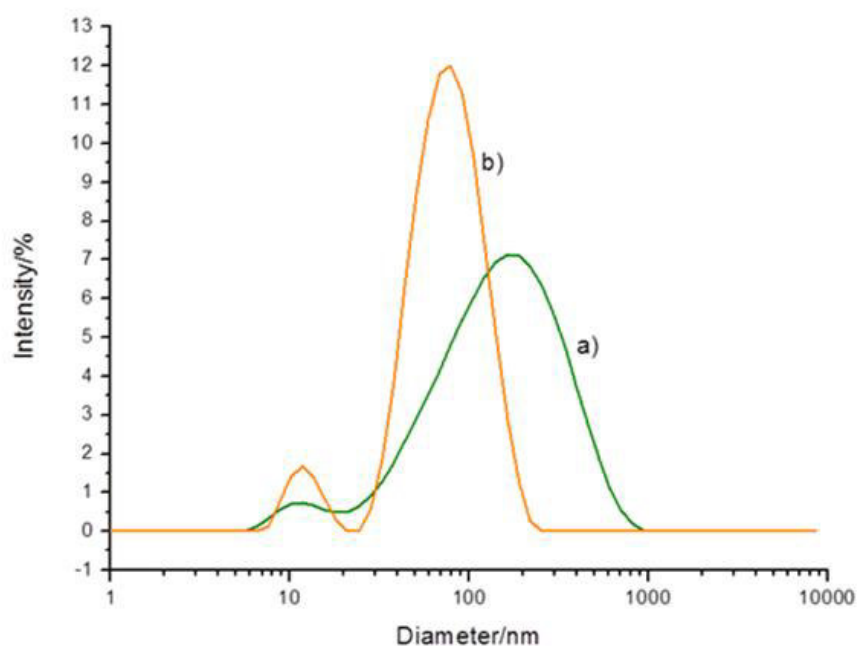


Figure 2.7 Dynamic light scattering experimental results presenting the size distribution by intensity of a) AgNSs and b) AgNPs.

2.3.2 SERS characterization with benzenethiol as Raman probe

The efficiency of several SERS substrates was assessed by employing benzenethiol (BT) as reference Raman-probe [17,18] whose Raman bands are well known from the literature (see Table 2.1 for detailed information) [23].

Table 2.1 Main SERS bands of BT and their assignments [23].

Raman shift/cm ⁻¹	BT vibrational mode
420	C-S stretching and ring in-plane deformation
690	Ring in-plane deformation and C-S stretching
998	Ring out-of-plane deformation and C-H out-of-plane bending
1021	Ring in-plane deformation and C-C symmetric stretching
1071	C-C asymmetric stretching and C-S stretching
1571	C-C symmetric stretching

The Raman enhancement produced by the AgNPs and AgNSs was at first tested depositing the colloid on flat gold surfaces, named hereafter macro-gold. These substrates were modified through overnight immersion in cysteamine solution [19,20], followed by incubation in the colloidal AgNPs and eventually in the 10^{-2} mM BT solution in ethanol [21]. Raman spectra recorded on decorated and undecorated samples indicates that BT is not detected by Raman spectroscopy on the macro-gold layer (Figure 2.8-a) and even the addition of AgNPs allowed observing only very weak signals (Figure 2.8-b). Instead, SERS signals were significantly enhanced when the macro-gold surface was decorated with AgNSs (Figure 2.8-c). Recorded SERS spectra presented indeed the typical bands of BT: 1575 (s), 1072 (s), 1022 (s), 1002 (s), cm^{-1} (in black). Moreover it was possible to detect the presence of cysteamine (bands at 815 and 610 cm^{-1} , in green) [24] and citrate (bands at 1360 and 928 cm^{-1} , in orange) [25] used for the preparation of the nanostructures.

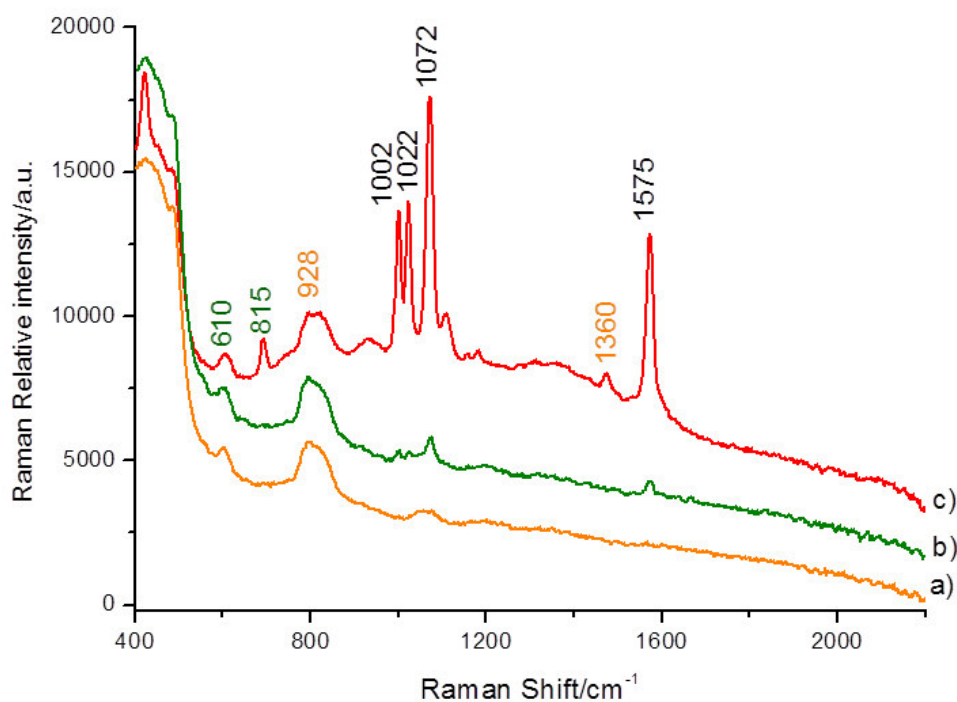


Figure 2.8 Raman spectra of benzethiol adsorbed from a 10^{-2} mM solution onto: a) flat gold layer functionalized by cysteamine; b) flat gold + AgNPs and c) flat gold + AgNSs. The main bands of BT are marked in black, citrate in orange and cysteamine in green ($\lambda_{\text{ex}} = 785$ nm, $P = 100$ mW).

2.3.3 Summary

Both the two different kinds of nanomaterials here synthesized and characterized with focus on their SERS, namely AgNPs and AgNSs, proven to be efficient enhancers of Raman signals for BT. However, the direct comparison of SERS signals indicates a higher efficiency for the AgNSs, which seems related to their anisotropic shape. On account of their better performances, AgNSs represent the perfect candidate to be applied for sensitive analyses of artistic materials.

Part B: Application of AgNSs: case study

2.4 Case study: “*Madonna della Misericordia*” from the National Gallery of Parma

2.4.1 Introduction

This part of my thesis work was developed thanks to a traineeship at the restoration laboratory of the National Gallery of Parma, under the supervision of Dr. Ines Agostinelli. Aim of this stage was, besides learning the main restoration techniques, the collection and the analytical study of real samples from different works of art. In particular, the attention was focused on the *Madonna della Misericordia* which needed an intervention of restoration and scientific analyses to provide a more precise historical background and knowledge of the technique and materials used by the painter and/or during previous restoration interventions. This painting, oil on panel, 192 x 82 cm, represents Virgin Mary housing under her mantle the clients, two ladies and two gentlemen, kneeling at her right and left, respectively. It is completed by a painted neo-gothic frame characterized by two lateral *paraste*, a central rose and a *predella* decorated by three saints (Figure 2.9).

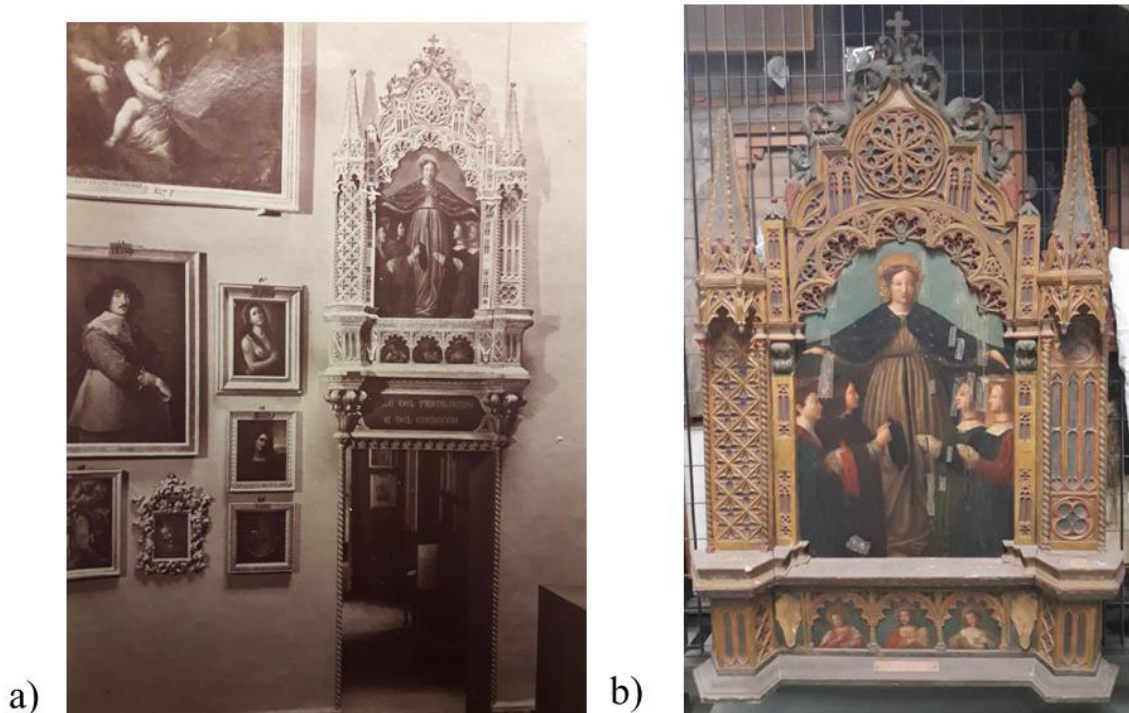


Figure 2.9 Pictures showing the *Madonna della Misericordia* a) at the entrance of Parmigianino and Correggio's display rooms in the 19th century and b) in the picture gallery where it has been displayed until 2018.

This painting arrived to the Gallery in 1868, coming from the Cappuccini's monastery in Borgo Santa Chiara, Parma [26]. The director of the Gallery, Corrado Ricci, attributed this painting to an anonymous painter belonging to the school of Cremona of the 15th century [27]. However, many doubts about this interpretation arose due to many stylistic and technical incongruences which suggest to postdate it to the 19th century [28], also due to the evidence of important restoration interventions (Japanese paper on cracks, re-paintings, etc.) carried out in 1896 [27] and in 1951 [28]. In order to solve this issue, the contribute of scientific analysis was desirable. In the following section, the main results obtained will be presented with the aim of answering to the exposed matter.

2.4.2 Materials and methods

Infrared reflectography

The IR reflectography analysis was performed by using a Hamamatsu vidicon tube camera.

UV fluorescence

A commercial Wood lamp was employed to assess the UV fluorescence emitted by the painting.

SEM-EDS

Scanning electron microscopy (SEM) and energy dispersive spectroscopy (EDS) analysis on the cross sections were performed at the University Ca' Foscari of Venice (Department of Molecular Sciences and Nanosystems), using a TM3000 Hitachi tabletop scanning electron Microscope coupled with a X-ray microanalysis system (SwiftED3000); conditions for recording the EDS spectra were: acquisition time 30.0 s; process time 5 s; accelerating voltage 15 kV.

μ -Raman spectroscopy

The SERS measurements were performed during a following stage at the University of Southampton, at the School of Chemistry. A Renishaw 2000 Raman spectrometer was employed to carry out the Raman and SERS measurements. The excitation laser employed was a Renishaw 785 nm laser and a CCD detector. The maximum power of the laser is 100 mW but lower powers were used during the data acquisition, typically 0.05% and 1% (0.05 and 1 mW). The collection time was 10 s for one accumulation. The spectrometer was equipped with a Leica DMLM series microscope. In order to collect scattered light at the sample, a microscope objective with a 50X magnification was employed with a short working distance (0.37 mm-numerical aperture 0.75).

Preparation of the cross sections

The cross sections were sampled with a scalpel, cutting triangular millimetric fragments containing all the layers composing the painting. Then they were placed into cells of a silicon rubber mold on an already hardened resin layer. At this point, the embedding resin was prepared under the fume hood using some mL of unsaturated orthophthalic polyester resin (purchased from G. Angeloni,

Venice) and few drops of hardener (methyl-ethyl-ketone peroxide). The components were stirred until the mixture was completely homogenous. Eventually, the resin was poured into the cells and left dry for two days. Once the resin cured, the polishing procedure started. The cross sections were polished manually using silicon carbide cards with decreasing grain sizes. Different grit size cards were used (P120-P500-P800-P4000-P6000-P8000-12000, of an average size from 130 to 4 μm) and progressively replaced into the lapping machine, equipped with a magnetic rotating disk and water cooling system, from the coarsest to the finest one. The sections were pressed onto the abrasive papers for some minutes and frequently observed at the stereomicroscope to check the level of polishing. This procedure ended when the samples were reached from the long side of the resin blocks.

Ag nanostars colloid: preparation and application onto the sample

AgNSs were synthesized according to the recipe followed by A. García-Leis *et al.* [21] (see Chapter 2-Part A). Therefore, the colloidal solution of AgNSs was concentrated by centrifuging three times at 8000 rpm for 5 minutes in a 1.5 mL Eppendorf centrifuge tube from 500 μL of colloid. After each centrifugation step 400 μL of supernatant were removed and replaced by the same quantity of colloid. Before centrifuging, nanoparticles which got stuck at the bottom, were dispersed again in order to eliminate interfering salts. After this procedure, 2 μL of the concentrated AgNSs dispersion were deposited on the cross section by means of a micropipette. Once completely dried, the sample was ready to be analyzed through a μ -Raman spectrometer.

2.4.3 Cross sections analysis

The preliminary analyses were fundamental to plan the sampling areas. Indeed, mapping the retouched areas in the original painting is necessary to avoid them during the sampling. Seven cross sections were sampled from the painting and the *predella*, and six from the frame. Each one was taken in order to answer to specific questions about the materials employed in every layer of the

stratigraphy in those precise points (Figure 2.10). For the sake of brevity, only the most important and relevant results are exposed.



Figure 2.10 Sampling map of the cross sections (CS) in the a) panel and b) frame (CS5 frame is an erratic sample, analysis not shown).

Bluish background (CS7): an exemplificative study

The study of CS7, sampled in the bluish background behind Virgin Mary and the clients, is the most exemplificative in the context of my thesis and, for this reason, it is exposed as keystone to interpret the painting and its story.

Figure 2.11-a shows the exact area from CS7 was sampled and, once embedded in a polyester resin block, it was analyzed at the stereomicroscope (Figure 2.11-b). and optical microscope in reflected light (Figure 2.11-c). At high magnifications (50X), all the layers composing the painting are visible. Starting from the bottom, we can find the ground layer, generally made of gypsum and animal glue, which is necessary to make even and homogeneous the support, in this case the wood panel. Then, it is possible to note the paint layer made of a mixture of blue and white grains. The peculiar feature is that this sequence is repeated: a new ground and paint layer were added on the

original ones in more recent times. Apparently, they may be composed by the same materials, but this must be investigated by means of elemental and molecular analyses.

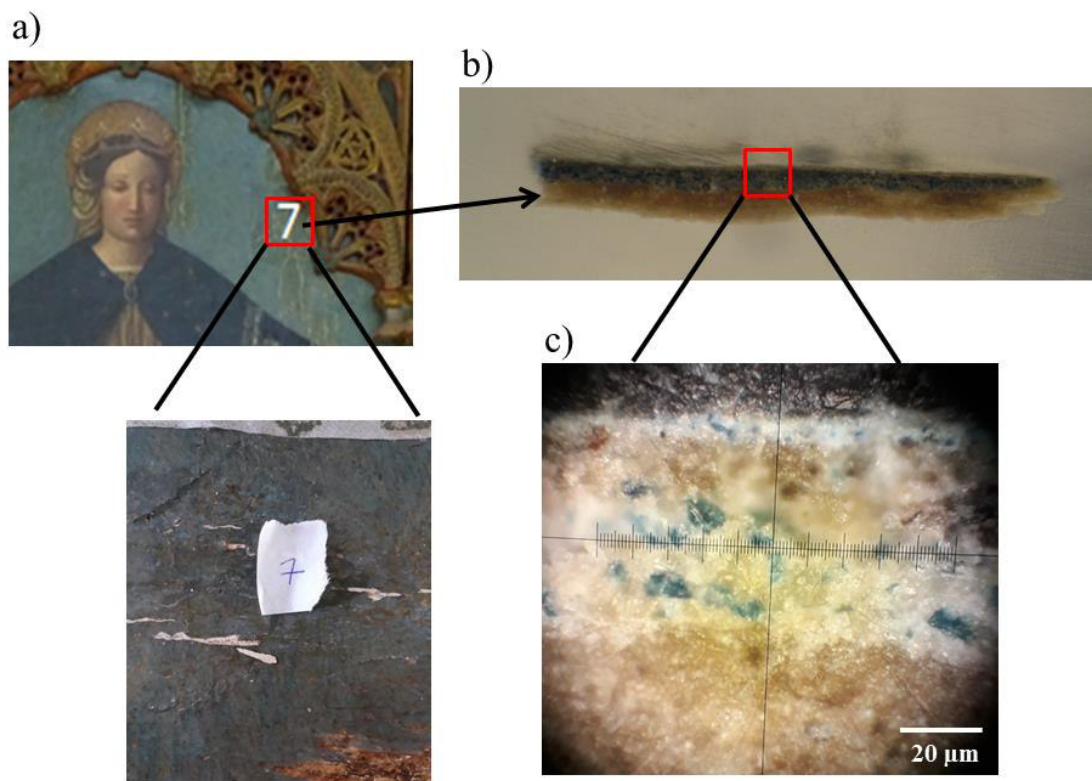


Figure 2.11 a) The sampling area of CS7 is marked on the picture and is zoomed in the picture below; b) CS7 analyzed at the stereomicroscope, a transversal sample (1-2 mm) embedded in a resin block showing all the layers by which the painting is composed; c) magnification of the cross section (objective of the microscope 50X) showing from the bottom to the top the original ground and paint layer and a more recent coat composed by a new ground and paint layer.

First of all, the cross section was examined through scanning electron microscopy (SEM). The image in Figure 2.12 confirms the presence of four layers: the 1st ground (around 150 µm), characterized by light elements; the 1st paint layer (≈ 70 µm) composed by grains of quite light elements in a heavier matrix; the 2nd ground layer (≈ 50 µm) and the 2nd paint layer (≈ 15 µm), both made of light matrices with some concentrated point of heavy elements. The energy dispersive

(EDS) analysis gave important indications about the elemental composition of the layers: Ca and S in the 1st ground layer, agree with the presence of gypsum (CaSO_4); Cu in the grains and Pb in the matrix of the 1st paint layer, hints of the presence of a blue copper pigment such as azurite [$\text{Cu}_3(\text{CO})_2(\text{OH})_2$] and a white lead pigment, probably lead white [$(\text{PbCO}_3)_2 \cdot \text{Pb}(\text{OH})_2$]; mainly Ca and S in the 2nd ground layer, again indicating the presence of gypsum; Ti and Cr in the 2nd paint layer, suggesting the use of titanium white (TiO_2) as white pigment and a chromium based bluish pigment. Certainly, the presence of Ti, introduced as pigment since 1920 [29], and Cr, employed from the second half of 19th century [30], is a piece of evidence which indicates the modernity of this layer, probably added during the last restoration.

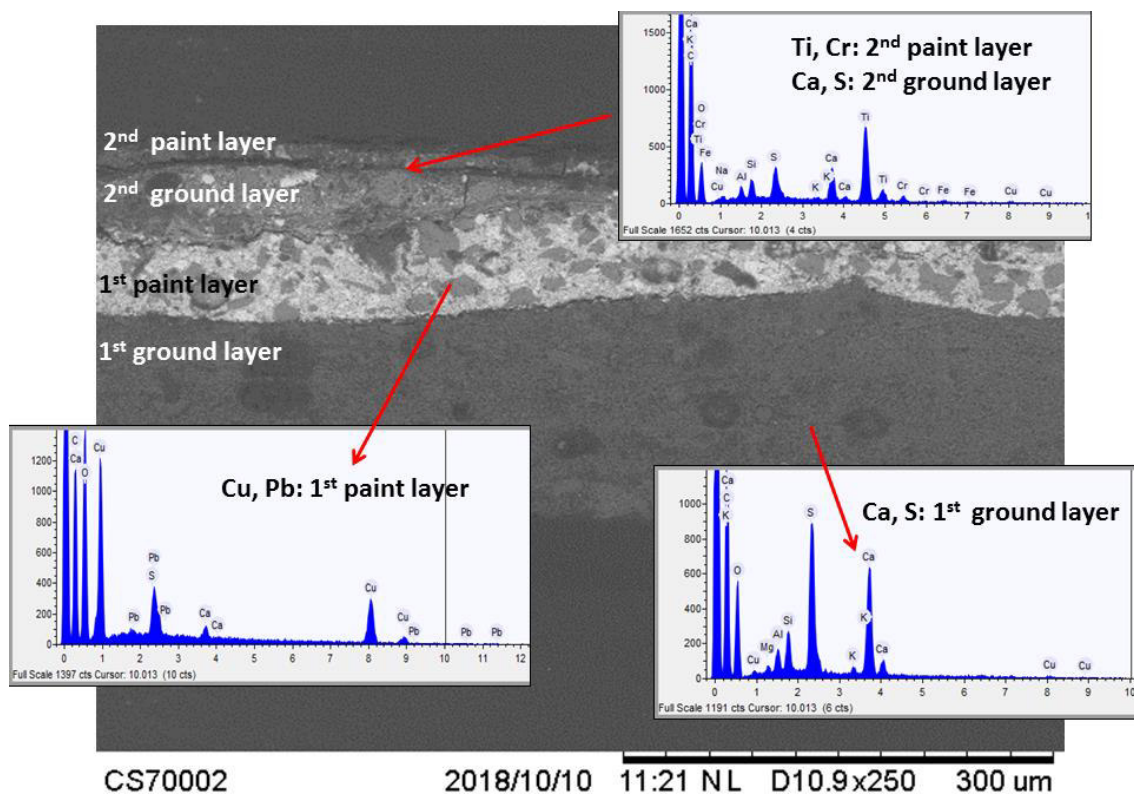


Figure 2.12 SEM image of CS7 and EDS analysis of each layer. The 1st and the 2nd ground layers are characterized by the presence of Ca and S; the 1st paint layer is composed by Cu and Pb while in the 2nd paint layer Ti and Cr are found.

In order to confirm the suppositions made on the basis of the elemental analysis, molecular spectroscopy and, in particular, Raman spectroscopy was applied. Figure 2.13 shows the Raman spectra of the analytes and the precise points of collection on the magnified cross section (Figure 2.13-a). The two ground layers were confirmed to contain gypsum, whose spectrum presents the typical band at 1009 (strong) cm^{-1} (Figure 2.13-b) [31]. Comparison with literature spectra [31] proved that the 1st paint layer is made of azurite, characterized by the bands at 1578 (weak), 1423 (medium), 1096 (m), 832 (w), 770 (m), 401 (s), 247 (m) and 83 (m) cm^{-1} (Figure 2.12-c), and lead white, whose bands are at 1055 (s) and 401 (m) cm^{-1} (Figure 2.13-d).

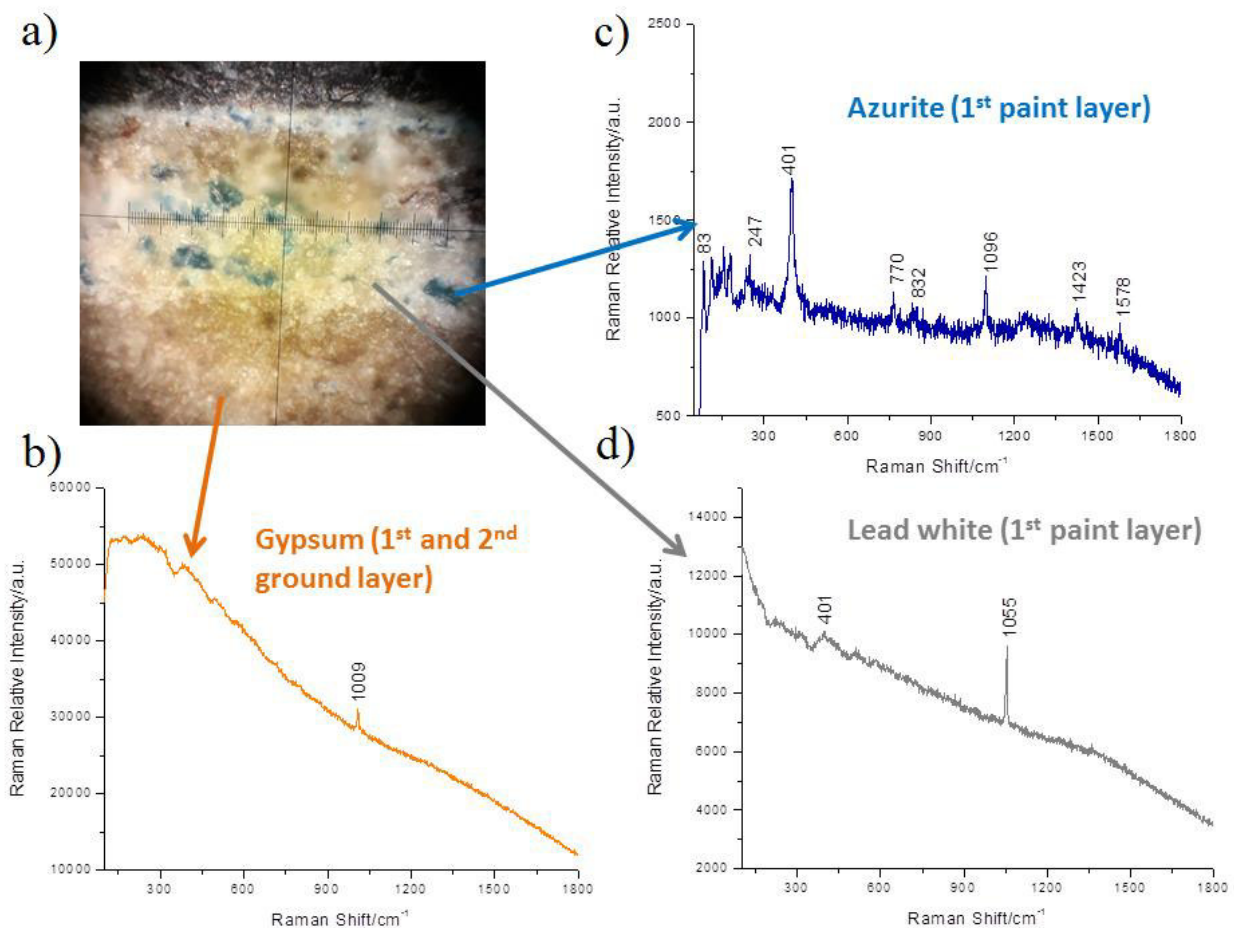


Figure 2.13 a) Picture of CS7 at the optical microscope (50X); Raman analysis carried out on CS7: the 1st and 2nd ground layers are composed by b) gypsum while the 1st paint layer is made of a mixture of c) azurite and d) lead white ($\lambda_{\text{ex}}=785\text{ nm}$, $P=0.05\text{ mW}$, $t=1 \times 10\text{ s}$).

The analyses performed on the 2nd paint layer are exposed below. The presence of titanium white was proved by the presence of its typical bands at 640 (m), 510 (m), 397 (m) and 143 (s) cm⁻¹ (Figure 2.14).

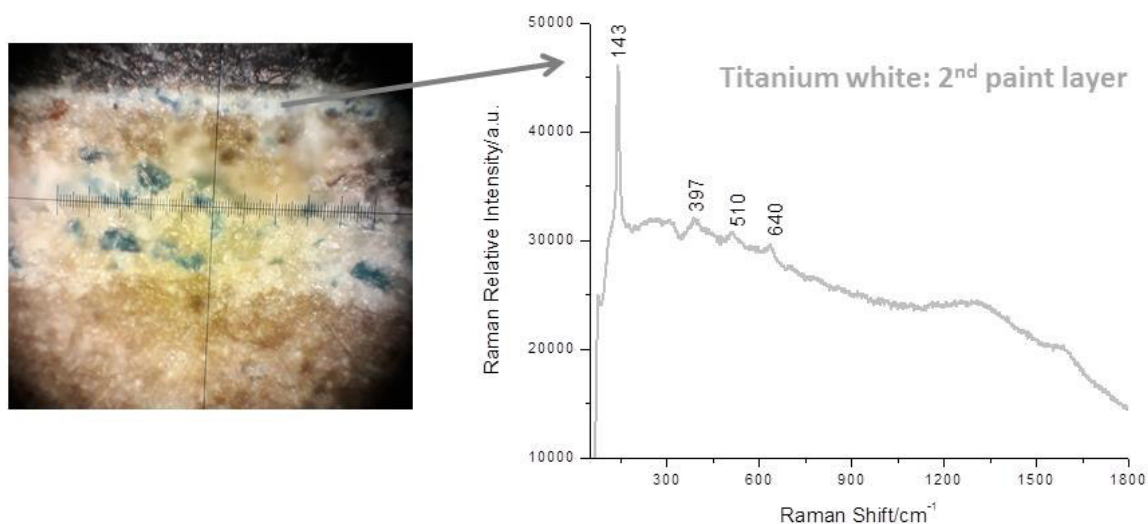


Figure 2.14 Raman analysis performed on the 2nd paint layer of CS7: the white pigment resulted titanium dioxide ($\lambda_{ex} = 785 \text{ nm}$, $P = 0.05 \text{ mW}$, $t = 1 \times 10 \text{ s}$).

The Raman characterization of the bluish pigment, due to the scarcity of grains and the tiny thickness of the layer, resulted particularly difficult. Figure 2.15-a shows an EDS spectrum collected on a blue grain of the 2nd paint layer which reveals the presence of S, Ba, Cr and Co. S and Ba indicate the presence of barite, BaSO₄. This natural occurring mineral has been synthetically produced from the beginning of the nineteenth century and, from that time on, it has been extensively employed both as filler in the formulations of colors [32] and used in the preparation of TiO₂ [29]. Cr and Co can be attributed to a bluish chromium-based pigment: cobalt chromite, CoCr₂O₄, identified by the Raman bands at 548 (s) and 162 (s) cm⁻¹ (the bands in gray belongs to titanium white) (Figure 3.15-b) [33]. PB36 (Cobalt Chromite Blue-Green Spinel) often substitutes the historically genuine Cerulean Blue (PB35, Cobalt Stannate), the latter being introduced in 1860 as

pigment [34], since it represents a cheaper alternative. The synthesis of PB36 dates back to the end of the eighteenth century when the basic process of calcining cobalt oxide and alumina, in which parts of the cobalt are substituted with chromium, was discovered [35].

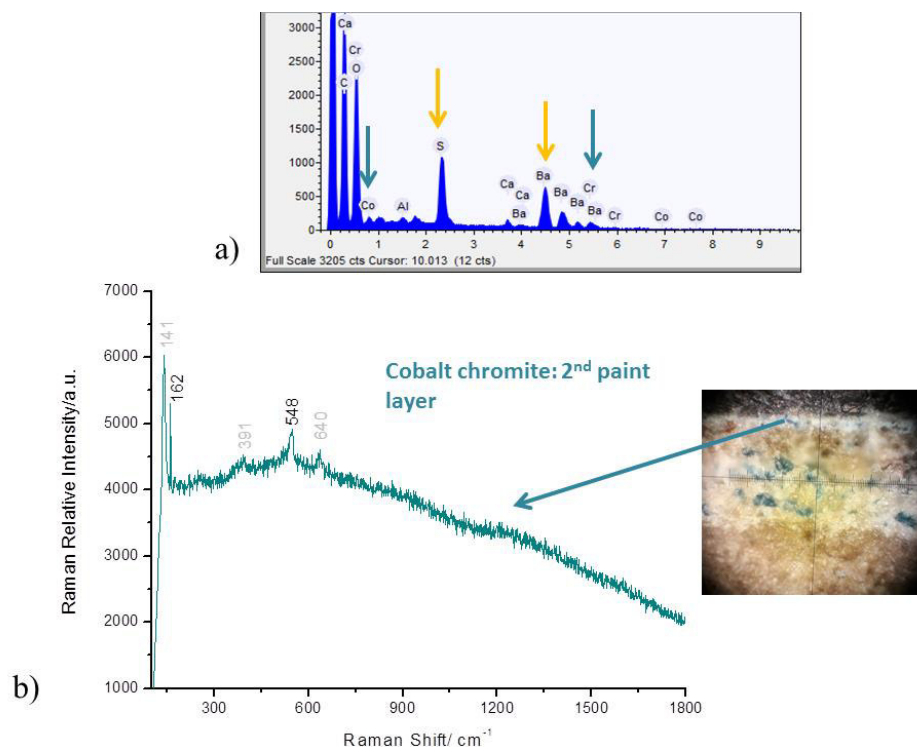


Figure 2.15 a) EDS spectrum performed on blue grain of the 2nd paint layer which reveals the presence of S, Ba, Cr and Co the 2nd paint layer of CS7; b) Raman spectrum of the chromium-based bluish pigment which resulted cobalt chromite ($\lambda_{ex} = 785$ nm, $P = 0.05$ mW, $t = 1 \times 10$ s).

While analyzing this blue layer we noticed that some spots gave strong fluorescence while others didn't. Indeed the spectrum in figure 2.15-b refers to the non-fluorescent grains. Comparing the obtained results with the composition of most diffused contemporary color tubes, it was clear that the presence of cobalt chromite alone was unlikely since this pigment often mixed with synthetic organic dyes [36]. Normal Raman spectroscopy didn't provide spectra useful for this diagnostic issue because of the fluorescence, typically generated by organic dyes (Figure 2.16-a). For this reason, we opted to employ the SERS technique using AgNSs as signal enhancers and fluorescence

quenchers, in order to amplify the Raman spectrum of the fluorescent grains. After adding Ag nanostars [21], the spectrum shown in Figure 2.16-b was collected. It is characterized by main bands at 1566 (m), 1510 (s), 1400 (w), 1379 (m), 1349 (s), 1303 (m), 1104 (s), 1002 (m), 720 (m), 679 (s), 649 (m), and 585 (w) cm^{-1} which roughly correspond to copper phthalocyanine, PB 15:2 [37]. The presence of this organic dye is confirmed by the detection of Cu signals in the EDS spectrum (Figure 2.16-c). Phtalocyanines were synthesized at the beginning of the twentieth century and they have been widely employed as blue and green pigment until today [38]. It can be noted that the band at 211 cm^{-1} is produced by the interaction of Ag with ions present in the colloidal solution of nanoparticles [39].

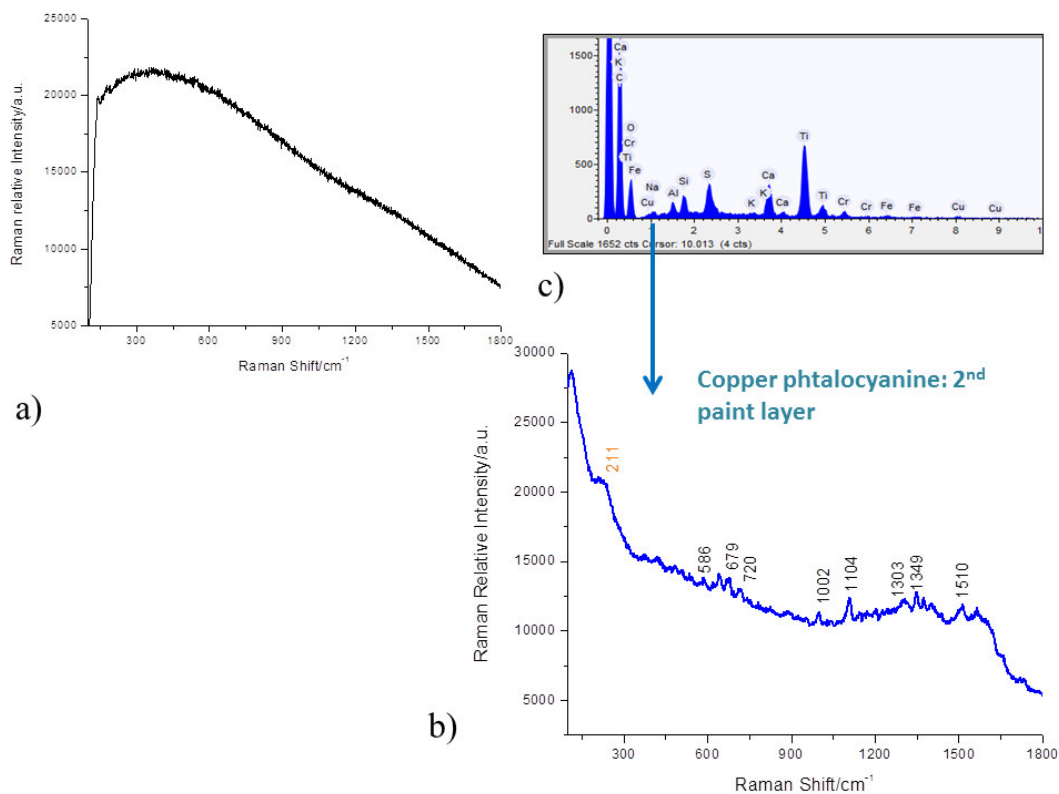




Figure 2.16 a) Raman spectrum of the blue organic dye in 2nd paint layer of CS7 which resulted completely fluorescent; b) SERS spectrum of the blue dye, obtained by adding concentrated AgNSs, which corresponds to a copper phthalocyanine; c) the presence of Cu is confirmed by EDS analysis ($\lambda_{\text{ex}} = 785 \text{ nm}$, $P = 0.05 \text{ mW}$, $t = 1 \times 10 \text{ s}$).


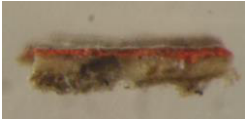




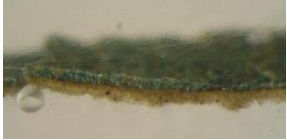
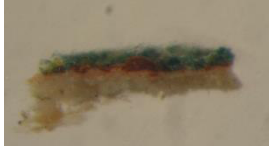
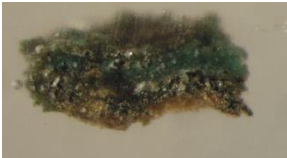
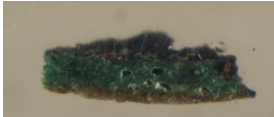
2.4.4 Conclusions

The analysis of CS7 from the *Madonna della Misericordia* revealed at least two moments of execution: the first one characterized by a paint layer made of azurite and lead white and the second one by a paint layer of titanium white, cobalt chromite, copper phtalocyanine and barite. On account of that, it is possible to state that the bluish repainting of the background of the panel and the *predella* (data not shown) and the decorations of the frame (analyses not shown) date back to the 20th century. However, since the materials composing the first paint layer, azurite and lead white, also present in Virgin Mary's mantle (data not shown) are employed throughout the history of art, we can't answer with full confidence whether its first manufacture dates back to the 19th or 15th century. Nevertheless, an accurate observation of the artistic style and the simplicity of the stratigraphy lead to the conclusion that it is highly improbable to date the first version of this painting to the 15th century. Probably, the painting that we are considering is a 19th century copy of an ancient original, lost in the centuries.

In order to make the description of the obtained results more clear, a brief summary of the detected materials in each cross section is presented in Table 2.2.

Table 2.2 Summary of the material composing the cross sections sampled from the *Madonna della Misericordia*.

Sample	Composition
CS1- upper left part of the bluish background 	Preparation: gypsum 1 st paint layer: azurite and lead white 2 nd paint layer: titanium white
CS2- bluish background in the <i>predella</i> 	Preparation: gypsum Paint layer: titanium white, phtalocyanine blue (?) and chromite (?)
CS3- Virgin Mary's blue mantle	Preparation: gypsum Paint layer: azurite, goethite (probably hydrated hematite) and lead white

	
<p>CS4- Santa Lucia's red tunic in the <i>predella</i></p> 	<p>Preparation: gypsum Paint layer: vermillion</p>
<p>CS5- client's red sleeve</p> 	<p>Preparation: gypsum Paint layer: vermillion</p>
<p>CS6- client's white bonnet</p> 	<p>Preparation: gypsum Paint layer: lead white</p>
<p>CS7- left lower part of the bluish background</p> 	<p>1st preparation: gypsum 1st paint layer: azurite and lead white 2nd preparation: gypsum 2nd paint layer: titanium white, phtalocyanine blue (?) and chromite (?)</p>
<p>CS1 frame- beige decoration</p> 	<p>Preparation: gypsum Paint layer: lead white</p>
<p>CS2 frame- greenish decoration</p> 	<p>Preparation: gypsum Paint layer: titanium white and supposed phtalocyanine + chromite</p>
<p>CS3 frame- green decoration</p> 	<p>Preparation: gypsum 1st red paint layer: red lead 2nd green paint layer: supposed phtalocyanine + chromite</p>
<p>CS4 frame- bluish decoration</p> 	<p>Paint layer: supposed Scheele's green</p>
<p>CS6 frame- bluish decoration</p> 	<p>Paint layer: supposed Scheele's green</p>

The description of this case study underlines the importance of the so called analytical sequence [40] in the examination of cultural heritage: non-invasive techniques (see Appendix B) give the necessary indications to continue with the micro-destructive ones, justifying the sampling; the analysis of the stratigraphy is fundamental to understand the story of the work of art; the suppositions made on the basis of the elemental techniques are confirmed by the molecular ones and, above all for the objective of this thesis, when the Raman spectroscopy fails the SERS technique comes to the aid.

References

- [1] A. Guerrero-Martínez, S. Barbosa, I. Pastoriza-Santos, L.M. Liz-Marzan, *Curr. Opin. Colloid Interface Sci.* **2011**, *16*, 118.
- [2] Y. Wang, P.H.C. Camargo, S.E. Skrabalak, H. Gu, Y. Xia, *Langmuir* 2008, *24*, 12042.
- [3] A. García-Leis, J.V. García-Ramos, S. Sánchez-Cortés, *J. Phys. Chem. C* **2013**, *117*, 7791.
- [4] P.S. Kumar, I. Pastoriza-Santos, B. Rodriguez-Gonzales, F.J. García de Abajo, L.M. Luis-Marzan, *Nanotechnology* **2007**, *19*, 015606.
- [5] L. Litti, J. Reguera, F.J. García de Abajo, M. Meneghetti, L.M. Liz-Marzan, *Nanoscale Horiz.* **2019**.
- [6] L. Rodríguez-Lorenzo, R.A. Alvarez-Puebla, I. Pastoriza-Santos, S. Mazzucco, O. Stéphan, M. Kociak, L.M. Liz-Marzán, F.J. García de Abajo, *J. Am. Chem. Soc.* **2009**, *131*, 4616.
- [7] I. Pastoriza-Santos, L.M. Luis-Marzán, *Adv. Funct. Mater* **2009**, *19*, 679.
- [8] H. Yuan, C.G. Khoury, H. Hwang, C.M. Wilson, G.A. Grant, T. Vo-Dinh, *Nanotechnology* **2012**, *23*(7), 075102.
- [9] M. Yamamoto, Y. Kashiwagi, T. Sakata, H. Mori, M. Nakamoto, *Chem. Mater* **2005**, *17*, 5391.
- [10] O.M. Bakr, B. H. Wunsch, F. Stellacci, *Chem. Mater* **2006**, *18*, 3297.

- [11] M. Zhou, S. Chen, S. Zhao, *Chem. Lett.* **2006**, 35, 332.
- [12] Z. Li, W. Li, P.H.C. Camargo, Y. Xia, *Angew. Chem. Int. Ed.* **2008**, 47, 9653.
- [13] L. Lu, A. Kobayashi, K. Tawa, Y. Ozaki, *Chem. Mater* **2006**, 18, 4894.
- [14] Y. Wang, P.H.C. Camargo, S.E. Skrabalak, H. Gu, Y. Xia, *Langmuir* **2008**, 25, 12042.
- [15] P.C. Lee, D. Meisel, *J. Phys. Chem.* **1982**, 86, 3391.
- [16] M.V. Cañamares, J.V. García-Ramos, J.D. Gomez-Varga , C. Domingo, S. Sánchez-Cortés, *Langmuir* **2005**, 21, 8546.
- [17] A.D. McFarland, M.A. Young, J.A. Dieringer, R.P. Van Duyne, *J. Phys. Chem. B* **2005**, 109, 11279.
- [18] N. Valley, N. Greeneltch, R.P. Van Duyne, G.C. Schatz, *J. Phys. Chem. Lett.* **2013**, 4, 2599.
- [19] J.B. Shein, L.M.H. Lai, P.K. Eggers, M.N. Paddon-Row, J.J. Gooding, *Langmuir* **2009**, 25, 11121.
- [20] M. Silvestrini, P. Ugo, *Anal. Bioanal. Chem.* **2013**, 405, 995.
- [21] M. Zamuner, D. Talaga, F. Deiss, V. Guieu, A. Kuhn, P. Ugo, N. Sojic. *Adv. Funct. Mater.* **2009**, 19 (44), 3129.
- [22] T.J. Cho, V.A. Hackley, *Anal. Bioanal. Chem.* **2010**, 398, 2003.
- [23] J. Fontana, J. Livenerec, F. J. Bezaresd, J. D. Caldwell, R. Rendell, B. R. Ratna. *Appl. Phys. Lett.*, **2013**, 102, 20160.
- [24] Q. Ma, H. Zhang, W. Liua, J. Gea, J. Wua, S. Wang, P. Wang, *RSC Adv.* **2016**, 6, 85285.
- [25] S. Sánchez-Cortés, J.V. García-Ramos, *J. Raman Spectrosc.* **1998**, 29, 365.
- [26] Stanislao da Campagnola, *L'arte nella chiesa e nel convento di s. Maria Maddalena e dell'Immacolata (già s. Caterina), in I Cappuccini a Parma: quattro secoli di vita, a cura di Felice da Mareto* **1961**, Ist. grafico tiberino, Roma.

- [27] C. Ricci, *La R. Galleria di Parma* **1896**, L. Battei, Parma.
- [28] L. Fornari-Schianchi, Galleria Nazionale di Parma, *Catalogo delle opere dall'antico al Cinquecento* **1997**, F.M. Ricci, Milano.
- [29] M. Laver, *Titanium dioxide whites* in “*Artists' Pigments. A Handbook of their History and Characteristics*” Vol 3 **1997**, E.W. ed. Fitzhugh, Oxford University Press, Cambridge.
- [30] R. Newman, *Chromium oxide greens* in “*Artists' Pigments. A Handbook of their History and Characteristics*” Vol 3 **1997**, E.W. ed. Fitzhugh, Oxford University Press, Cambridge.
- [31] L. Burgio, R.J.H. Clark, *Spectrochim. Acta Part A* **2001**, 57,1491.
- [32] R.L. Feller, *Barium Sulphate - Natural and Synthetic in Artists' Pigments. A Handbook of their History and Characteristics Vol 1* **1986**, 255-283, ed. R.L. Feller, Cambridge University Press, Cambridge.
- [33] M.C. Caggiani, A. Cosentino, A. Mangone, *Microchem. J.* **2016**, 129, 123.
- [34] D. Bomford, J. Kirby, J. Leighton, A. Roy, R. White, L. Williams, *Art in the making: impressionism* **1990**, ISBN: 0300050356, National Gallery, London, United Kingdom.
- [35] A.A. Travor (ed.), *Coatings technology handbook – Third edition* **2005**, CRC Press.
- [36] www.maimeri.it, consulted in November 2019.
- [37] N.C. Scherrer, S. Zumbuehl, F. Delavy, A. Fritsch, R. Kuehnen, *Spectrochim. Acta Part A* **2009**, 73, 505.
- [38] M.A. Dahlen, *Ind. Eng. Chem.* **1939**, 31(7), 839.
- [39] M.V. Cañamares, J.V. García-Ramos, C. Domingo, S. Sánchez-Cortés, *Vib. Spectrosc.* **2006**, 40, 161.
- [40] D. Pinna, M. Galeotti, R. Mazzeo, *Scientific examination for the investigation of paintings. A handbook for restorers* **2011**, Centro Di, Firenze.

Chapter 3

Hierarchical nanostructures based on Ag nanostars @ Au nanowires for the SERS detection of lake-pigments

3.1 Introduction

The excellent properties of AgNSs [1] used for the sensitive SERS [2,3] detection of benzenethiol [4] (see Chapter 2) make them the optimal nanoparticles for the preparation of complex nanostructures [5-8] eventually suitable for further enhancing Raman signals. It was indeed demonstrated that bimetallic structures promote the plasmonic effect [9]. Moreover, the contemporary presence of two metals can bring several other advantages; for instance, Ag and Au have been employed to prepare hierarchical structures which can exploit both the strong SERS effect typical of AgNSs and the suitability of Au for immobilizing biological samples [10] (see also paragraph 1.5 of this thesis).

As substrates to be decorated with Ag nanoparticles we have chosen high aspect ratio Au nanowires (AuNWs). AuNWs can be obtained in the shape of ensembles of nanowire electrodes via templated electroless deposition in nanoporous membranes [11,12]. The strategy used here to prepare the hierarchical structures is based on the use of cysteamine bridges [13,14], this molecule binding the AuNWs and the AgNSs via the thiol and amine functional groups, respectively. The obtained hierarchical structure is named hereafter AgNSs@AuNWs. As a comparison, nanostructures composed by spherical AgNPs [15,16] at AuNWs (AgNPs@AuNWs) were prepared as well. It is worth to note that both kind of nanostructures can be eventually further functionalized in order to

immobilize on their surface biomolecules suitable to develop SERS-based biosensors [17,18]. After optimization of the procedures and characterization of the obtained nanomaterials (FE-SEM and TEM analyses were performed with the experimental assistance of Prof. Patrizia Canton, University Ca' Foscari of Venice), the SERS properties were assessed at first with respect to adsorbed benzenethiol, used as SERS active probe, whose spectrum is well known from the literature [19]. The experimental data, carried out with the assistance of Dr. Lucio Litti and Prof. Moreno Meneghetti at the University of Padua, were supported and compared with digital simulations and calculations of the electromagnetic field enhancement at the interfaces by employing the boundary element method (BEM), implemented by the aforementioned researchers [20,21]. After these preliminary studies, Raman enhancement properties of the nanomaterials and, in particular, of the hierarchical structure AgNSs@AuNWs were tested referring to the detection of a colouring agent quite challenging to be analyzed in painting media, that is cochineal lake (CL), also known as carmine or crimson lake. Lake-pigments are complex coloring agents in which an organic dye (see paragraph 1.6.1) is adsorbed onto particles of insoluble inorganic salt. Thanks to the colouring properties of carminic acid [22], cochineal has long been used as colorant, both alone for dyeing textiles or adsorbed on insoluble particles to produce the pictorial lake pigment [23,24]. Since the lake pigments are complex materials, their analysis is complex as well, being usually performed after extraction (and preconcentration) of the organic dye from the raw pigment. Indeed, Ag colloids have been previously used to detect by SERS anthraquinone-based red dyes in solution [25], in grains embedded in various binding media with [26] or without [27] previous extraction or hydrolysis. Similar methodologies have been applied also for analyzing dyes in pre-treated fibres [28] or on textile samples [29] as well as on cross sections sampled from works of art [30,31]. In the present study, we study the possibility to apply AgNSs@AuNWs substrates for the SERS detection of CL, without performing the extraction of the carminic acid dye.

3.2 Materials and methods

3.2.1 Materials

All the chemicals used in the preparation of the AgNSs were purchased from Sigma-Aldrich. Silver nitrate (AgNO_3); sodium citrate tribasic dihydrate ($\text{C}_6\text{O}_7\text{H}_5\text{Na}_3 \cdot 2\text{H}_2\text{O}$); sodium hydroxide (NaOH); hydroxylamine in solution (NH_2OH ; 50% w/v in water). Polycarbonate filter membranes, coated by the producer with the wetting agent polyvinylpyrrolidone, were supplied by SPI-Pore Filter (47 mm filter diameter, filter thickness 6 μm , 80 nm pore size, 6×10^8 pores/ cm^2 pore density). Flat macro-gold slides are prepared by vapor deposition of a 10 nm chromium adhesion layer followed by 200 nm of gold onto standard glass microscope slides. For the electroless gold deposition the following chemicals were employed: methanol (CH_3OH , Sigma-Aldrich); tin chloride (SnCl_2 , Sigma-Aldrich), silver nitrate (AgNO_3 , Sigma-Aldrich); ammonium hydroxide (NH_4OH , Sigma-Aldrich); sodiumdisulfitoaurate(I) ($\text{Na}_3\text{Au}(\text{SO}_3)_2$, BOC Sciences); sodium sulfite (Na_2SO_3 , Sigma-Aldrich); nitric acid (HNO_3 , Sigma-Aldrich). Cochineal lake-pigment (0116E) was purchased from Zecchi (Firenze, Italy), made of carminic acid (7- α -D-glucopiranosyl-3,5,6,8-tetrahydroxy-1-methyl-9,10-dioxoanthracene-2-carboxylic acid; M. W. = 492.38 g/mol) bound onto alum.

3.2.2 Synthesis of AgNSs and AgNPs

AgNSs were synthesized according to the protocol described by A. García-Leis *et al.* [1], while AgNPs were prepared adapting the method described by P.C. Lee and D. Meisel [15,16] (see Chapter 2).

3.2.3 Membrane templated preparation of AuNWs

Ensembles of gold nanowires embedded in the polycarbonate (PC) template (2DNEEs) were prepared by the electroless membrane templated procedure described previously [11,32] and

summarized in Figure 3.1. Briefly, after dipping the PC membrane in methanol for 4 h, it was sensitized with Sn^{2+} in a solution containing 0.026 mol L^{-1} SnCl_2 and 0.07 mol L^{-1} trifluoroacetic acid in 50:50 methanol: water for 45 min. After rinsing with methanol, the membrane was dipped in 0.026 mol L^{-1} $\text{Ag}[(\text{NH}_3)_2]\text{NO}_3$ for 10 min. The membrane was washed with methanol and then with water and successively immersed in an Au plating bath containing $7.9 \cdot 10^{-3} \text{ mol L}^{-1}$ $\text{Na}_3\text{Au}(\text{SO}_3)_2$ in 0.127 mol L^{-1} Na_2SO_4 at $0 \text{ }^\circ\text{C}$. After 20 min, 0.625 mol L^{-1} formaldehyde was added to the solution. Electroless deposition was allowed to proceed for 24 hours. After this period the golden membrane was washed with water and immersed in 10% HNO_3 solution for 12 hours and finally rinsed with water and dried. At the end of the electroless deposition, gold is deposited both within the pores and the outer faces of the membrane. Therefore, to expose the polycarbonate, the outer gold layer was removed from one face of the membrane by peeling with scotch tape (Scotch® Magic™ by 3M), while keep the nanowires intact within the pores. The membrane was then rinsed again with water and dried. In order to remove the polycarbonate of the templating membrane to expose the AuNWs, two different etching processes were applied, one to perform the partial [32] and the other for the total etching [33,34]. For the former case (partial etching) the AuNWs, 2DNEEs were dipped for 30 s in $\text{CH}_2\text{Cl}_2:\text{EtOH}$ 1:9 [33]. The total etching of the polycarbonate, was instead achieved by attaching a 2DNEE onto a Teflon support by means of Kapton adhesive tape and pouring pure dichloromethane several times on the tilted sample. Exposed AuNWs were cleaned by residues of PC by using a procedure recently described [34], based on the use of a cold atmospheric plasma jet system, namely, Stylus Plasma Noble produced by NADIR SrL (Italy). For the present application, the following parameters were employed: Ar/O_2 flux= 8 L/min; t = 60 s; HV= 4 W - Gain 40%; RF= 15 W pulsed; WD= 8 mm.

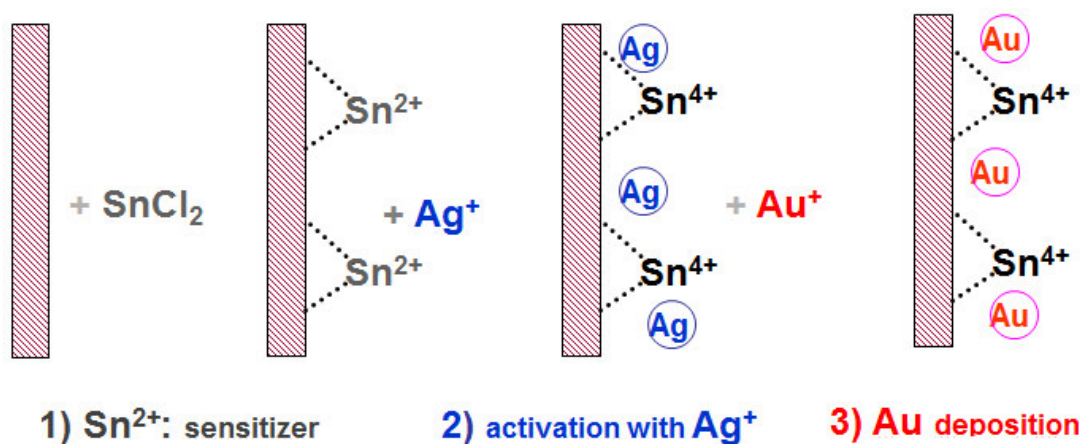


Figure 3.1 Schemes summarizing the steps used to produce AuNWs via electroless reduction of gold in track etched polycarbonate membrane: 1) Sn²⁺ sensitizes the membrane; 2) the membrane is dipped into a Ag[(NH₃)₂]NO₃ solution and Sn²⁺ reduces Ag⁺ to metallic silver; 3) the membrane is immersed in a Na₃Au(SO₃)₂ solution. Formaldehyde, gradually added, reduces slowly Au⁺ to metallic gold. The nuclei of Ag⁰ on the membrane are galvanically displaced by Au⁰. In this way the pores are filled and the outer faces get covered by gold.

3.2.4 Preparation of the samples for the Raman analysis

The macro-gold slides and the AuNWs arrays employed for the benzenethiol (BT) detection were prepared as follows:

4. overnight immersion in 10 mM cysteamine water solution [14];
5. overnight immersion in the colloidal suspension of nanoparticles (AgNPs or AgNSs);
6. overnight immersion in 10⁻² mM BT ethanolic solution [4].

The substrates used to investigate cochineal lake-pigment, macro-gold and AuNWs, were prepared following this protocol:

1. overnight immersion in 10 mM cysteamine water solution [14];

2. deposition of 1 μL drop of concentrated AgNSs onto the samples, letting the solvent to evaporate at room conditions;
3. overnight immersion in few mLs of a methanolic dispersion of cochineal lake-pigment at the desired concentration, typically 0.492 mg/mL.

The colloidal suspension of AgNSs was concentrated by centrifuging three times at 8000 rpm in a 1.5 mL Eppendorf centrifuge tube from 500 μL of colloid. After each centrifugation step 400 μL of supernatant were removed and replaced by the same quantity of colloid. Before centrifuging, nanoparticles which got stuck at the bottom were dispersed again in order to eliminate the interfering salts.

3.2.5 Instrumentation

SERS and Raman spectroscopy

The Raman spectra were measured on macro-gold and AuNWs with or without Ag nanospheres and AgNSs, using either one of the following instrumental setups: i) Renishaw inVia Raman spectrometer equipped with a diode laser operating at 785 nm (300 mW max power), used at 0.1% of its power (0.3 mW), with an acquisition time of 10 s, coupled with an optical microscope (Leica), with objective 20X/0.4; ii) Micro Raman B&W Tek model i-Raman 785S equipped with a diode laser operating at 785 nm (300 mW max power), power 5 % (15 mW), acquisition time 3 x 20 s, coupled with an optical microscope (Olympus BX51), with objective 20X/0.4. No significant differences were observed in the results obtained using one or the other setup. The post-processing of the spectra was performed with the OriginLab software. Because of the heterogeneity of the examined samples, preliminary measurements were performed analyzing different areas of the samples, targeting the spots providing the highest signals. The spectra reported and compared in this work are indeed the spectra providing the highest signals for each of the examined substrates. The

evidence that relative SERS enhancements are comparable when this procedure was applied both on different batches of samples and using different instrumentation, confirms the validity of this experimental approach that provides comparable results, independently on the instrumentation used.

UV-Visible absorption spectroscopy

UV-Vis absorbance spectra were recorded with a Perkin-Elmer Lambda 40 spectrophotometer equipped with a Peltier-Elmer PTP6 (Peltier temperature programmer) apparatus. The analysis of AuNWs suspensions were performed in dichloromethane.

Transmission electron microscopy (TEM)

Transmission electron microscopy (TEM) and high resolution TEM (HRTEM) images were measured using a JEOL 3010 high resolution electron microscope (0.17 nm point-to-point resolution at Scherzer defocus), operating at 300 kV, equipped with a Gatan slow-scan CCD camera (model 794) and an Oxford Instrument EDS microanalysis detector Model 6636. Drops of colloidal solutions were deposited on Holey-Carbon Copper grids and let dry at room temperature before analysis.

Field-emission scanning electron microscopy (FE-SEM)

The SEM analysis were performed using a Sigma-VP Carl Zeiss field-emission scanning electron microscope. Solid samples were immobilized on stubs by means of conductive tape in order to prevent the charging of the surfaces.

Boundary element method (BEM) simulations

The digital structures used to simulate the nanomaterials in this study were produced by a 3D design modeling software (Blender 2.79b) and then imported in Matlab environment. The minimum distance between AgNS and AuNW was fixed at 0.5 nm, as it is reported to be the minimum distance avoiding complex coupling effects [36]. The attribution of the physical properties for the nanostructures and the environments, as well the spectra and local fields simulations, were done

using the MNPBEM libraries developed by U. Hohenester *et al.* [19,20]. The exciting fields (with excitation source at 785 nm) are considered as propagating along the x, y and z axes and polarized along the two other normal directions for each case. The results are an average of the different field excitations, simulating the situation of a nanostructure at a random orientation with respect of the incoming field. The Raman enhancement factors are calculated as the forth power of the local fields calculated at the surface of the simulated structures, given unitary the intensity of the exciting electromagnetic field. This can be done because the frequency of the exciting light and that of the scattered light are similar, being the difference that of a vibrational frequency.

3.3 Results and Discussion

3.3.1 Characterization of the AuNWs by UV-Vis spectroscopy and FE-SEM

The FE-SEM images in Figure 3.2 show the morphology of the ensembles of AuNWS at different steps of their preparation. Namely, Figure 3.2-A shows the surface of a 2DNEE after peeling of the outer gold layer, with the nanowires inlaid within the membrane pores. Figure 3.2-B shows that a short time treatment (30 s) in $\text{CH}_2\text{Cl}_2/\text{C}_2\text{H}_5\text{OH}$ exposes only the top of the nanowires, for a length of approximately 250-300 nm. Finally, Figure 4.2-C and D confirm that abundant washing with CH_2Cl_2 removes efficiently all the polycarbonate of the template with complete exposition of the AuNWs. These nanowires result approximately 6 μm long which corresponds to the thickness of the templating membrane. The AuNWs are not perfectly cylindrical, instead, they tend to assume a cigar-like shape, with a maximum diameter around 120-150 nm, since they adapt to the cigar shape of the track-etched pores in polycarbonate membrane [12,37], The high enlargement FE-SEM image in Figure 4.2-D, also confirms what discussed in our previous studies [38], i.e. that the templated electroless deposition of gold in track-etched membranes starts with the formation of

small Au nuclei deposited on the inner wall of each nanopore, these nuclei successively growing under the shape of a nanowire formed by nanospheres efficiently stacked together.

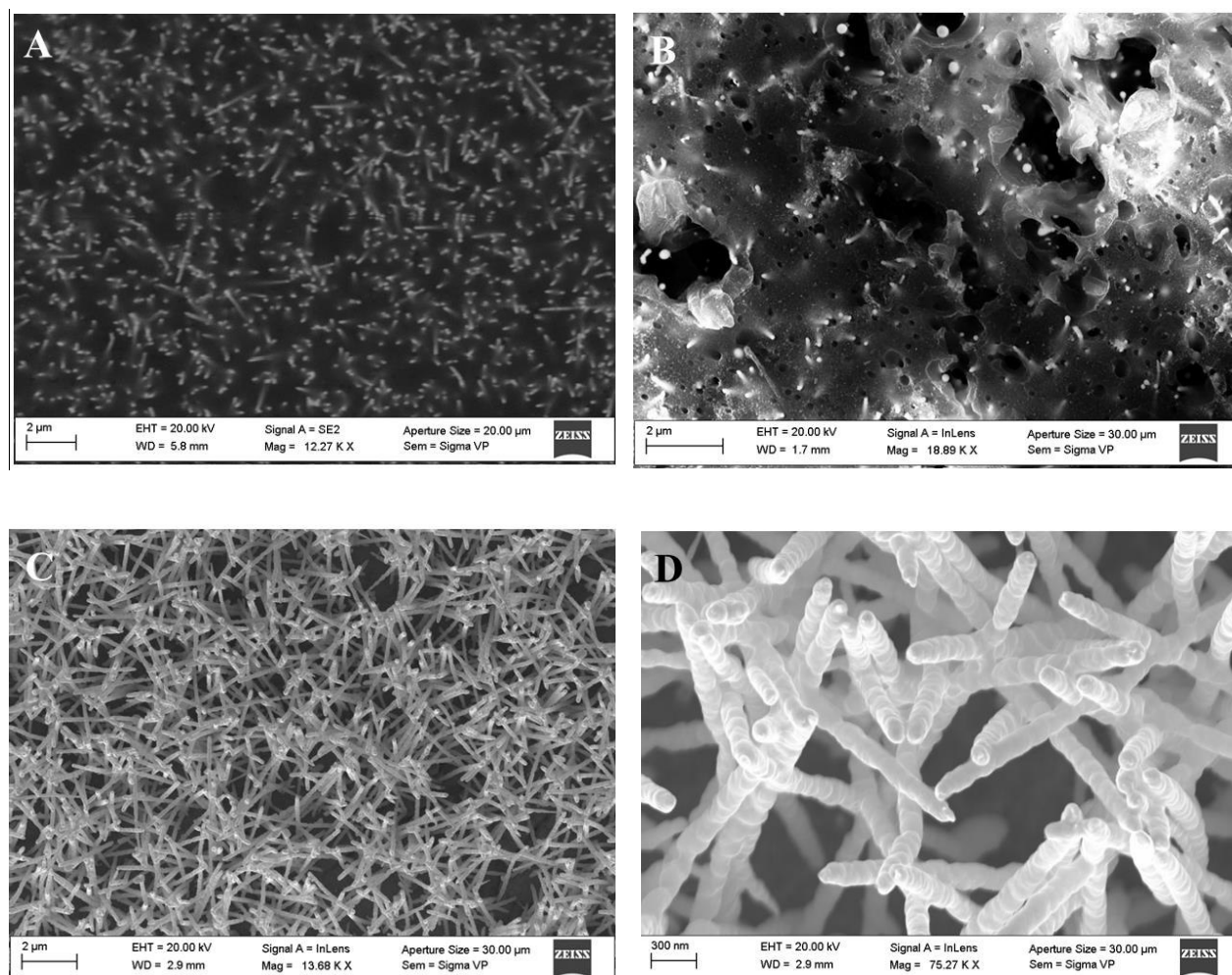


Figure 3.2 FE-SEM images of polycarbonate membranes: A) after gold electroless deposition and peeling the gold from the outer face of the membrane B) after chemical etching with 1:9 $\text{CH}_2\text{Cl}_2/\text{C}_2\text{H}_5\text{OH}$ for 30 s and plasma etching and C-D) after total etching in dichloromethane.

The typical UV-Vis absorption spectrum of AuNWs, suspended in dichloromethane after careful removal of the polycarbonate, showed the maximum absorption at 532 nm, in agreement with previous findings (see Figure 3.3) [38].

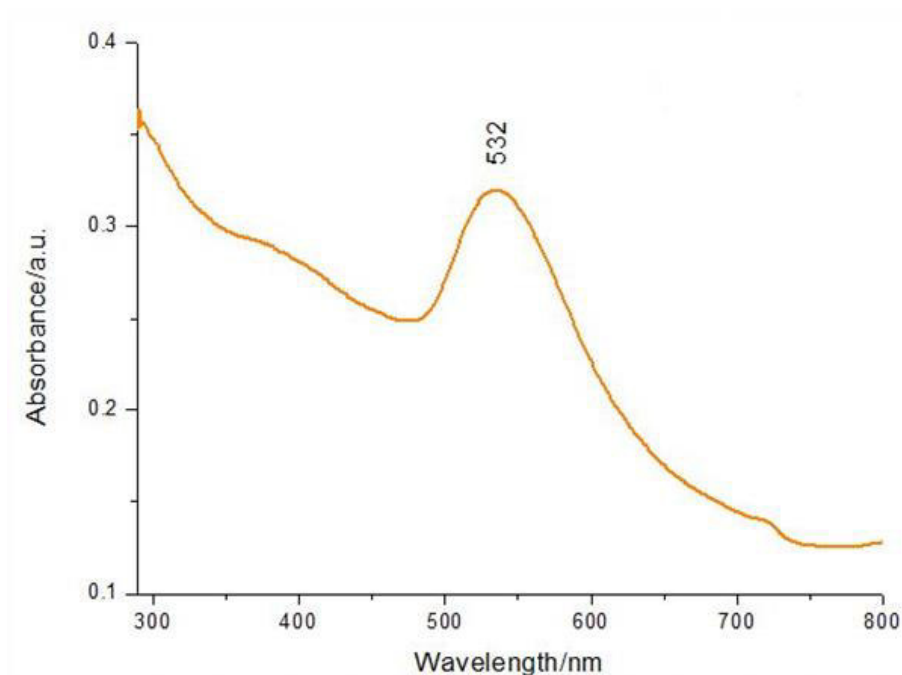


Figure 3.3 UV-Vis absorption spectrum of AuNWs, showing the maximum absorption at 532 nm⁻¹.

3.3.2 Preparation and FE-SEM characterization of AgNPs@AuNWs hierarchical structures

Cysteamine was used as bridging ligand suitable to bind the silver nanoparticles onto the gold nanowires [13,14]. Indeed, the sulfhydryl group of the thiol has a great affinity for gold while the amine group binds silver. Note that an excess of cysteamine was used in order to prevent the possibility that both the sulfhydryl and the amine groups of the same molecules could bind only the AuNW surface; operating with excess cysteamine, on the surface of the AuNWs a compact cysteamine monolayer is expected to be formed, with the amine functionalities protruding out of the Au surface [13]. Figure 3.4 reports the FE-SEM analyses performed after treating the ensemble of AuNWs with cysteamine and AgNSs as described in the experimental section. These images show that the AgNSs are bound onto the surface of the AuNWs, in part as isolated entities and in part as clusters of nanostars. The latter areas are the spots on which the laser beam used for SERS measurements (see below) was preferentially focused since preliminary tests indicate that focusing the laser beam on these areas produces higher SERS signals.

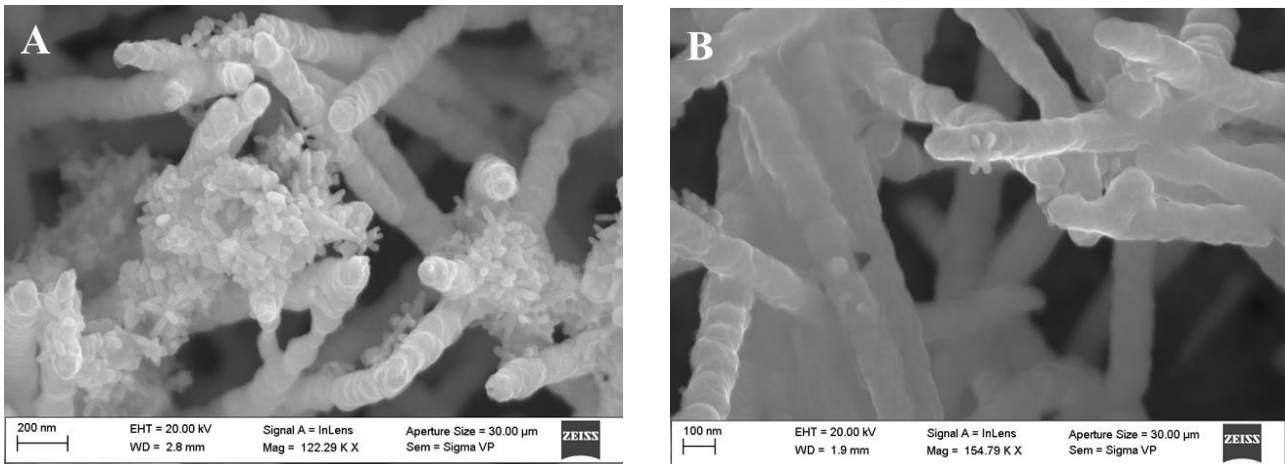


Figure 3.4 A-B) FE-SEM image of total etched AuNWs bound to AgNSs by means of cysteamine.

3.3.3 Boundary element method simulations

The complex morphology of the hierarchical nanostructure above described makes it difficult to perform the quantitative evaluation of the exposed surface area so preventing the precise calculation of the surface concentration of the Raman probe, necessary for the evaluation of REFs from experimental spectra (see equation 1.1). To overcome this limit, we chose to model and compare the localized intensity of electromagnetic fields in the nanostructures by numerical calculations performed using the boundary element method (BEM). The BEM approach assumes a dielectric environment where bodies with homogeneous and isotropic dielectric functions are separated by abrupt interfaces. It can be employed in the field of plasmonics, in which metallic nanoparticles are embedded in a dielectric background. It presents the advantage that only the boundaries between the different dielectric materials have to be discretized and not the entire volume, performing faster simulations with low memory requirements [19,20]

Figure 3.5 shows the REFs obtained by BEM for an AgNS, an AuNW and the coupling of the two nanostructures are reported, using an excitation source at 785 nm. The EFs are calculated as the forth power of the local fields calculated at the surface of the simulated structures, given unitary the

intensity of the exciting electromagnetic field. The enhancements calculated in the AgNSs hot spots are of the order of 10^4 , but only in very tiny areas, whereas the one obtained for AuNW is order of magnitude smaller (10^2). This shows that the expected enhancements for isolated AgNS and AuNW are small. Calculations for the assembled AgNS and AuNW show, on the other hand, that the enhancements are at least of the order of 10^5 , but in extended areas. The absence of sharp tips, or edges, in both AgNS and AuNW avoid the local fields to concentrate in single nanostructures alone. One can conclude, therefore, that the hierarchical system composed by these two nanomaterials optimizes the enhancement by creating hot spots on large areas due to the proximity of the two.

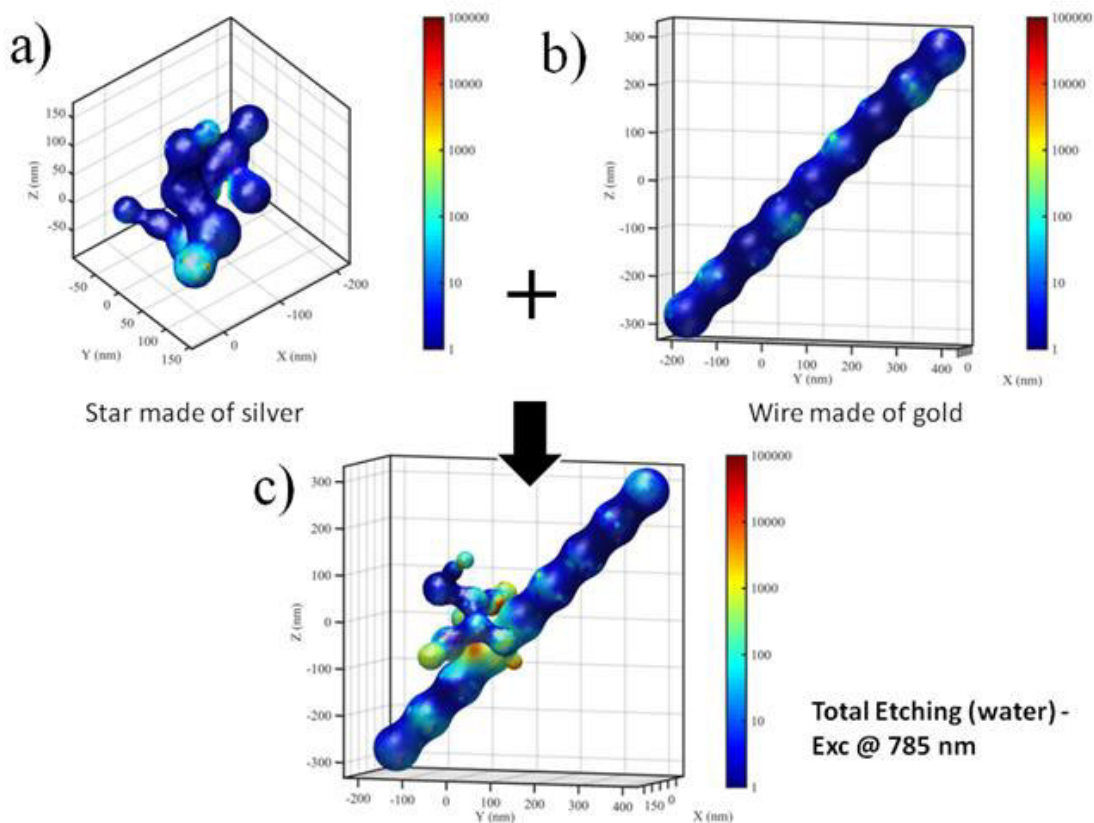


Figure 3.5 BEM calculations of the SERS enhancements, exciting at 785 nm, produced by a) AgNS (enhancement factor $\sim 10^4$ in very limited areas), b) AuNW (enhancement factor $\sim 10^2$) and c) the hierarchical system composed by these two nanomaterials (EF $\sim 10^5$ in wider areas).

The BEM methodology has been applied also to spherical AgNPs bound to AuNW in the hierarchical structure AgNPs@AuNWs and relevant results are summarized graphically in Figure

3.6. Comparison between Figure 3.5 and 3.6 indicates a significantly larger number of hot spots for AgNSs@AuNWs.

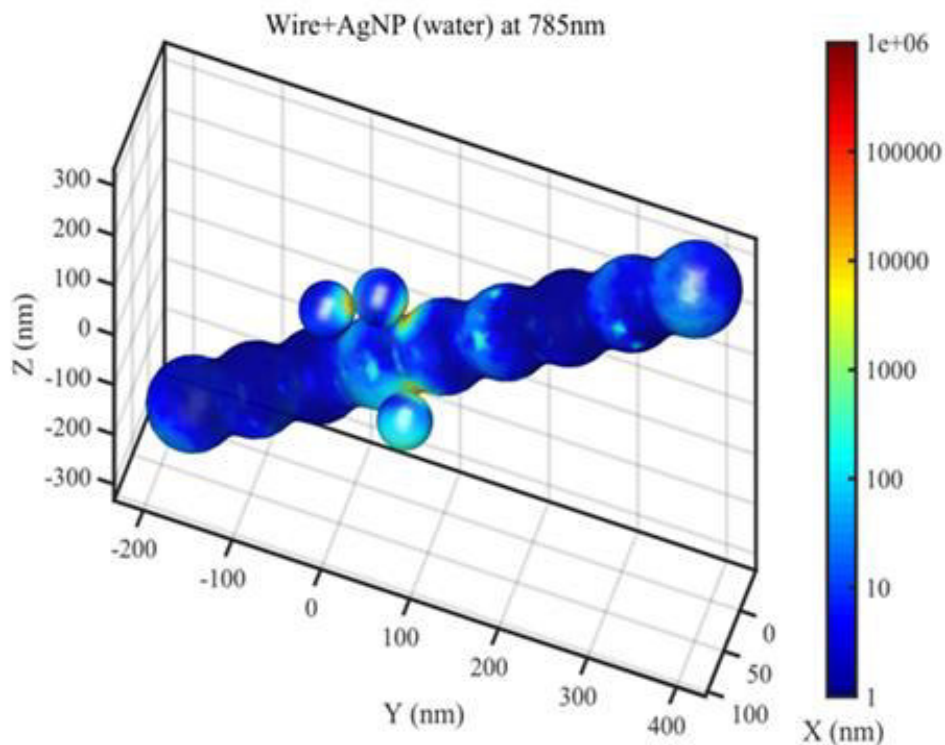


Figure 3.6 BEM calculations of the SERS enhancements, exciting at 785 nm, produced by Ag nanospheres coupled to AuNW.

3.3.4 SERS characterization with benzenethiol as Raman probe

The efficiency of several SERS substrates was assessed by employing benzenethiol (BT) as reference Raman-probe [39,40] whose Raman bands are well known from the literature [21]. Figure 3.7 presents the spectra obtained on ensembles of AuNWs, partially (Figure 3.7-a) or totally etched without (Figure 3.7-b) or with AgNPs (Figure 3.7-c) or AgNSs (Figure 3.7-d). On the partially etched AuNWs, BT cannot be detected while, on totally etched AuNWs the typical Raman spectrum of this probe is observed. This indicates that AuNWs, fully free from the polycarbonate,

can act as SERS substrate. Almost the same signals of AuNWs alone are found using the AgNPs@AuNWs assemblies, but a dramatic enhancement in SERS activity is obtained using AgNSs@AuNWs hierarchical nanostructures. Note that the band at 243 cm^{-1} (in purple) is attributed to the interaction between colloidal Ag and ions adsorbed from the preparation solution [41]. All these evidences indicate the superior SERS performances of AgNSs when coupled with macro-gold [42] with even more dramatic effects when assembled on AuNWs. The obtained results are in agreement with the expectations drawn from the BEM calculations which highlighted a larger number of hot spots and stronger SERS enhancement for AgNSs@AuNWs structures .

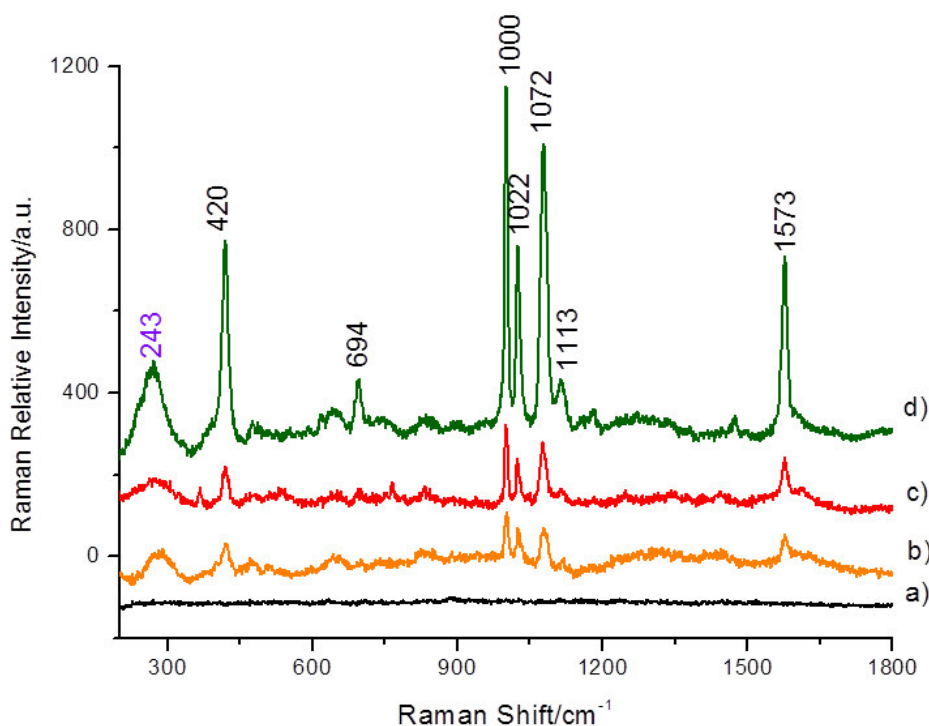


Figure 3.7 Raman spectra of of benzenethiol adsorbed from a 10^{-2} mM solution onto: a) partially etched AuNWs; b) totally etched AuNWs; c) totally etched AuNWs + AgNPs; d) totally etched AuNWs + AgNSs. The main bands of BT are marked in black and those attributed to the colloid in purple ($\lambda_{\text{ex}}= 785$ nm, $P = 0.3$ mW, $t = 1 \times 10$ s).

3.3.5 Application to cochineal lake-pigment detection

The positive results obtained with BT prompted us to test the application of AgNSs@AuNWs as SERS substrate for improving the Raman detection of cochineal lake-pigment (CL), chosen among the artistic dyes as model analyte pigment of complex nature and particularly challenging to detect. The main Raman bands obtained with the AgNSs@AuNWs, marked in Figure 3.8, are compared with the main bands of carminic acid reported in literature [41] and summarized in Table 3.1.

Table 3.1 Main Raman bands of carminic acid compared to those of cochineal lake experimentally recorded using AgNSs@AuNWs and their assignments [41].

Reference bands	Experimental bands	Assignments
454	462 m	Skeletal vibrations
554	559 w	
685	662 w	$\gamma(\text{CCC})/\gamma_{\text{Glu}}(\text{CH})/\gamma_{\text{Glu}}(\text{COH})$
731	728 m	$\rho(\text{CH}_3)/\gamma(\text{CH})/\gamma(\text{COH})/\tau(\text{CCCC})$
963 w	945 w	$\delta_{\text{Glu}}(\text{COH})/\rho(\text{CH}_3)/\delta(\text{CCC})$
1229 w	1217 m	$\delta(\text{C}_5\text{OH})/\delta(\text{C}_4\text{H})/\nu(\text{CC})/\delta_{\text{Glu}}(\text{CH})$
1308 s	1297 s	$\delta(\text{C}_5\text{OH})/\delta(\text{C}_8\text{OH})/\delta(\text{C}_3\text{OH})/\nu(\text{CC})$
1449 m	1441 w	$\nu_{\text{I/II}}(\text{CC})/\delta(\text{CH}_3)/\delta_{\text{Glu}}(\text{CH})$
1553 s	1534 m	$\nu_{\text{III}}(\text{CC})/\delta(\text{C}_8\text{OH})/\delta(\text{CH})$

Figure 3.8 compares the SERS spectra recorded after adsorbing CL on four different substrates, namely: a) undecorated macro-gold, b) undecorated AuNWs, c) AgNSs on macro-gold, d) AgNSs@AuNWs. No useful Raman signal was detected with macro-gold (Figure 3.8-a) nor with AuNWs alone (Figure 3.8-b), so confirming that the Raman detection of cochineal lake-pigment is not a trivial issue. Instead the presence of AgNSs deposited onto macro-gold led to significantly better results (Figure 3.8-c) in that the main bands of the carminic acid in the CL are recognized at: 1534 (m), 1441 (w), 1297 (s), 1217 (m), 945 (w), 728 (m), 662 (w), 559 (w) and 462 (m) cm^{-1} . We wish to point out that in these spectra, the signal at 1024 cm^{-1} is attributed to the presence of citrate

ions left on the silver nanostars surface [43], the peak at 285 cm^{-1} is attributed to the AuNWs themselves (Figure 3.8-b) and the one at 216 cm^{-1} is related to the colloidal Ag (Figure 3.8-c-d) [41]. All evidence indicates that for CL, the strongest Raman enhancement and the best definition of the bands is again obtained using the hierarchical structure AgNSs@AuNWs (Figure 3.8-d).

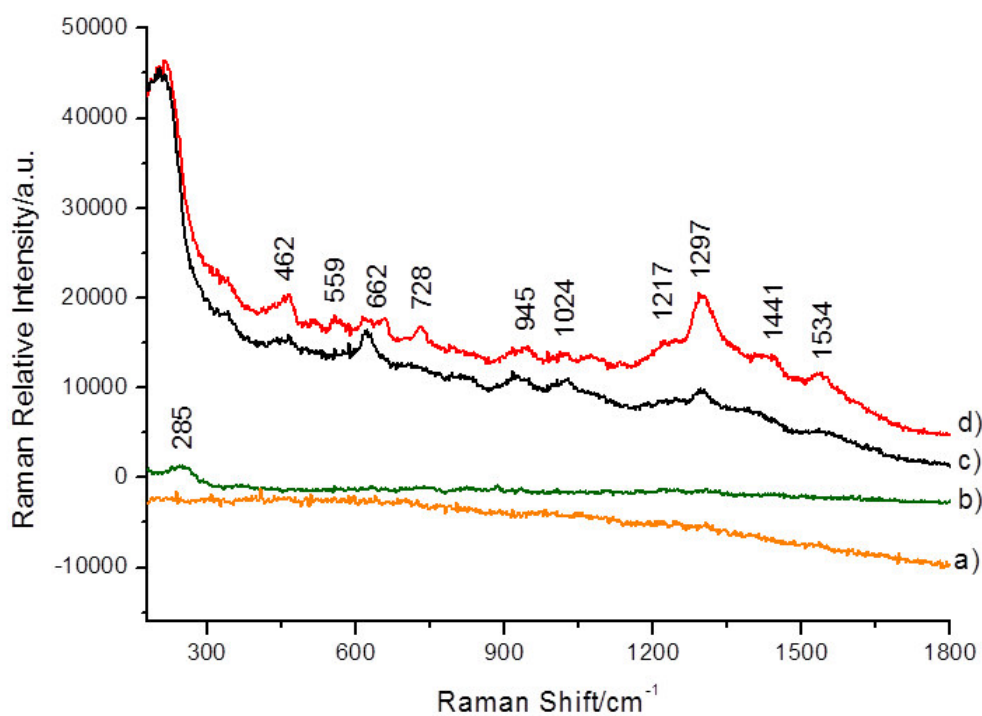


Figure 3.8 SERS spectra of a 0.492 mg/mL cochineal lake-pigment dispersion recorded on: a) macro-gold; b) totally etched AuNWs; c) AgNSs@macro-gold; d) AgNSs@AuNWs ($\lambda_{\text{ex}} = 785\text{ nm}$, $P = 15\text{ mW}$, $t = 3 \times 20\text{ s}$).

It is worth to point out that the resolution and intensity of the Raman signals for CL do not reach the enhancement level observed for BT, however these results show that it is possible to reliably detect CL directly by SERS using the AgNSs@AuNWs. Note that, in these experiments, the dye, namely carminic acid (CA), is not extracted from the lake-pigment and the analyses are performed directly using a dispersion of this lake-pigment where the dye is mixed with alum in approximately 1:2

molar ratio (Al:CA) [44]. In order to provide an estimate of the analytical performances relevant to SERS determination with the aid of AgNSs@AuNWs structures, a preliminary calibration plot was obtained. In these experiments CL dispersions containing 0.024, 0.036 and 0.049 mg/mL of the lake-pigment were incubated on AgNSs@AuNWs and relevant SERS spectra recorded. Figure 3.9 reports the linear graph obtained by plotting the Raman intensities recorded at approximately 1300 cm^{-1} vs. CL concentration in the dispersion from which the adsorption of the lake-pigment on AgNSs@AuNWs was performed. The background noise (σ_b) was evaluated from the standard deviation in five repeated blank measurements at 1300 cm^{-1} and resulted 3000 a.u. From the sensitivity $m = 8 \cdot 10^5 \text{ a.u./mg} \cdot \text{mL}^{-1}$, the limit of detection (LOD) was calculated using the equation $\text{LOD} = 3\sigma_b/m$ and resulted 0.01 mg/mL. Typically the content of carminic acid in CL is around 18-43% [45]. From UV-Vis spectra of the CL methanol solution used here, we estimated that the CA content in our CL is approximately 40%. Therefore, the detection limit of 0.01 mg/mL corresponds approximately to a molar concentration of CA of $8 \cdot 10^{-6} \text{ M}$.

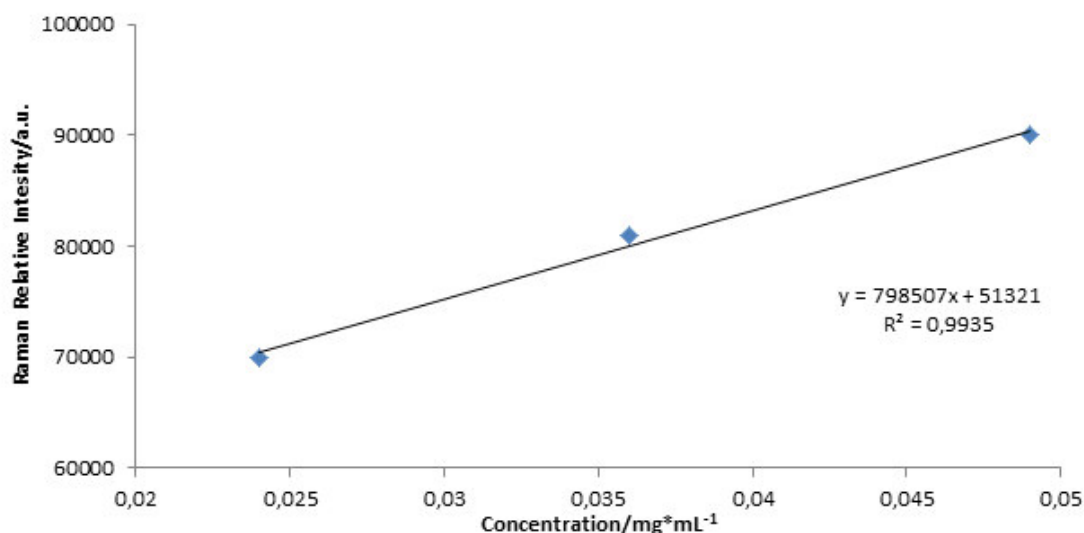


Figure 3.9 Calibration plot obtained by plotting the Raman intensities recorded at 1300 cm^{-1} vs. CL concentration. In these experiments cochineal lake dispersions (0.024, 0.036 and 0.049 mg/mL) were incubated on AgNSs@AuNWs and relevant SERS spectra recorded.

4.4 Conclusions

In this work three different kinds of nanomaterials were synthesized and characterized with focus on their SERS, namely, AuNWs, AgNPs and AgNSs. It was proven that the highest enhancement was produced by AgNSs@AuNWs, both for BT and CL. Indeed, AgNSs alone showed to be SERS active substrates, however, as expected on the BEM simulation, the effect is amplified when coupling AgNSs with AuNWs. BEM simulations indicated that the AgNSs@AuNWs hierarchical structures present a higher number of hot spots with respect to AgNSs, AuNWs and AgNPs@AuNWs structures, which agrees with our experimental findings. From an applicative viewpoint, the results obtained show that the AgNSs@AuNWs can be used as efficient SERS substrates for the analysis of lake-pigments such as the cochineal lake, without requiring the extraction of the organic dye contained in the lake. Preliminary tests showed that this methodology can be applied also to analyze other lake-pigments, such as the rose madder lake-pigment [46]. It is worth to note that this kind of nanostructures is suitable for further functionalization in order to eventually develop novel SERS biomolecular sensors [17], even in the context of an innovative combination of SERS with a microfluidic approach [47] or thin layer chromatography (TLC) [18].

References

- [1] A. García-Leis, J.V. García-Ramos, S. Sánchez-Cortés, *J. Phys. Chem. C* **2013**, *117*, 7791.
- [2] M. Fleischmann, P.J. Hendra, A.J. McQuillan, *Chem. Phys. Lett.* **1974**, *26(2)*, 163.
- [3] R.F. Aroca, M. C. Vallete, J.V. García Ramos, S. Sánchez-Cortés, J.A. Sánchez Gil, P. Sevilla, *Amplificación plasmónica de espectros Raman y de fluorescencia SERS y SEF sobre nanoestructuras metálicas* **2014**, Ed. CSIC, Madrid, Spain.
- [4] M. Zamuner, D. Talaga, F. Deiss, V. Guieu, A. Kuhn, P. Ugo, N. Sojic, *Adv. Funct. Mater.* **2009**, *19(44)*, 3129.

- [5] S. Park, J. Lee, H. Ko, *ACS Appl. Mater. Interfaces* **2017**, *17*, 44088.
- [6] Y. Zhao, X. Li, Y. Liu, L. Zhang, F. Wang, Y. Lu, *Sens. Actuators B* **2017**, *247*, 850.
- [7] W. J. Anderson, K. Nowinska, T. Hutter, S. Mahajan, M. Fischlenchner, *Nanoscale*, **2018**, *10*, 7138.
- [8] W. Xin, J.-M. Yang, M. S. Goorsky, L. Carlson, I. M. De Rosa, *ACS Appl. Mater. Interfaces*, **2017**, *9*, 6246.
- [9] K. Kim, J.K. Yoon, *J. Phys. Chem. B* **2005**, *109*, 20731.
- [10] X. Guo, Z. Guo, Y. Jin, Z. Liu, W. Zhang, D. Huang, *Microchim. Acta* **2012**, *178*, 229.
- [11] V.P. Menon, C.R. Martin, *Anal. Chem.* **1982**, *63*, 1920.
- [12] P. Ugo, L.M. Moretto, *Template Deposition of Metals*, Ed. C. Zosky, *Handbook of Electrochemistry*, chapter 16.2, Elsevier, 678-709, Amsterdam, NL **2007**
- [13] J.B. Shein, L.M.H. Lai, P.K. Eggers, M.N. Paddon-Row, J.J. Gooding, *Langmuir* **2009**, *25*, 11121.
- [14] M. Silvestrini, P. Ugo, *Anal. Bioanal. Chem.* **2013**, *405*, 995.
- [15] P.C. Lee, D.J. Meisel, *J. Phys. Chem.* **1982**, *86*, 3391.
- [16] M.V. Cañamares, J.V. García-Ramos, C. Domingo, S. Sánchez-Cortés, *Vib. Spectrosc.* **2006**, *40*, 161.
- [17] N. Banaei, A. Foley, J.M. Houghton, Y. Sun, B. Kim, *Nanotechnology* 2017, *28*, 45510.
- [18] G. Sciutto, S. Prati, I. Bonacini, L. Litti, M. Meneghetti, R. Mazzeo, *Anal. Chim. Acta* **2017**, *991*, 104.
- [19] U. Hohenester, A. Trügler, *Comput. Phys. Commun.* **2012**, *183*, 370.
- [20] U. Hohenester, *Comput. Phys. Commun.* **2018**, *222*, 209.
- [21] J. Fontana, J. Livenerec, F. J. Bezaresd, J. D. Caldwell, R. Rendell, B. R. Ratna, *Appl. Phys. Lett.*, **2013**, *102*, 20160 .

- [22] P. Allevi, M. Anastasia, S. Bingham, P. Ciuffeda, A. Fiecchi, G. Cighetti, M. Muir, A. Scala, J. Tyman, *J. Chem. Soc., Perkin Trans. 1* **1998**, 575.
- [23] H. Schweppe, H. Roosen-Runge, *A Handbook of their History and Characteristics Vol 1*, ed. Feller R.L. Cambridge University Press, Cambridge, **1986**, 255.
- [24] M.V. Cañamares, M. Leona, *Lasers in the Conservation of Artworks* **2008**, Castillejo et al. (eds) © Taylor & Francis Group, London.
- [26] F. Pozzi, J. R. Lombardi, S. Bruni, M. Leona, *Anal. Chem.* **2012**, *84*, 3751.
- [27] C.L. Brosseau, F. Casadio, R.P. Van Duyne, *J. Raman Spectrosc.* **2011**, *42*, 1305.
- [28] M. Leona, J. Stenger, E. Ferloni, *J. Raman Spectrosc.*, **2006**, *37*, 981.
- [29] K. L. Wustholz, C. L. Brosseau, F. Casadio, R. P. Van Duyne, *Phys. Chem. Chem. Phys.*, **2009**, *11*, 7350.
- [30] A. Idone, M. Aceto, E. Diana, L. Appolonia, M. Gulminic, *J. Raman Spectrosc.*, **2014**, *45*, 1127.
- [31] K. A. Frano, H. E. Mayhew, S. A. Svoboda, K. L. Wustholz, *Analyst*, **2014**, *139*, 6450.
- [32] M. De Leo, A. Kuhn, P. Ugo, *Electroanalysis* **2007**, *19(2-3)*, 227.
- [33] S. Yu, N. Li, J. Wharton, C. R. Martin, *Nano Lett.* **2003**, *3(6)*, 815.
- [34] A.M. Stortini, S. Fabris, G. Saorin, E. Verga Falzacappa, L.M. Moretto , P. Ugo, *Nanomaterials* **2019**, *9(2)*, 150.
- [35] A. Patelli, E. Verga, L. Nodari, S.M. Petrillo, A. Delva, P. Ugo, P. Scopece, *Mater. Sci. Eng.* **2018**, *364*, 012079.
- [36] R. Esteban, A.G. Borisov, P. Nordlander, J. Aizpurua, *Nat. Commun.* **2012**, *3*, 825.
- [37] P. Apel. Track-etching technique in membrane technology. *Radiat. Meas.* **2001**, *34*, 559.
- [38] M. De Leo, F.C. Pereira, L.M. Moretto, P. Scopece, S. Polizzi, P. Ugo, *Chem. Mater.* **2007**, *19(24)*, 5955.
- [39] A.D. McFarland, M.A. Young, J.A. Dieringer, R.P. Van Duyne, *J. Phys. Chem. B* **2005**, *109*, 11279.

- [40] N. Valley, N. Greeneltch, R.P. Van Duyne, G.C. Schatz, *J. Phys. Chem. Lett.* **2013**, *4*, 2599.
- [41] M.V. Cañamares, J.V. García-Ramos, C. Domingo, S. Sánchez-Cortés, *Vib. Spectrosc.* 2006, *40*, 161.
- [42] L. Rodriguez-Lorenzo, R. Ivarez-Puebla, J. García de Abajo, L.M. Liz-Marzán, *J. Phys. Chem. C* **2010**, *114*, 7336.
- [43] S. Sánchez-Cortés, J.V. García-Ramos, *J. Raman Spectrosc.* **1998**, *29*, 365.
- [44] A.P. Damant, *Food colorants in Handbook of textile and industrial dyeing* **2011**, Woodhead Publishing.
- [45] P.N. Marshall, R.V. Horobin, *Stain Technol.* **1974**, *49(1)*, 19.
- [46] M. Longoni, *Nanomateriali avanzati per l'analisi SERS di coloranti usati in ambito artistico*, Master Thesis, University Ca' Foscari of Venice, academic year **2017-18**.
- [47] D. Calzavara, D. Ferraro, L. Litti, G. Cappelletto, G. Mistura, M. Meneghetti, M. Pierno, *Adv. Cond. Matter Phys.* **2018**, 9 pages.

Chapter 4

Hierarchical nanostructures based on Ag nanostars @ Cu nanowires

4.1 Introduction

The experimental part exposed in this Chapter was carried out in collaboration with Margherita Longoni, Dr. Angela Maria Stortini, concerning the deposition of Cu-nanowires and Dr. Lavinia de Ferri and Prof. Giulio Pojana, in relation to the SERS measurements (Università Ca' Foscari, Venice, Italy). The focus of this Chapter is the preparation of a novel hierarchical SERS substrate, composed by Cu nanowires decorated with AgNSs (AgNSs@CuNWs). The properties of AgNSs and the protocol used for their preparation have been already described in Chapter 3 [1]. Instead, the attention will be pointed to the optimization of the membrane template electrochemical synthesis of CuNWs [2] and, thereafter, and the testing of the possibility to use AgNSs@CuNWs as SERS substrates. The final aim is the comparison with the already described AgNSs@AuNWs hierarchical nanostructures, presented in Chapter 3, in order to verify if the presence of copper instead of gold represents an advantage or a disadvantage in terms of Raman enhancement. The SERS properties of Cu have been previously investigated and it results, similarly to gold, less efficient than silver because it absorbs the visible photons < 600 nm while Ag presents a high reflectivity all along the visible spectrum, helping in this way the plasmonic effect [3]. Indeed, Cu can be considered a valuable alternative to Au as metal to be coupled with AgNSs [3]. Cu has already been employed to prepare SERS nanoparticles [4] and even in hierarchical nanostructures used as powdered substrate for Ag nanoparticles, reaching a Raman enhancement in the order of $1.4 \cdot 10^5$ [5]. On account of that, nanoporous membranes were employed as template for the

electrochemical deposition of copper in shape of nanowires. The potential advantage of using Cu nanowires instead of Au nanowires could be the significantly lower cost of copper.

4.1.1 Electrochemical template deposition of quasi-monodimensional nanomaterials

As presented in Chapters 1 and 3, the hard template synthesis is a method based on the use of a nanoporous membrane template as a mold for the oriented growth of metal structures which trace the shape of its pores [6-8]. Nanoporous membranes of different materials are employed to this aim. Figure 4.1-A shows an alumina membrane which is prepared through controlled anodization of aluminum, characterized by dense and ordered pores, hexagonally organized [9]. Instead, Figure 4.1-B presents a polycarbonate membrane whose porosity is obtained by the track-etching technique, that is bombarding the polymeric film with high-energy particles or ions followed by development of the defects so generated by chemical etching in alkaline solution [10]. The polycarbonate membranes present sparse and irregular porosity, even though their flexibility often represents an advantage with respect to the fragility of the alumina ones. The metal deposition inside the pores can be electroless (see Chapter 3) or electrochemical, as in this case.

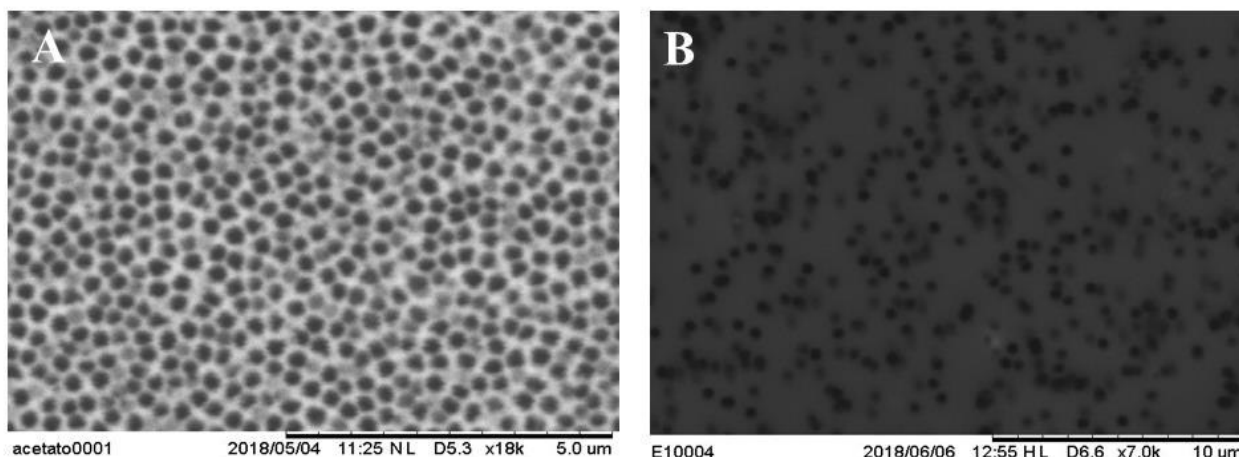


Figure 4.1 SEM images of an A) alumina and a B) polycarbonate nanoporous membrane.

The metal ions in solution are reduced electrochemically on a metal layer pre-deposited on, or in intimate contact with, one face of the membrane (which is electronically insulating). By this method, the metal is deposited at the pore/electrode interface and fills the pores from the bottom to

the top. The final result is an ensemble of solid wires whose matrix can be etched to expose them partially or completely (Figure 4.2) [11].

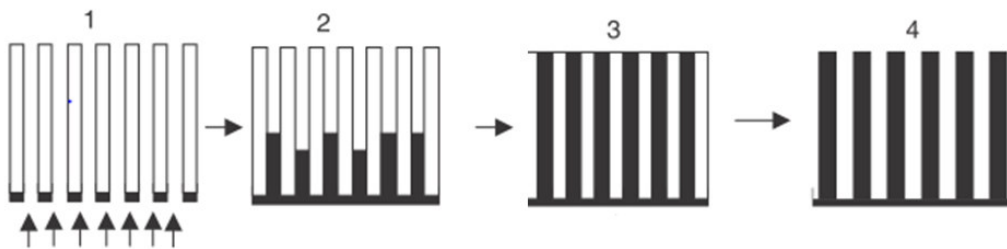


Figure 4.2 Electrodeposition steps of NWs: 1) the deposition starts from the side of the membrane in contact to the electrode; 2) growth of the NWs; 3) the NWs reach the top of the pores; 4) etching of the template. Adapted from [11].

This kind of deposition, can be performed potentiostatically, when a constant reducing potential is applied, or galvanostatically, when a constant current is used. Because of the better control of the process, in this thesis we used the potentiostatic method. In order to obtain arrays of nanowires, the metal deposition must be stopped a little earlier than when the pores are completely filled, otherwise the metal starts to pour out of the pores creating protuberances on the surface of the membrane and mushroom-like structures are formed (see Figure 4.3).

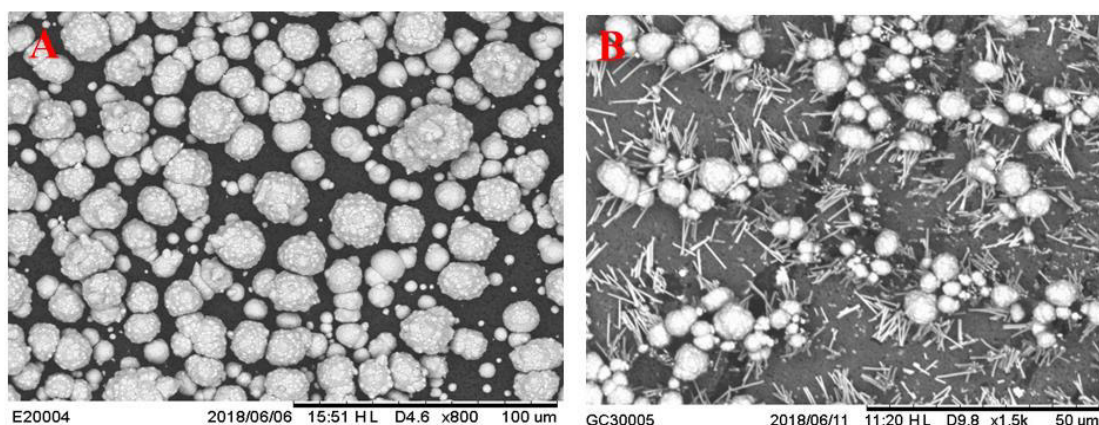


Figure 4.3 SEM images of copper NWs poured out of the pores of a polycarbonate membrane A) before and B) after the etching procedure.

4.2 Materials and methods

4.2.1 Materials

All the chemicals used in the preparation of the AgNSs were purchased from Sigma-Aldrich (see Chapter 2). The polycarbonate filter membranes, coated with the wetting agent polyvinylpyrrolidone, were supplied by SPI-Pore Filter (47 mm filter diameter, 10 μm filter thickness, 400 nm pore diameter, $1 \cdot 10^8$ pores/ cm^{-2} pore density). The alumina membranes, Anodisc47, were characterized by 200 nm pore diameter, 60 μm filter thickness, $1 \cdot 10^9$ pores/ cm^{-2} pore density. 5% Nafion®117 hydroalcoholic solution (monomer unit: $\text{C}_7\text{HF}_{13}\text{O}_5\text{S} \cdot \text{C}_2\text{F}_4$) was purchased from Sigma Aldrich.

4.2.2 Synthesis of AgNSs

The preparation of AgNSs has been previously described (see Chapter 2) [1].

4.2.3 Electrochemical deposition of CuNWs

CuNWs were electrochemically deposited in both polycarbonate and alumina membranes. One side of the membrane was sputtered with a thin layer of gold by Ar plasma [2]. and then fixed to the surface of the working electrode (WE) by means of Nafion®117, used in this case as a kind of polyelectrolytic glue. Glassy carbon (diameter 5 mm) or copper disks (diameter 3 mm) were employed as working electrodes, while two copper spirals or sheets were used as the counter (CE) and pseudo-reference electrode (Cu_{REF}), respectively (Figure 4.4). The presence of the copper CE guarantees a continuous refueling of Cu^{2+} ions which would be otherwise quickly consumed by the deposition of metallic copper at the WE.

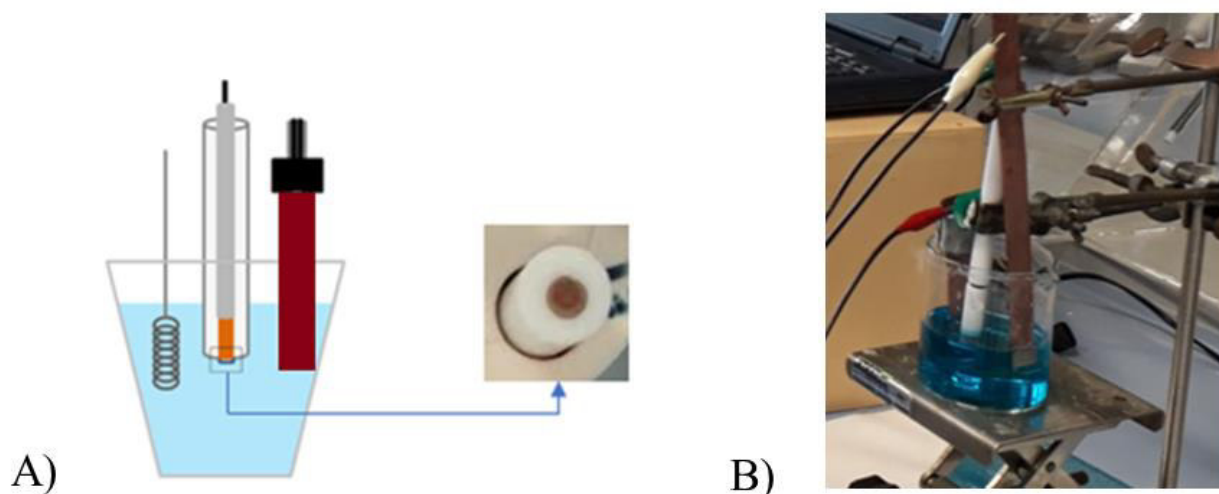
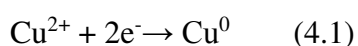


Figure 4.4 A) Scheme representing a three-electrode cell composed by a counter electrode (left) which acts as an anode, the working electrode (middle) which is the cathode and a reference electrode (right). The membrane fixed on the WE is shown by a picture at right. B) Picture of the three-electrode cell employed for the electrochemical deposition.

The electrolytic solution was composed by CuSO_4 acidified with H_2SO_4 . A constant reducing potential was applied in order to reduce the Cu^{2+} ions to metallic Cu inside the pores, following the reaction:



The deposition was studied through chronoamperometric technique, able to record the trend of the current as a function of time.

4.2.4 Preparation of the samples for the Raman analysis

The macro-Cu plates and CuNWs ensembles employed for the benzenethiol (BT) detection were prepared as follows:

7. overnight immersion in 10 mM cysteamine water solution [27];

8. overnight immersion in the colloidal suspension of nanoparticles (AgNPs or AgNSs);
9. overnight immersion in 10^{-3} M BT ethanolic solution [13].

4.2.5 Instrumentation

Potentiostat

For the deposition of CuNWs and the electrochemical measurements a CH1000 potentiostat (CH Instruments, USA) was employed. In detail, cyclic voltammetry and chronoamperometry were used as techniques.

Scanning electron microscopy (SEM) – energy dispersive X-ray spectroscopy (EDS)

A TM3000 Hitachi scanning electron microscope coupled to the software SwiftED3000 for the EDS analysis was employed to characterize the nanoporous membranes and the NWs. The electron beam was used with a power of 15 keV and the acquisition time for the EDS spectra was 3 minutes.

Raman spectrometer

Raman measurements were performed by means of a portable spectrometer i-Raman 785S (B&W Tek Inc, Newark, DE, USA) operating with a 785 nm diode laser of variable power electronically tunable (between 3 and 300 mW with 1% intervals), which was connected through optical fibres (1.5 m length) to a BAC102 Raman Trigger Probe (B&W Tek) equipped with a standard 304SS shaft mounting a flat quartz window. The spectrometer was matched with a BAC 151B (B&W Tek) microscope. The Rayleigh radiation was blocked by a notch filter, and a LWP (long wave pass) filter removed the elastically diffused radiation fraction in order to measure Raman peaks up to 150 cm^{-1} from Rayleigh limit. The backscattered Raman radiation was dispersed by a holographic grating on a TE Cooled Linear 2048 pixels CCD Array at $10\text{ }^{\circ}\text{C}$. The entrance slit width was fixed at $25\text{ }\mu\text{m}$. Spectra were collected in the $175\text{-}3000\text{ cm}^{-1}$ fixed spectral range, with a nominal spectral

resolution of 4.5 cm^{-1} , typical integration times of 20 s, 3 accumulation cycles to improve the signal-to-noise ratio, keeping the laser power at 15 mW according on the material response and using a 20X objective. Data were registered employing the dedicated BWSpec4 software and then analyzed with Origin software.

4.3 Results and discussion

4.3.1 Voltammetric study of Cu^{2+} ions reduction

In order to find out the best conditions for the electrochemical deposition of copper, some preliminary analyses were carried out by cyclic voltammetry in different solutions of acidified CuSO_4 . For the sake of simplicity, only the cyclic voltammograms obtained by using the solutions of CuSO_4 0.01 M, H_2SO_4 0.01 M and Na_2SO_4 0.5 M will be reported and discussed in detail. The measurements were performed using two different working electrodes: copper or glassy carbon.

The cyclic voltammogram shown in Figure 4.5-A, recorded at 40 mV/s using a copper working electrode, shows a cathodic peak at around -0.250 V vs. Cu_{REF} . The anodic branch of the CV is characterized by an almost linear growth of the current at potentials higher than $+0.02 \text{ V}$ (vs Cu_{REF}).

The reduction peak, whose current increases with the square root of the scan rate, is due to the two-electron reduction of Cu^{2+} ions (see eq. 4.1) which diffuse from the bulk solution to the surface of the electrode. The anodic current runs up without creating a peak because it corresponds to the oxidation of both the metallic copper deposited during the cathodic branch of the CV and that constituting the WE itself. In the case of glassy carbon WE (Figure 4.5-B), the cathodic branch of the voltammogram presents a diffusion controlled peak ($E_p = -0.3/-0.36 \text{ V}$ vs Cu_{REF} , peak current increasing linearly with $v^{1/2}$), while the anodic one shows a symmetric stripping peak with $E_p \approx 0.140 \text{ V}$ vs Cu_{REF} . Also in this case the cathodic peak corresponds to the reduction exposed in the equation 4.1, while the anodic one to the reverse reaction, that is the re-oxidation of the metallic copper electrodeposited on the glassy carbon surface to regenerate Cu^{2+} ions in solution. It is

interesting to note that the reduction peak of Cu^{2+} to Cu^0 is shifted to more negative potentials than on copper. In fact, it is known that the less favourite energetic process in electrodeposition is the formation of the first crystal nuclei: on a copper electrode they are already formed, while on a different material (i.e. glassy carbon) they must be created during the cathodic scan itself.

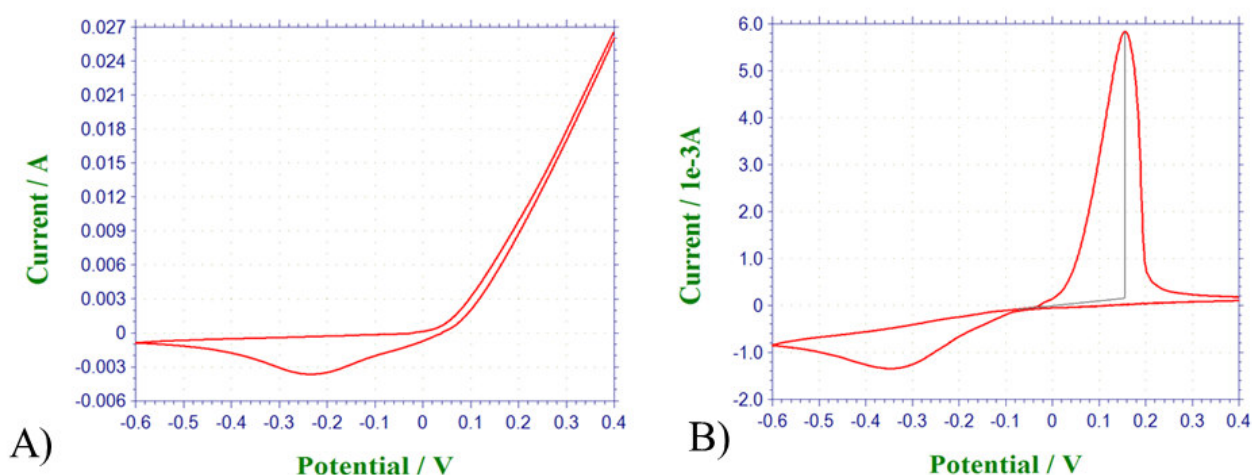


Figure 4.5 Cyclic voltammograms recorded at 40 mV/s scan rate showing the reduction of Cu^{2+} ions in a three-electrode cell from a solution of CuSO_4 0.01 M acidified with H_2SO_4 0.01 M and Na_2SO_4 0.5 M on A) Cu and B) GC working electrodes (vs Cu_{REF}).

The obtained results indicate that the electrodeposition on copper occurs at less negative potentials on Cu than on GC (respectively -0.25 V and -0.3 V vs Cu_{REF}). On the other hand, copper electrodes tend to get oxidized extremely easily, even at low oxidation potentials, while GC does not present this shortcoming.

4.3.2 Optimization of copper nanowires deposition in nanoporous membranes

According to what discussed in the previous paragraphs, we tried to deposit copper on different working electrodes (copper and glassy carbon) covered with nanoporous membranes. In particular, the aim of the experiment was to investigate the influence of different electrolytes and of the potential applied in the deposition of CuNWs within the template alumina or polycarbonate membranes.

Template deposition of CuNWs in polycarbonate membranes

After the sputtering procedure, the polycarbonate membranes were cut in discs of 3 mm diameter. Then, they were fixed on the electrode by means of Nafion®117 solution, diluted to 0.5% with methanol. According to the results obtained, the best conditions to deposit CuNWs in polycarbonate are the following:

- Deposition solution: CuSO_4 0.3 M, H_2SO_4 0.001 M and NaSO_4 1 M;
- Deposition time: 180 seconds on copper working electrode and 140 seconds on glassy carbon at -400 mV.

Figure 4.6 presents the typical chronoamperogram recorded during the electrodeposition. The deposition is stopped when the current reaches a plateau, in order to prevent the formation of a metal deposit protruding out of the pores. In order to prevent this result, the experimentally established deposition times, 180 s on copper and 140 on GC, should not be exceeded.

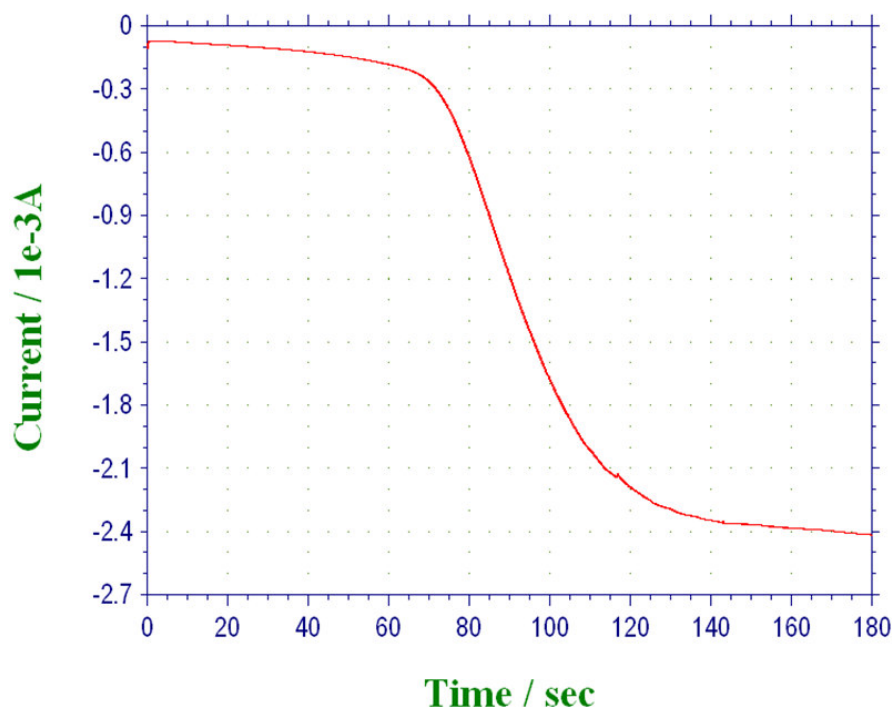


Figure 4.6 Chronoamperogram showing the deposition of CuNWs in a polycarbonate membrane with 400 nm pores, fixed on a copper electrode, applied potential: -400 mV vs Cu_{REF} .

Thereafter, the membranes were etched in pure dichloromethane (DCM) for one minute. The copper nanowires deposition has been studied by scanning electron microscope (SEM) coupled with EDX probe in order to check the growth of the copper nanowires and the efficacy of the etching and, at the same time, to confirm the deposition of copper. Figure 4.7 and 4.8 show the SEM images of CuNWs deposited on copper and GC electrodes, respectively. The results obtained indicate that electrodeposition of CuNWs on a copper working electrode produced denser arrays of NWs than on glassy carbon, probably because with the latter WE many pores remained empty.

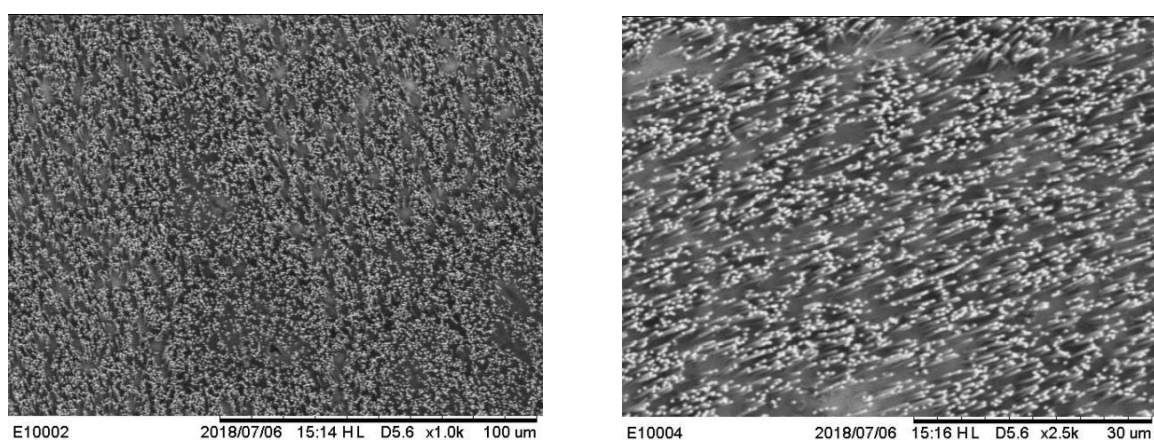


Figure 4.7 SEM images of CuNWs electrodeposited using a track etched polycarbonate membrane with 200 nm pores, on copper electrode. Images recorded after etching the polycarbonate with pure DCM for one minute.

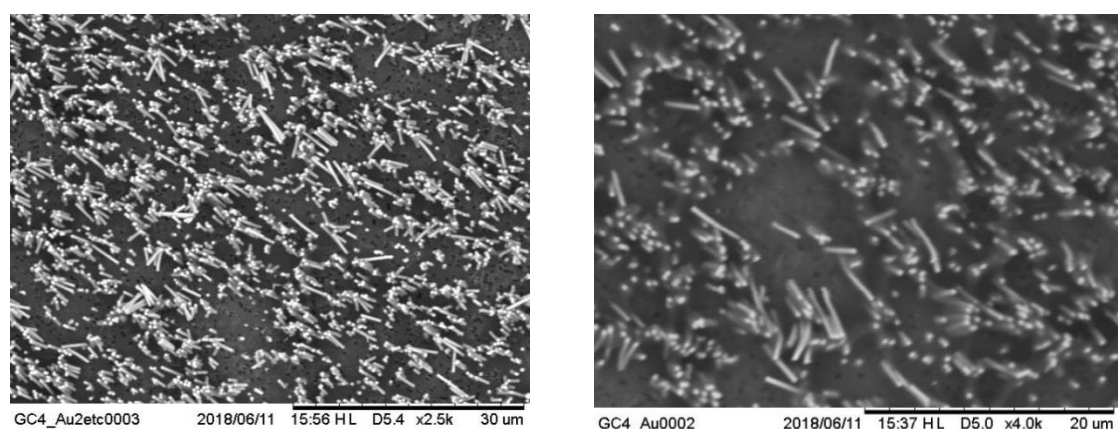


Figure 4.8 SEM images of CuNWs electrodeposited on glassy carbon electrode. Images recorded after etching the polycarbonate with pure DCM for one minute.

In all cases the EDX spectra confirmed the presence of copper, together with some carbon and oxygen, from residual polycarbonate and Nafion®117, and sulphur and fluorine due to Nafion®117 (Figure 4.9).

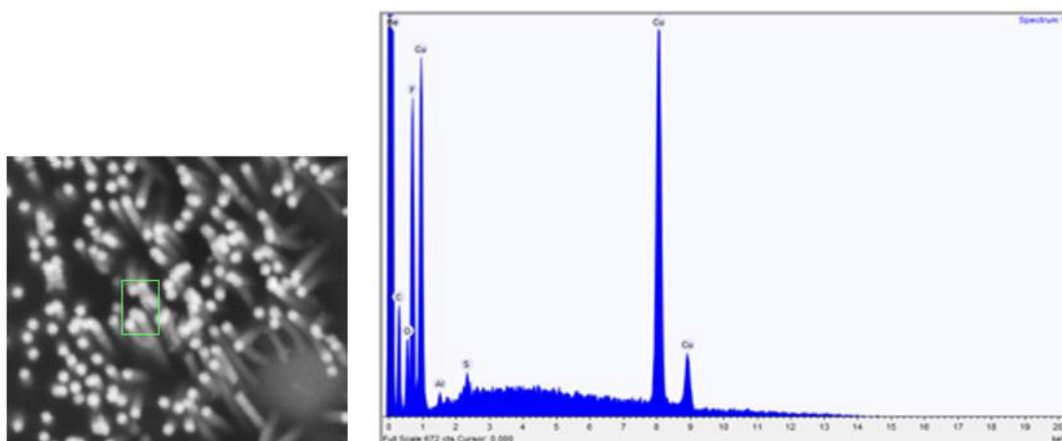


Figure 4.9 EDX spectrum, acquired at the showed area, revealing the presence of CuNWs.

Template deposition of CuNWs in alumina nanoporous membranes

The alumina membranes underwent gold sputtering for 30 seconds. Thereafter, they were cut in irregular fragments due to their fragility. Fragment of dimension suitable to cover all the WE was fixed on the electrode with pure Nafion®117.

After preliminary tests, the best condition to deposit copper nanowires in alumina templates resulted the following:

- Deposition solution: CuSO_4 0.6 M, H_2SO_4 and Na_2SO_4 0.01M
- Deposition time: 300 s at - 250 mV vs Cu_{REF} on copper working electrode; no positive result was achieved on GC electrode.

After the deposition, the membranes were etched in NaOH 5 M for 15 minutes (Figure 4.10-A). Also in this case microscopic analysis witnessed the growth of the CuNWs, while elemental spectra confirmed that the metal deposited within the pores was copper (Figure 4.10-B).

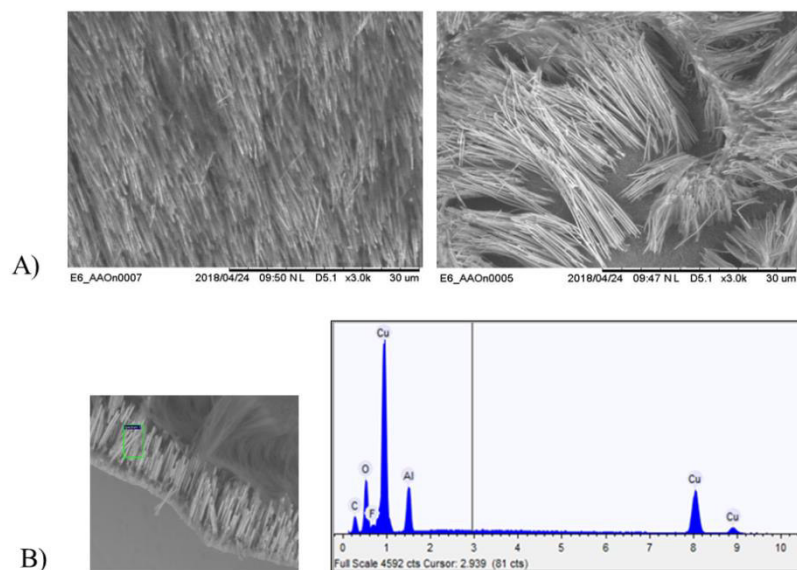


Figure 4.10 A) SEM images of CuNWs electrodeposited in an alumina membrane on copper electrode; B) EDS spectrum showing the presence of Cu.

Summary on membrane templated CuNWs electrodeposition

Comparing the information obtained from the tests made, the following information was obtained:

- The growth of the CuNWs within the polycarbonate membranes occurs successfully both on glassy carbon and copper working electrodes, while in the case of aluminium oxide membranes it is successful only on copper;
- CuNWs in polycarbonate resulted denser when deposited on copper electrode than on GC.

On account of that, polycarbonate membranes were preferred rather than the alumina ones which are in addition more fragile and difficult to manipulate. As far as the electrode material is concerned, copper resulted the most suitable one.

4.3.3 SERS on CuNWs and AgNSs@CuNWs substrates

In order to test the Raman enhancement produced by these copper-based SERS substrates, benzenethiol (BT) [13-15] was again chosen as reference Raman probe. A copper plate, named

hereafter macro-copper, was employed as control. Figure 4.11 shows the spectra obtained from the analyses of BT adsorbed from a 10^{-3} M methanolic solution, adsorbed on different substrates. In absence of nanoparticles it was not possible to detect any Raman signal of the analyte (Figure 4.11-a). Instead, when CuNWs are employed as substrate (Figure 4.11-b), the bands of BT appear, even though weak and together with interferences (band at 1305 cm^{-1}). BT on AgNSs@macro-copper (Figure 4.11-c) resulted easily detectable thanks to the high enhancement produced by the presence of the Ag nanoparticles. The signal appear even more intense when the hierarchical structure AgNSs@CuNWs was employed (Figure 4.11-d).

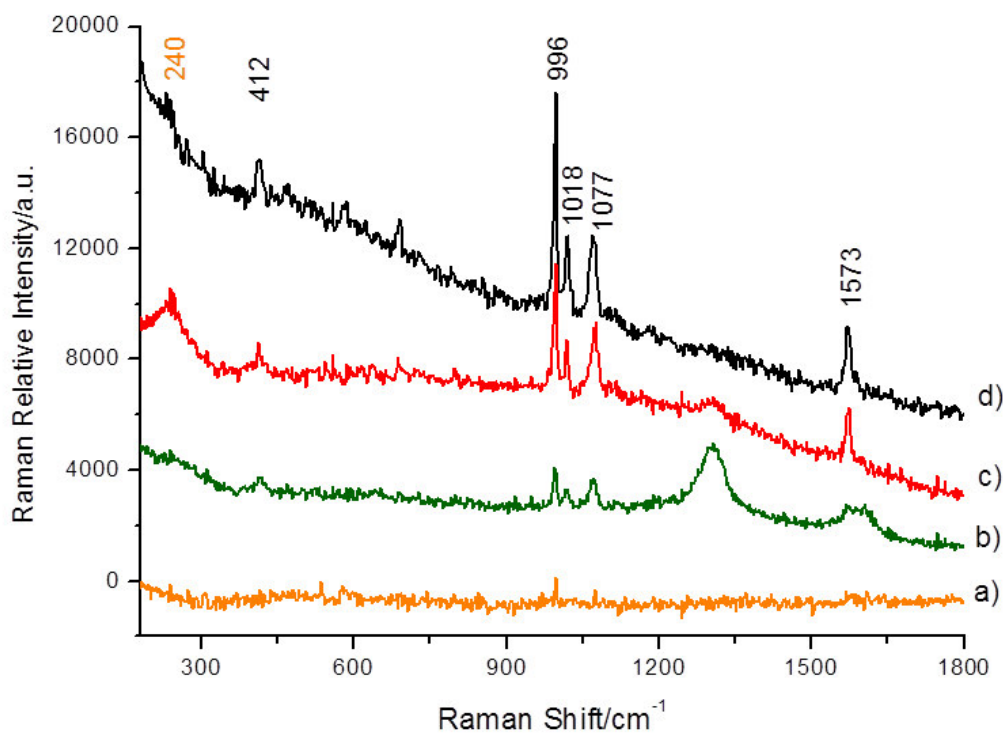


Figure 4.11 SERS spectra of 10^{-3} M BT recorded on a) macro-copper; b) CuNWs; c) AgNSs@macro-copper and d) AgNSs@CuNWs ($\lambda_{\text{ex}}=785\text{ nm}$, $P=15\text{ mW}$, $t=3 \times 20\text{ s}$).

Table 4.1 summarizes the main bands of the SERS spectra shown in Figure 4.11, with their assignation and the comparison with those reported in literature [16]. The band at around 240 cm^{-1}

is caused by the presence of nanomaterials and, in this particular case, is due to the interaction of Ag^+ cations interacting with anions present in the colloidal solution (Figure 4.11-d) [17].

Table 4.1 Comparison between bands (cm^{-1}) of BT reported in literature with their assignments and those experimentally obtained [16]. To describe the relative intensity and the shape of the bands: br = broad; sh = shoulder, w = weak, m = medium and s = strong.

Reference [16]	Macro-copper	AgNSs@macro-copper	CuNWs	AgNSs@CuNWs	Assignments
420	-		412 w	412 w	$\nu(\text{C-S})$ /ring in-plane deformation
998	-	996 s	996 m	996 s	Ring out-of-plane deformation/ $\gamma(\text{C-H})$
1022	-	1018 m	1018 w	1018 m	Ring in-plane deformation/ $\nu(\text{C-C})$
1072	-	1070 s	1076 m	1076 s	$\nu(\text{C-C})/\nu(\text{C-S})$
1571	-	1570 m	1573 br	1573 s	$\nu(\text{C-C})/\nu(\text{C-S})$

4.4 Conclusions

The results obtained and presented were compared and interpreted in order to reach some conclusions. Polycarbonate membranes were preferred rather than alumina ones which are fragile and do not guarantee the electrodeposition of CuNWs on GC electrodes. In relation to the material of the electrode, copper promotes the formation of crystal nuclei during the deposition, generating ordered and dense nanowires. The detection of BT was possible only in presence of nanomaterials able to generate a plasmonic effect. Standing alone CuNWs produce a Raman enhancement which is much less intense than the one caused by AgNSs@macro-copper, witnessing the high efficiency of AgNSs. Their properties are further improved when they are bound to another nanomaterial in a hierarchical nanostructure, such as AgNSs@CuNWs.

References

- [1] A. García-Leis, J.V. García-Ramos, S. Sánchez-Cortés, *J. Phys. Chem. C* **2013**, *117*, 7791.
- [2] A.M. Stortini, L.M. Moretto, A. Mardegan, M. Ongaro, P. Ugo, *Sens. Actuator B-Chem.* **2015**, *207*, 186.
- [3] E. Le Ru, P. Etchegoin, Elsevier, Amsterdam, The Netherlands, **2009**.
- [4] S. Chandra, A. Kumar, P. Kumar Tonar, *J. Saudi Chem. Soc.* **2014**, *18*, 149.
- [5] K. Kim, H.S. Lee, *J. Phys. Chem. B* **2005**, *109*, 18929.
- [6] G.E. Possin, *Rev. Sci. Instrum.* **1970**, *41*, 772.
- [7] W.D. Williams, N. Giordano, *Rev. Sci. Instrum.* **1984**, *55*, 410.
- [8] R.M. Penner, C.R. Martin, *Anal. Chem.* **1987**, *59*, 2625.
- [9] J.W. Diggle, T.C. Downie, C.W. Goulding, *Chem. Rev.* **1969**, *69*, 365.
- [10] V.P. Menon V.P, C.R. Martin, *Anal. Chem.* **1995**, *67*, 1920
- [11] P. Ugo, L.M. Moretto, *Template Deposition of Metals. In C. Zosky (ed.), Handbook of Electrochemistry*, **2007**, chapter 16.2, Elsevier, Amsterdam.
- [12] T.M. Whitney, P.C. Searson, J.S. Jiang, C.L. Chien, *Science* **1993**, *261*, 1316.
- [13] M. Zamuner, D. Talaga, F. Deiss, V. Guieu, A. Kuhn, P. Ugo, N. Sojic, *Adv. Funct. Mater.* **2009**, *19(44)*, 3129.
- [14] A.D. McFarland, M.A. Young, J.A. Dieringer, R.P. Van Duyne, *J. Phys. Chem. B* **2005**, *109*, 11279.
- [15] N. Valley, N. Greeneltch, R.P. Van Duyne, G.C. Schatz, *J. Phys. Chem. Lett.* **2013**, *4*, 2599.

- [16] J. Fontana, J. Livenerec, F. J. Bezaresd, J. D. Caldwell, R. Rendell, B. R. Ratna, *Appl. Phys. Lett.*, **2013**, *102*, 20160.
- [17] M.V. Cañamares, J.V. García-Ramos, C. Domingo, S. Sánchez-Cortés, *Vib. Spectrosc.* **2006**, *40*, 161.
- [18] K. Kim, H.S. Lee, *J. Phys. Chem. B* **2005**, *109*, 18929.
- [19] K. Kim, J. Choi, K.S. Shin, *J. Phys. Chem. C* **2013**, *117*, 11421.

Chapter 5

Hierarchical nanostructures composed by sphere segment void substrates decorated with Ag nanostars

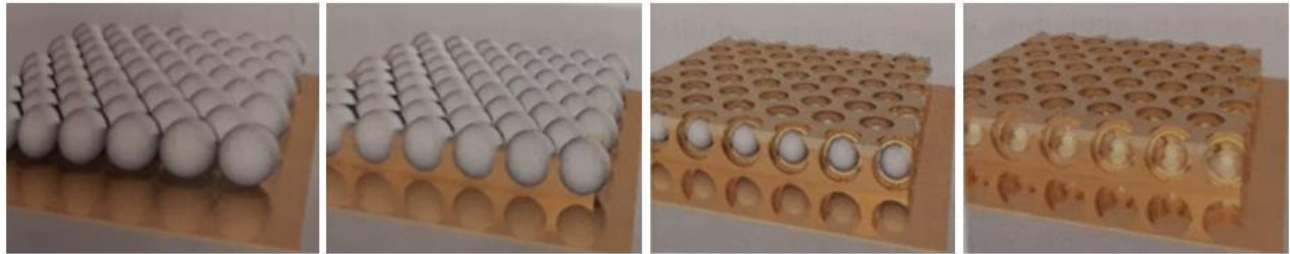
5.1 Introduction

The experimental part exposed in this chapter was mainly carried out during a stage in the group of Prof. Philip N. Bartlett at the University of Southampton. Aim of the present work is the combination of Ag nanostars with highly ordered gold surfaces, namely the sphere segment void (SSV) substrates, which are already known to produce efficient Raman enhancements. The idea here was to study whether synergetic effects can arise by combining SSV structures with the AgNSs and, eventually, to compare the magnitude of possible SERS enhancements with those achieved with the nanowires based structures, presented in Chapters 3 and 4. The SSV gold nanostructures have been developed by the Phil Bartlett and coworkers and are obtained by templated electrodeposition of gold, using a monolayer of polystyrene spheres as templating material, later removed by chemical dissolution of the template. Two sizes of polystyrene were employed: 600 and 220 nm. For the present aims, the SSV substrates were decorated with Ag nanostars (AgNSs) to produce hierarchical nanostructures that will be named here AgNSs@SSV. In the following part of this introduction, principles on the preparation of SSV structures and their SERS activity will be briefly presented.

5.1.1 SSV substrates

SSV substrates are thin layer metallic films with an ordered arrangement of spherical cavities prepared by using a monolayer of closed packed polystyrene spheres as template (see Figure 5.1)

[1,2]. It is possible to use one or more monolayers of templating particles, as well as to stop the gold deposition at a desired filling level.



1) Nanosphere template 2) Electrodeposition 3) Dissolution of spheres 4) SSV surface

Figure 5.1 Steps for the preparation of an SSV substrate: 1) a closed-packed monolayer of polystyrene spheres is used as template; 2) the electrodeposition of gold reach $0.5d$ of the spheres; 3) the deposition is stopped when the gold height is the 80% of the spheres; 4) the spheres are dissolved in dimethylformamide (DMF) leaving a SSV surface. Adapted from [3].

These substrates can be modified by choosing the sphere size and the deposition height, obtaining in this way a tunable electromagnetic enhancement. Indeed, in order to achieve the maximum enhancement, plasmons have to couple with both the incident and the scattered radiation. A plasmon is a collective oscillation of charges in a metal and when the fluctuation of charges is a metal-dielectric interface we talk of a surface plasmon. A surface plasmon which couples with an electromagnetic wave is called a surface plasmon polariton (SPP) [4]. SSV substrates have three main types of plasmon mode (Figure 5.2) [2,4,5]:

- Mie plasmons, generated inside the truncated empty spheres,
- Bragg plasmons, produced on the top surface between the truncated empty spheres;
- Rim plasmons, generated at the upper rim of the truncated empty spheres.

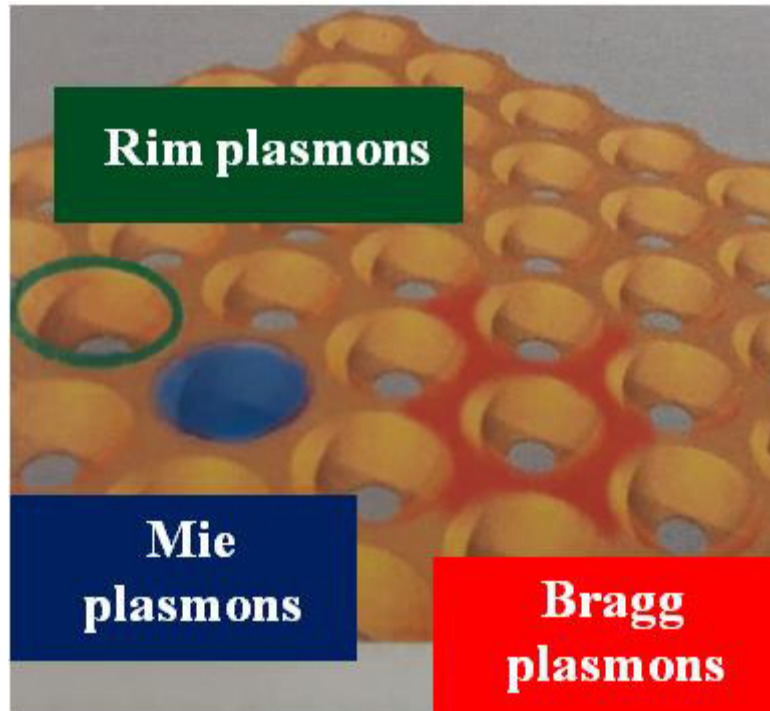


Figure 5.2 Location of the different plasmons on a SSV substrate: Rim plasmons are at the upper rim of the voids, Mie plasmons reside in the voids and the Bragg plasmons are delocalized on the flat surface between the voids. Adapted from [4,6].

The structural morphology of the substrate influences the type of plasmons that can be generated. In the case of SSV, the morphology can be controlled by changing the diameter of the spheres and the deposition height. The employed spheres have a fixed diameter (600 and 220 nm) and three main situations can be distinguished on the deposition height (Figure 5.3):

- $0.3d$ (30% of the diameter): Bragg plasmons are produced due to the presence of the continuous flat surface connecting the voids [2,5];
- $0.3d-0.7d$: Mie plasmons arise since truncated spherical voids are present [6];
- $>0.7d$: Bragg and Rim plasmons are produced due to the presence of continuous top flat surface and the complete upper rim [2,5]. Mie plasmons are present too [6].

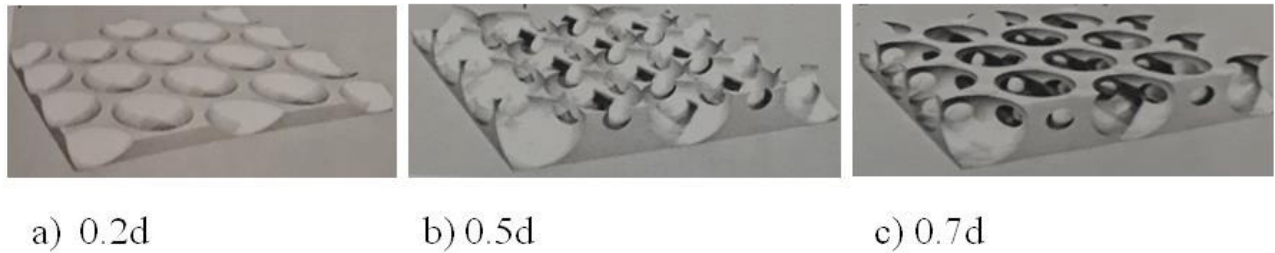


Figure 5.3 Schemes representing an SSV substrate at a) 0.2d, b) 0.5d, and c) 0.7d. Mie plasmons are present only when the truncated spheres are present (b,c); Bragg plasmons are generated when there is a continuous top surface (a,c); Rim plasmons are present when there is a complete rim around the top edge of the void (a,c). Adapted from [6].

Different types of plasmons can hybridize by overlapping [4,7]. In particular, this phenomenon occurs when the height of the spheres is about 0.8d, which corresponds to 480 nm [4]. When Mie and Rim plasmons mix, two new energy modes are generated. The one with higher energy (approximately 2 eV) is resonant with the 633 nm (1.96 eV) pump laser.

SSV are produced by hard-template synthesis with the employment of polystyrene spheres. The template is prepared by exploiting the convective assembly process [8]. During the controlled evaporation of water from the solution of colloidal particles, the capillary immersion force makes the particles collide and drives the formation of the colloidal crystal template [5].

5.1.2 Particle-in-cavity architectures

Structured gold SSV surfaces were already combined to spherical silver nanoparticles [9]. These architectures, called particle-in-cavity (PIC), showed an extremely strong field enhancement, namely $3.1 \cdot 10^4$ times more intense than the one produced by the bare cavities (Figure 5.4) [10]. Indeed, the cavities act effectively as light harvesters and the nanoparticles further focus the optical fields near the surface of these metallic nanovoids. The presence of silver nanostars, with their anisotropic shape, can improve the field enhancement. The wettability of the SSV surface must be

considered in order to understand how the water dispersion of the nanoparticles can cover a surface which becomes hydrophobic at a sub-micrometer scale and which present both curved and flat areas [11-13].

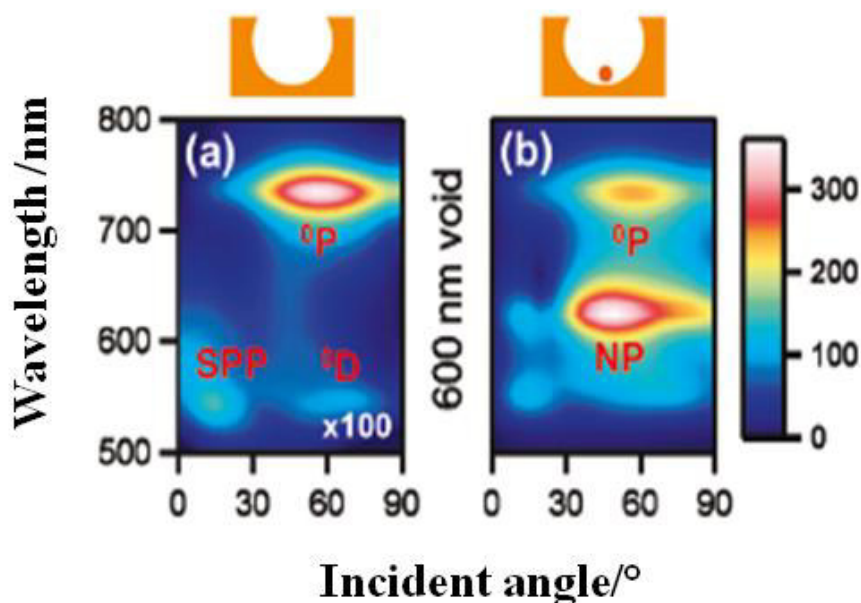


Figure 5.4 Calculated field enhancement spectral maps of a) Au void of diameter 600 nm empty voids and b) with a 60 nm Au sphere 1 nm away from the void surface. Note: color scales of (a) is multiplied by factor of 100. Adapted from [9].

5.2 Materials and methods

5.2.1 Materials

For the electroless gold deposition the following chemicals were employed: flat macro-gold slides which were prepared by vapour deposition of a 10 nm chromium adhesion layer followed by 200 nm of gold onto a standard glass microscope slide (Menzel-Glazer); gold surface cleaning solution (product number: 667978, Sigma-Aldrich); polystyrene spheres with a diameter of 600 and 220 nm, produced as 1% wt. aqueous solution (Thermo Scientific); electroplating solution -ECF 60-Technic Inc.- and brightener -E3- (Metalor Technologies); dimethylformamide (Sigma-Aldrich). Concerning

the Raman probe molecules, the following analytes were employed: benzenethiol (Sigma-Aldrich), carminic acid (Sigma-Aldrich), cochineal lake, madder lake and indigo (Zecchi, Florence).

5.2.2 Synthesis of AgNSs

We used here the AgNSs preparation procedure described previously in Chapter 2.

5.2.3 Synthesis of SSV

The flat macro-gold slides were cut into 19 mm x 13 mm pieces through a diamond point to be used as supports for SSV (Figure 5.5-1). The gold surfaces were cleaned by leaving them in a gold surface cleaning solution for 40 sec. Then they were dried by using compressed air. A spacer made of Parafilm (around 100 μm thick) with an inverted trapezoidal shape (15 and 7 mm x 12 mm) (Figure 5.5-2) was employed to construct a thin layer cell with a coverslip (Figure 5.5-3). The three layers were made to adhere to each other by heating up for a few seconds on a hot plate (around 80 $^{\circ}\text{C}$). Two different sizes of polystyrene spheres were employed in this research project, namely 600 and 220 nm. The polystyrene spheres were produced as 1% wt. aqueous solution and present a NIST Traceable diameter of $596 \text{ nm} \pm 9$ and 216 ± 4 . The stock solution was centrifuged 15 minutes at 6000 rpm and then a precise quantity of the supernatant was discarded to get a 1.8 % wt. solution. Therefore, the space between the gold layer and the coverslip was filled with a 10 μL of a colloidal sphere solution using a micropipette (Figure 5.5-4) and left in a constant temperature in incubator (about 13 $^{\circ}\text{C}$) on a tilted support for 48 hours.

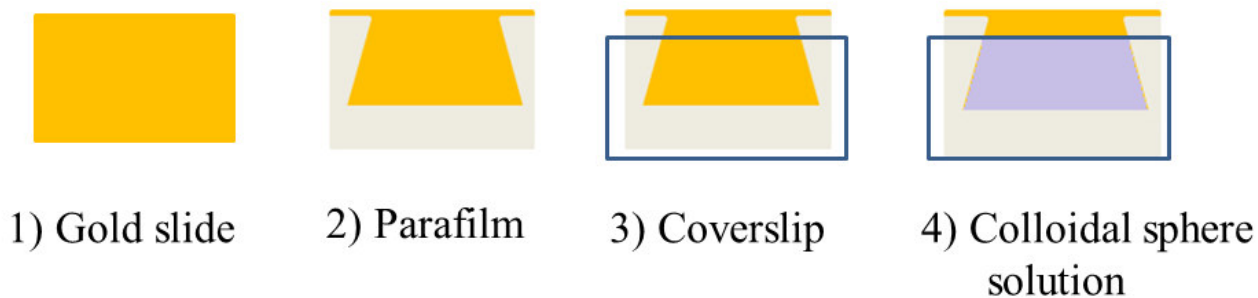


Figure 5.5 Scheme showing the preliminary steps to prepare an SSV substrate: 1) a gold coated glass slide is cut into 19 mm x 13 mm; 2) a spacer made of Parafilm with an inverted trapezoidal shape is placed on the slide; 3) a coverslip is placed on the slide to construct a thin layer cell; 4) the cell is filled with 10 μ L of a colloidal solution of polystyrene spheres using a micropipette.

A monolayer of hexagonally close packed polystyrene spheres is assembled from the colloidal suspension of monodisperse particles during a controlled evaporation process. Figure 5.6 shows the self-assembly of the spheres, driven by a capillary immersion force which makes the particle collide.

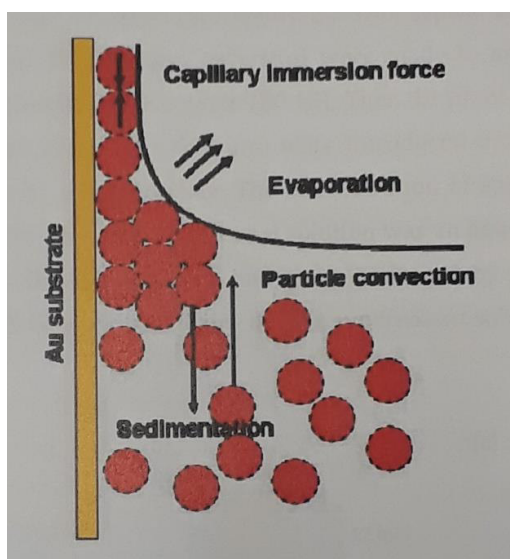


Figure 5.6 Self-assembly of colloidal spheres at a gold substrate. Adapted from [6].

The following step was the electrodeposition of gold by employing the monolayer of polystyrene spheres as template. A transparent nail varnish was used as insulating paint to be applied on the whole slide, except for the contact area with the crocodile clip used for connection with the potentiostat. The electroplating solution employed was cyanide free and based on gold sulphite. 10 μL of a brightener were added to every 10 mL of the plating solution to obtain a smooth and bright finish of the deposit. The deposition was carried out in a three-electrode glass cell at room temperature. A saturated calomel electrode (SCE) was used as reference electrode, a platinum mesh as counter electrode and the template as working electrode (Figure 5.7).



Figure 5.7 Picture showing the three-electrode glass cell employed to carry out the electrodeposition of gold.

The template was immersed in the plating solution for a few minutes to let it reach the equilibrium before the potentiostatic pulse. The required amount of charge was calculated on the basis of the amount of current on the template at the half deposition height (300 and 110 nm) and the desired deposition height (480 and 176 nm). A potential of -0.72 V was applied until reaching the calculated amount of charge. Figure 5.8 shows the typical deposition chronoamperogram. Initially the current increased abruptly at the beginning of the gold deposition because of the increase of the conductive surface with the deposition, then it decreased slowly along with the decreasing

deposition area. It was noticed the presence of a little peak at around $t = 30$ s, which indicates the arrangement of the spheres. After this, a more intense broad cathodic peak at $t = 135$ s is observed whose top corresponds to the half deposition height. When the cathodic current started to increase again at time approximately 220 s in Figure 5.8, the deposition was stopped since the half of the diameter of the spheres has been overcome.

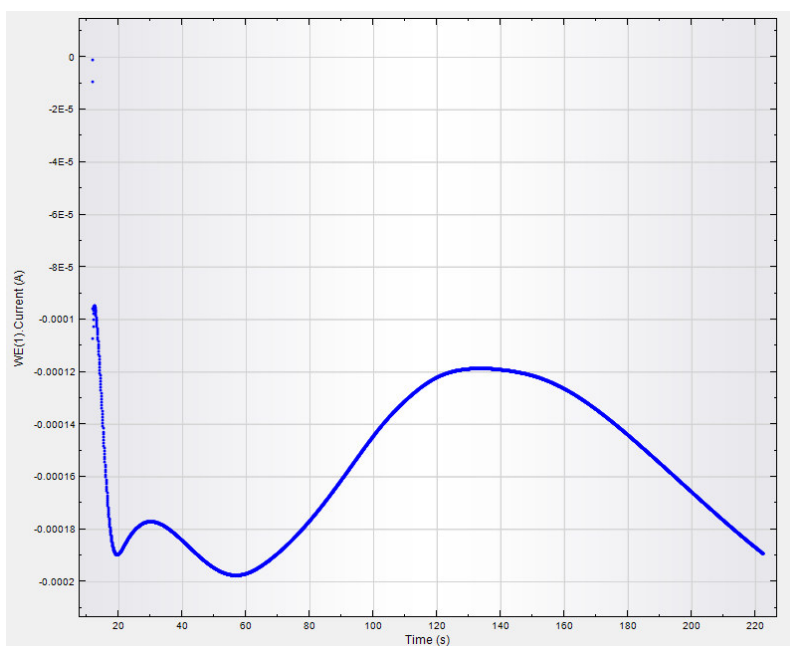


Figure 5.8 Typical chronoamperogram for an electrodeposition of gold until the 80% of the height of the polystyrene spheres at 0.72 vs. SCE.

Thereafter, the template was rinsed in ethanol, water and ethanol again and subsequently dried through compressed air. In order to remove the polystyrene, the template was placed in a vial with dimethylformamide (DMF) for 24 hours, then rinsed in ethanol and dried through compressed air for 5 minutes. Therefore, it was immersed for further 24 hours in DMF and the rinsing procedure was repeated. Figure 5.9 shows a 600 nm SSV (a) and a 220 nm SSV (b) ready to be employed, represented by the iridescent triangular surfaces on the gold slides.

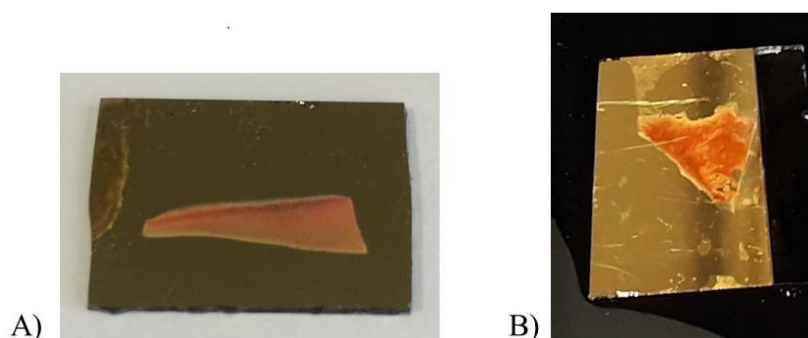


Figure 5.9 Pictures of the A) 600 nm and B) 220 nm SSV substrates after the dissolution on the polystyrene in DMF.

5.2.4 Preparation of the samples for the Raman analysis

The macro-gold slides and SSV substrates underwent different kind of preparations. These samples, meant to be Raman and SERS substrates, were employed:

1. as such;
2. decorated with AgNSs by immersion in their colloidal suspension for some hours;
3. immersed in a 10 mM water solution of cysteamine overnight [14,15] and then decorated with AgNSs.

Thereafter, all the samples were dipped in a 10^{-2} mM benzenethiol solution in ethanol overnight [16].

As far as the dyes and lake-pigments are concerned, the following coloring agent employed in the field of cultural heritage were chosen as target molecules:

1. Madder lake-pigment, an anthraquinone-based red colorant extracted from the roots of *Rubia tinctorum* and fixed on an inorganic substrate. The colour is mainly caused by the presence of alizarin (Figure 5.10) [17];

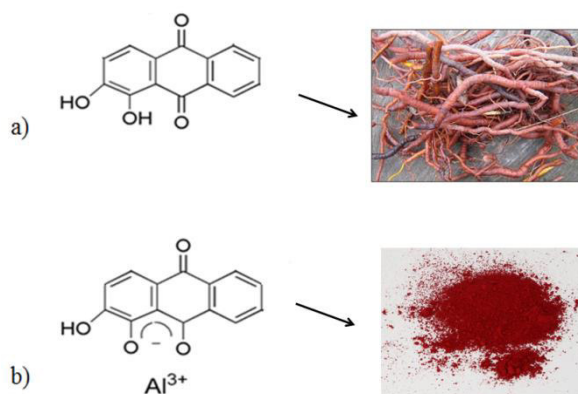


Figure 5.10 Structural formulas of a) alizarin, the main anthraquinone extracted from the roots of *Rubia tinctorum* (picture at right); b) interaction between alizarin and Al^{III} ion from the $\text{KAl}(\text{SO}_4)_2 \cdot 12\text{H}_2\text{O}$ particles. In this way the colorant is fixed on an inorganic substrate and it can be used as red lake in paintings.

2. Cochineal lake-pigment, an anthraquinone-based red colorant extracted from insects of the species *Coccus cacti* and fixed on an inorganic substrate, alum, a salt of aluminium $\text{KAl}(\text{SO}_4)_2 \cdot 12\text{H}_2\text{O}$. The molecule responsible for the colour is carminic acid (see Figure 1.13-a-b, Chapter 1) [18];
3. Pure carminic acid;
4. Indigo, a blue colorant extracted from *Indigofera tinctoria* or *Isatis tinctoria* by reducing it to its water soluble form, leucoindigo, and then re-oxidised to be used as a dye. The colouring molecule is indigo, composed by two isatin halves linked together in the respective 2- positions (Figure 5.11) [19].

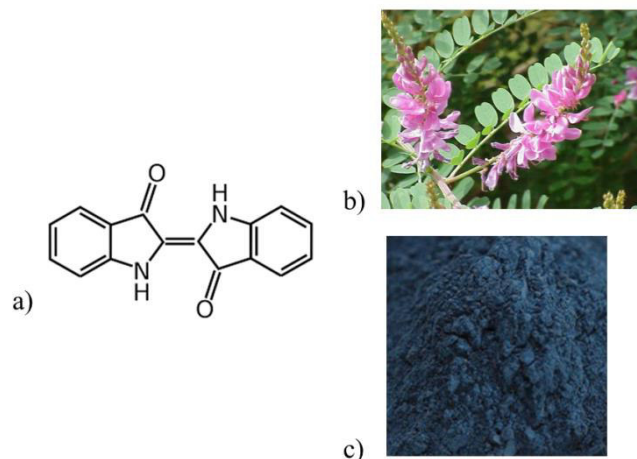


Figure 5.11 a) Structural formula of indigo which is extracted from b) the leaves of *Indigofera tinctoria* or *Isatis tinctoria*. During the extraction the molecule is reduced to the leucoindigo form, soluble in water, and then re-oxidized to be used as c) blue dye.

The substrates were prepared as already described but, since the detection of natural lake-pigments is more challenging, the AgNSs were concentrated by centrifugation and then dropped (1 μL) directly on the samples (see Chapter 4 for detailed procedure). When the drops were completely dry, the samples were immersed in a 10^{-3} M methanol solution of the dyes. In the case of pure carminic acid, the concentration step was not carried out since it was unnecessary.

5.2.5 Instrumentation

Potentiostat

The electrodeposition of gold to synthesize the SSV substrates was operated by a μ Autolab Type III potentiostat (software Nova 1.10). A potential of -0.72 V was applied until 480 nm of the 600 nm polystyrene spheres or 176 nm of the 220 nm ones. A three-electrode cell was employed, composed by a saturated calomel electrode (SCE) as reference electrode, a platinum mesh as counter electrode and the polystyrene spheres template as working electrode.

Field emission scanning electron microscopy

The morphology of the SERS substrates was characterized using a JEOL JSM 6500F FE-SEM and a Sigma-VP Carl Zeiss field-emission scanning electron microscope.

SERS and Raman spectroscopy

A Renishaw 2000 Raman spectrometer was employed to carry out the Raman and SERS measurements. The excitation laser employed was a Renishaw 785 nm laser and a CCD detector. The maximum power of the laser is 100 mW but lower powers were used during the data acquisition, typically 0.05% (0.05 mW). The collection time applied was 10 s for 1 accumulation. The spectrometer was equipped with a Leica DMLM series microscope. In order to collect scattered light at the sample, a microscope objective with a 50X magnification was employed with a short working distance (0.37 mm-numerical aperture 0.75). The spectrometer grating was calibrated by measuring the position of the most prominent band from a silicon (111) wafer (520.6 cm^{-1}).

5.3 Results and discussion

5.3.1 Characterization of the 600 and 220 nm size SSV substrates with or without AgNSs with FE-SEM

The morphological characterization of the SSV substrates was carried out by means of FE-SEM. Figure 5.12-A shows an 600 nm SSV substrate with the monolayer of spherical voids hexagonally packed [20,21]. The pore mouth is approximately 480 nm wide which corresponds to the 80% of the diameter of the spheres. The SSV substrates decorated with AgNSs are presented in Figure 5.12-B and 5.12-C without and with previous treatment with cysteamine, respectively. Each empty sphere can host a variable number of nanostars, from tens to none. Indeed, they present an average size of 100-200 nm from tip to tip. Some AgNSs can also precipitate, alone or agglomerated, on the

rims of the spheres. In this case, the presence of cysteamine does not seem to change the wettability of the surface.

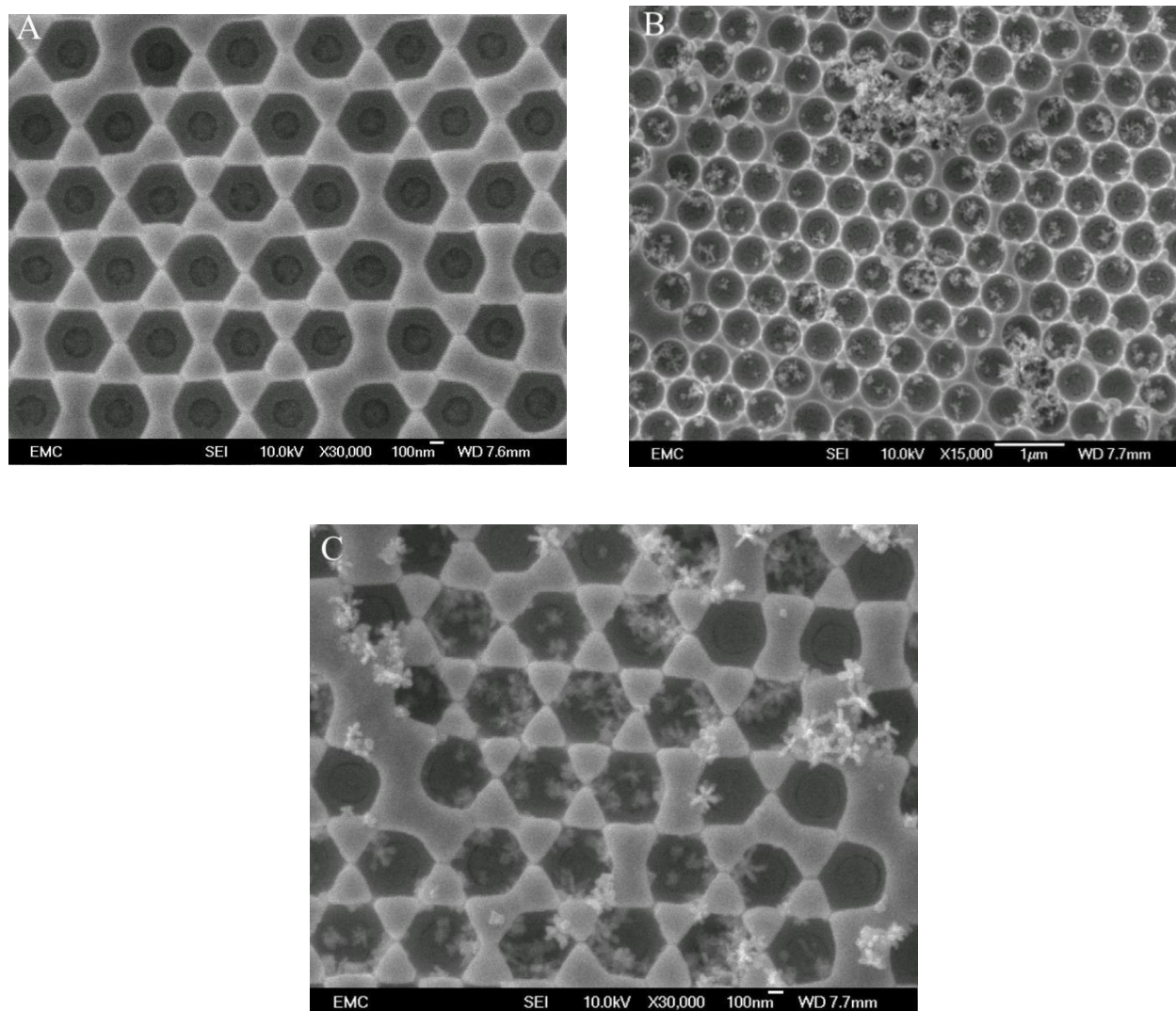


Figure 5.12 FE-SEM pictures of A) an SSV, B) an AgNSs@SSV and C) an AgNSs@SSV functionalized with cysteamine.

Figure 5.13-A shows a zoom-in image of the interesting case of a single AgNS inside an individual SSV cavity. In order to verify the presence of AgNSs on the gold substrate, the EDS spectrum of the surface was measured (Figure 5.13-B). The X-ray photons emitted by Au (3.4 atomic %) and Ag (2.5 atomic %) witnessed the contemporary presence of AgNSs and SSV structures.

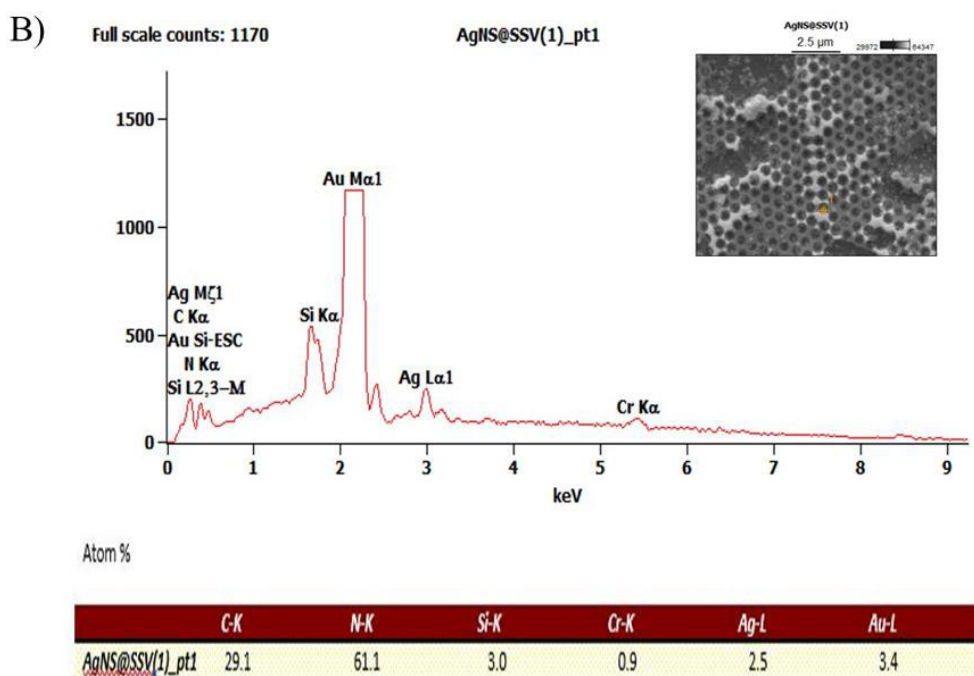
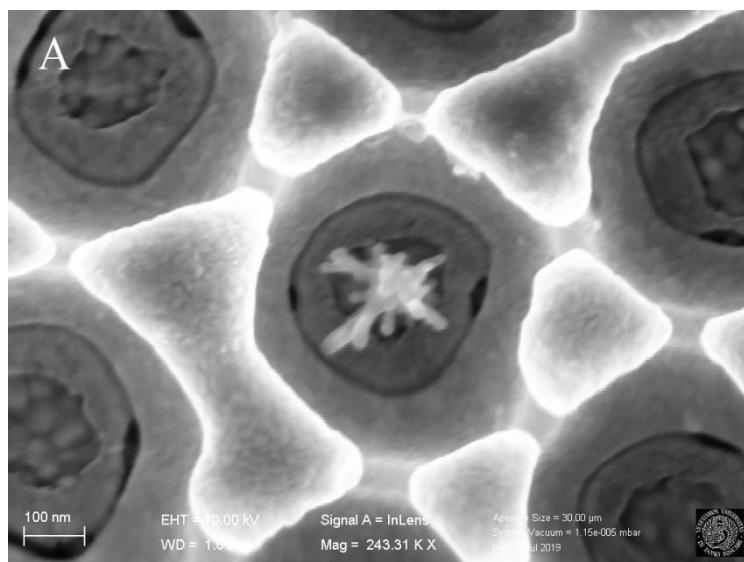


Figure 5.13 A) Zoom on a AgNS hosted in an SSV cavity; B) EDS spectrum showing the presence of Au and Ag.

To the aim of matching more strictly the average dimension of the AgNSs (100-200 nm) with the size of the SSV cavities, polystyrene spheres with a diameter of 220 nm were chosen to synthesize new SSV. The electrodeposition was carried out up to reaching the 80% of the height of the spheres

with a resulting pore mouth of 170-190 nm (Figure 5.14-A). Thereafter, the obtained substrates were functionalized with AgNSs. Figure 5.14-B shows how the AgNSs perfectly fit into the cavities of an 220 nm SSV which was not treated with cysteamine. Instead, when this bifunctional thiol was applied on the 220 nm SSV, it was observed that the AgNSs not only precipitate on the surface filling partially the hollow spheres, but also cover the hive-shaped gold surfaces (Figure 5.14-C). In this case, the wettability of the substrate is considerably modified by the presence of the thiol, possibly due to the smaller size of the cavities.

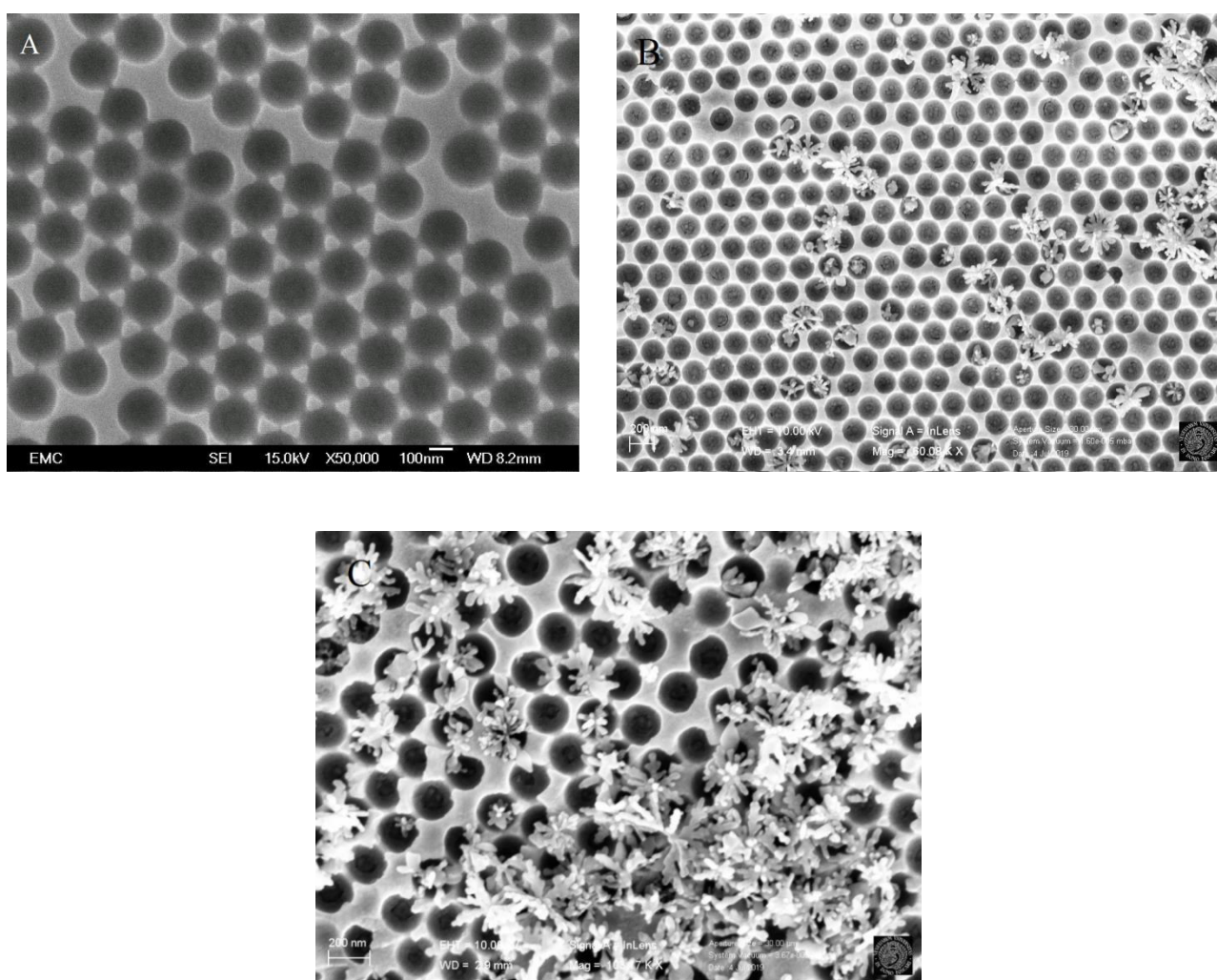
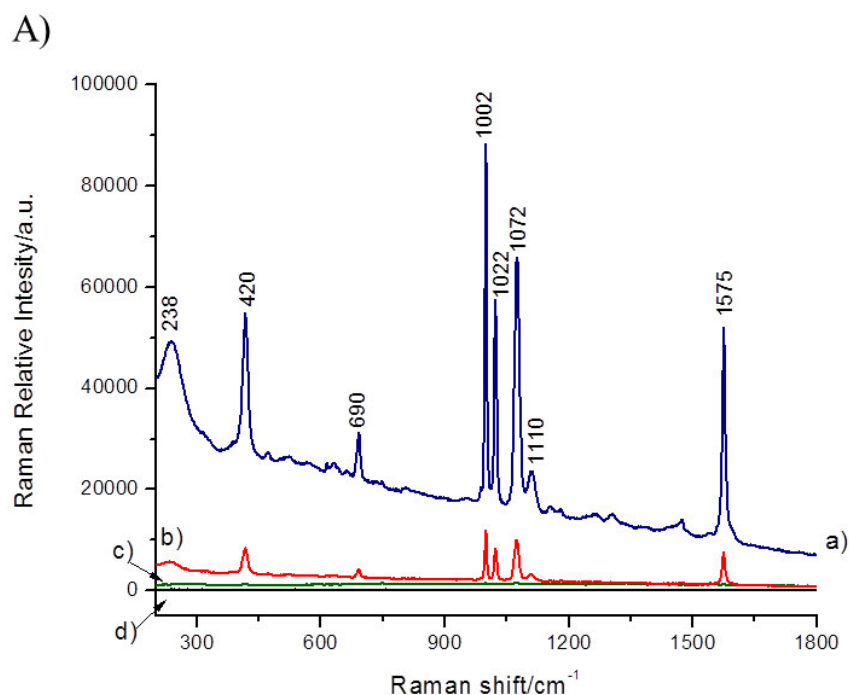


Figure 5.14 FE-SEM pictures of A) an SSV substrate, B) an AgNSs@SSV substrate and C) an AgNSs@SSV substrate functionalized with cysteamine.

5.3.2 Evaluation of the Raman enhancement by means of benzenethiol as Raman probe

The efficiency of the SERS substrates was at first assessed by employing BT as Raman-probe whose Raman bands are well known from the literature [22]. The glass slides coated by an evaporated layer of gold, named hereafter macro-gold, were used as comparison. The analysis on macro-gold confirmed that BT can't be detected by normal Raman spectroscopy (Figure 5.15-d). Instead, its SERS spectrum was recorded on alone or combined nano-materials (Figure 5.15-a-b-c). The typical bands of BT are placed at 1575 (strong), 1072 (s), 1022 (s), 1002 (s), 690 (medium) and 420 (s) cm^{-1} . The band at 238 cm^{-1} is attributed to the interaction between colloidal Ag and ions adsorbed from the preparation solution [23]. In presence of AgNSs bound to SSV substrates (AgNSs@SSV) the observed enhancement was maximum (Figure 5.15-a) and slightly weaker on AgNSs@macro-gold (Figure 5.15-b). Instead, in the case of standing alone SSV substrates very weak and poor signals were obtained (Figure 5.15-c). In order to get high quality spectra, the power of the laser must be increased at least 20 times.



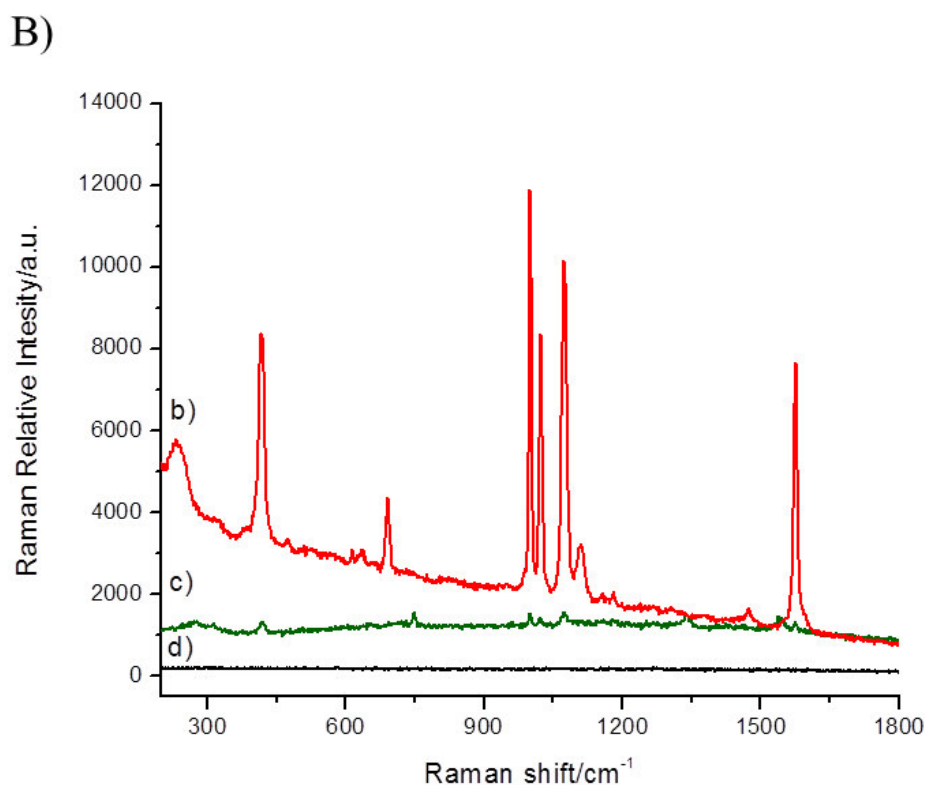


Figure 5.15 A) SERS spectra of a 10^{-2} mM BT solution adsorbed on a) AgNSs@SSV, b) AgNSs@macro-gold, c) SSV and d) macro-gold; B) zoom on the spectra b, c and d ($\lambda_{\text{ex}}=785$ nm, $P=0.05$ mW, $t=1 \times 10$ s).

5.3.3 Detection of madder lake-pigment

The first investigated colorant was madder lake-pigment, using literature as reference for its SERS spectrum [24,25]. Its SERS spectrum was obtained only on AgNSs@SSV, showing the typical bands at: 1567 (weak), 1476 (w), 1331 (s), 1280 (s), 1153 (m), 620 (m), 489 (s), 320 (m) cm^{-1} (Figure 5.16-a). In the case of AgNSs@macro-gold the intensity resulted lower (Figure 5.16-b) up to become undetectable on standing alone SSV (Figure 5.16-c) and macro-gold (Figure 5.16-d). However, even in the optimum enhancement conditions, the quality of the spectra was quite poor.

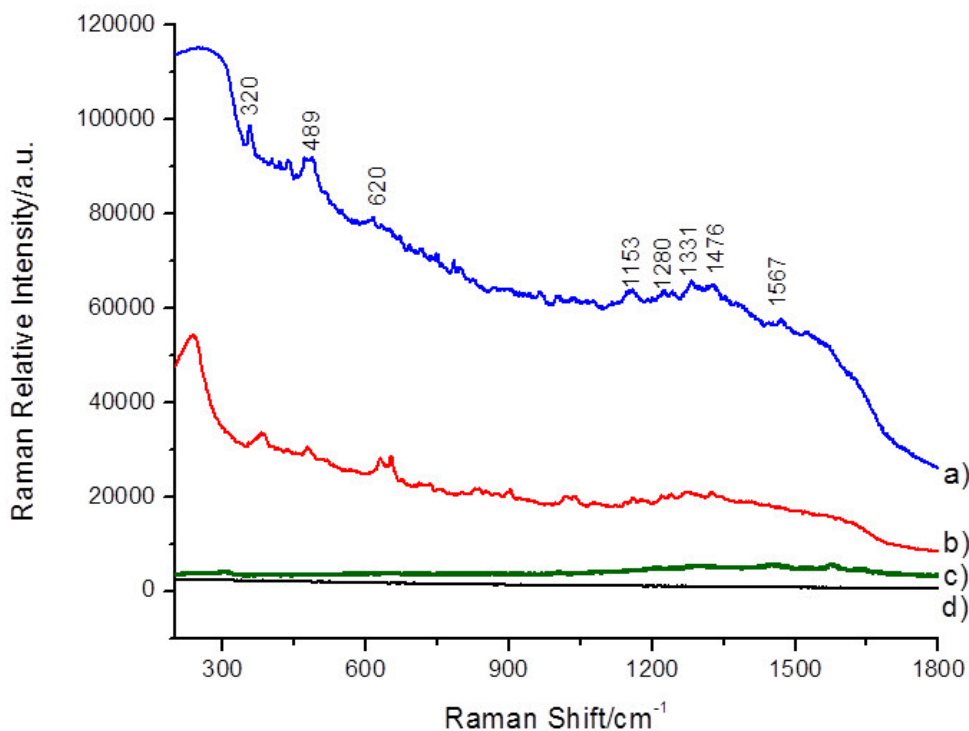


Figure 5.16 SERS spectra of a 10^{-3} M madder lake dispersion adsorbed on a) AgNSs@SSV, b) AgNSs@macro-gold, c) SSV and d) macro-gold ($\lambda_{\text{ex}}=785$ nm, $P=0.05$ mW, $t=1 \times 10$ s).

5.3.4 Detection of cochineal lake-pigment and comparison with pure carminic acid

Figure 5.17 reports the SERS spectra recorded after adsorbing cochineal lake-pigment (CL) on different substrates (see also Chapter 3). SERS spectral data reported in literature were used as reference [23-26]. Also in this case, AgNSs@SSV produced the strongest enhancements (Figure 5.17-a), followed by AgNSs@macro-gold (Figure 6.17-b). The main bands are marked in Figure 5.17: 1530 (w), 1460 (m), 1317 (s), 1226 (m), 959 (w), 732 (m), 580 (w), 470 (m) cm^{-1} . Instead, standing alone SSV generated much weaker spectra which in most cases did not allow the detection of the analyte (Figure 5.17-c). On undecorated macro-gold, CL resulted undetectable (Figure 5.17-d).

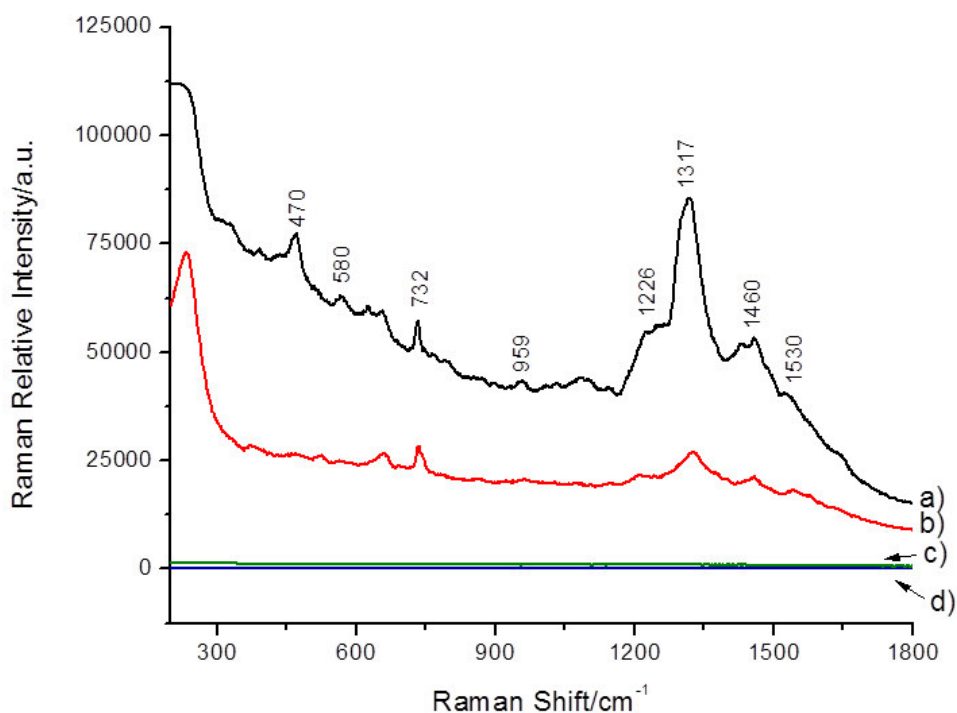


Figure 5.17 SERS spectra of a 10^{-3} M cochineal lake-pigment dispersion adsorbed on a) AgNSs@SSV, b) AgNSs@macro-gold, c) AgNSs@SSV and d) macro-gold ($\lambda_{\text{ex}} = 785$ nm, $P = 0.05$ mW, $t = 1 \times 10$ s).

After the first test on CL, pure carminic acid was investigated to provide a reference for the pure dye molecule [23,24,26]. The main bands are marked in Figure 6.18: 1576 (m), 1451 (m), 1411 (s), 1330 (s), 1224 (w), 1084 (m), 584 (w), 497 (m) and 380 (m) cm^{-1} . AgNSs@SSV produced once again the strongest enhancement (Figure 5.18-a). AgNSs@macro-gold allowed to record a useful spectrum, however with slightly lower sensitivity (Figure 5.18-b) while the standing alone SSV substrates generated a much weaker spectrum (Figure 5.18-c). No signal was recorded on macro-gold (Figure 5.18-d).

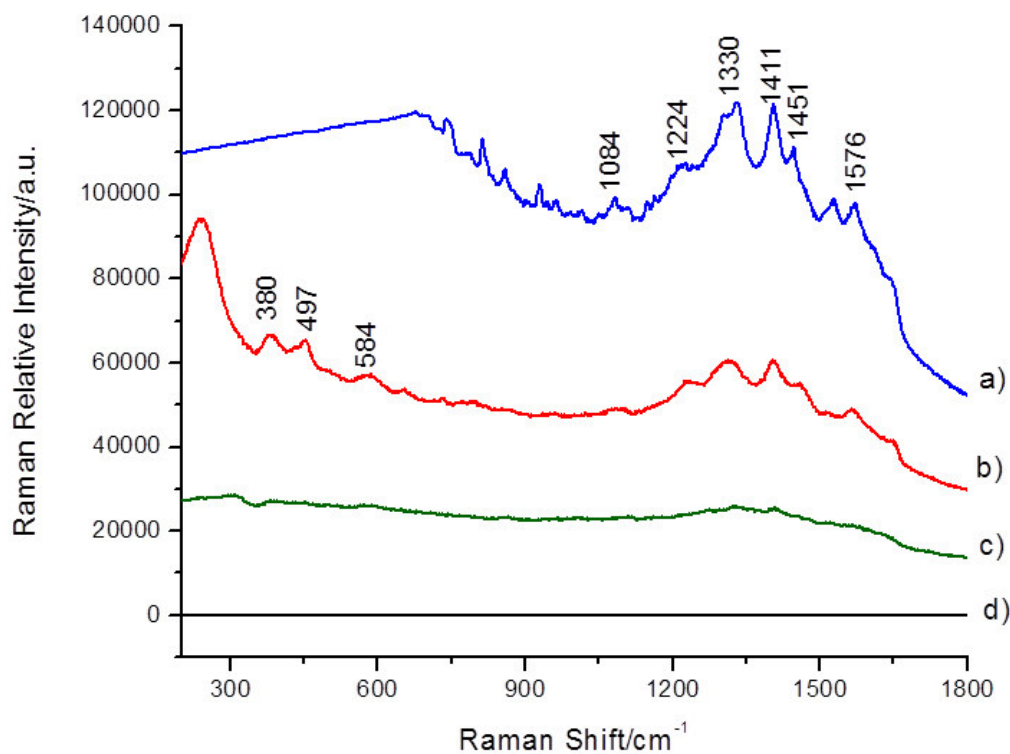


Figure 5.18 SERS spectra of a 10^{-3} M carminic acid solution adsorbed on a) AgNSs@SSV, b) AgNSs@macro-gold, c) SSV and d) macro-gold ($\lambda_{\text{ex}}=785$ nm, $P=0.05$ mW, $t=1 \times 10$ s).

5.3.5 Application to indigo

The last dye here tested was indigo whose SERS spectrum has been reported in literature [27]. Even in this case, the strongest enhancement was observed in the case of AgNSs@SSV (Figure 5.19-a), comparable with AgNSs@macro-gold (Figure 5.19-b). The main bands are found at 1580 (s), 1467 (w), 1313 (m), 1229 (w), 550 (m), 400 (w) cm^{-1} . Even though of a minor intensity, the SERS spectrum of indigo could be recorded also on SSV (Figure 5.19-c). Instead, on plain macro-gold layer, its signal couldn't be detected (Figure 5.19-d).

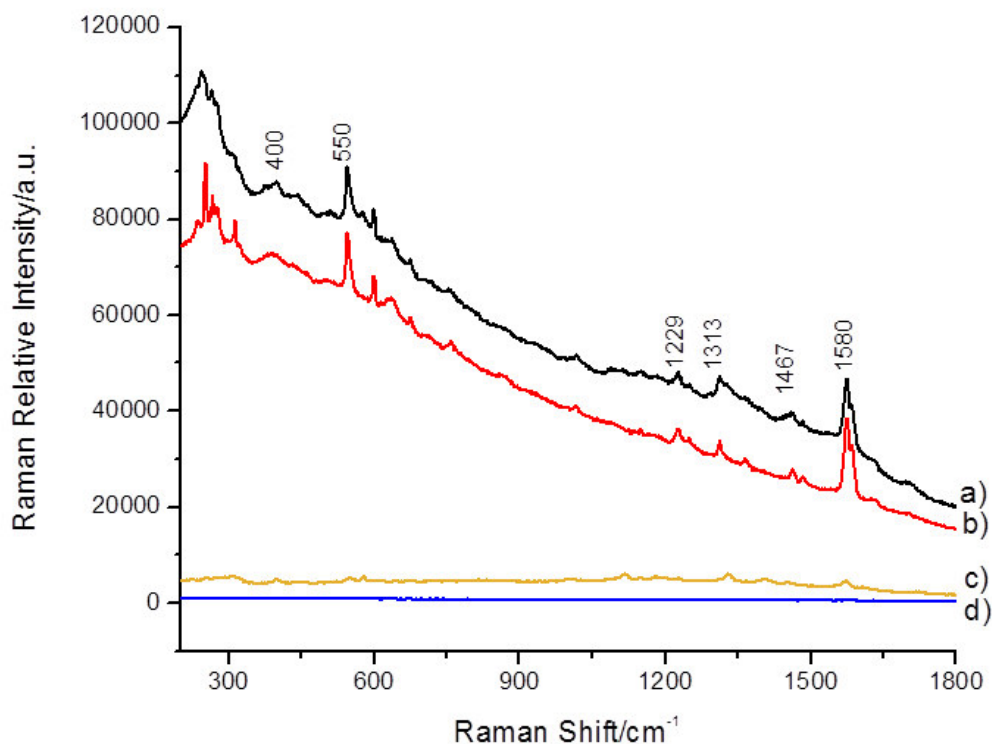


Figure 5.19 SERS spectra of a 10^{-3} M indigo solution adsorbed on a) AgNSs@SSV, b) AgNSs@macro-gold, c) SSV, d) macro-gold ($\lambda_{\text{ex}} = 785$ nm, $P = 0.05$ mW, $t = 1 \times 10$ s).

5.4 Conclusions

On account of the analyses performed, the hierarchical nanostructures AgNSs@SSV proved to generate a dramatic enhancement of the Raman signal, property that makes them extremely sensitive and efficient SERS substrates. Indeed, not only the detection of benzenethiol was successful, but also that of madder and cochineal lakes, complex composite materials, and indigo, a challenging dye. The SERS spectra obtained on AgNSs@macro-gold, even though they can provide high quality spectra, did not result as intense and defined as those recorded on the hierarchical structure. Standing alone SSV were effective only with easily-detectable analyte and using high laser power. Concluding, AgNSs@SSV hierarchical nanostructures show very attracting properties

in view of their possible application for the sensitive detection of artistic dyes. However, taking into account the morphological characteristics of these hierarchical structures, supported on a solid substrate, the preliminary extraction of the analyte from the sample looks necessary. However, thanks to the high sensitivity obtained, very small microvolumes can be analyzed.

References

- [1] N.G. Tognalli, A. Fainstein, E.J. Calvo, M. Abdelsalam, P.N. Bartlett, *J. Phys. Chem. C* **2012**, *116*, 3414.
- [2] S. Mahajan, R.M. Cole, B.F. Soares, S.H. Pelfrey, A.E. Russell, J.J. Baumberg, P.N. Bartlett, *Phys. Chem. C* **2009**, *113(21)*, 9284.
- [3] M. Meneghello, M.Sc. thesis, Università Ca' Foscari Venezia, **2013**.
- [4] S. Mahajan, Ph.D. thesis, University of Southampton, **2008**.
- [5] T.A. Kelf, Y. Sugawara, R.M. Cole, J. J. Baumberg, M. E. Abdelsalam, S. Cintra, S. Mahajan, A. E. Russell, P.N. Bartlett, *J. Phys. Chem.* **2006**, *74*, 245415.
- [6] R.P. Johnson, Ph.D. thesis, University of Southampton, **2011**.
- [7] E. Prodan, C. Radloff, N.J. Halas, P. Nordlander, *Science* **2003**, *302 (5644)*, 419.
- [8] A.S. Dimitrov, K. Nagayama, *Langmuir* **1996**, *12*, 1303.
- [9] J.D. Speed, R.P. Johnson, J.T. Hugall, N.N. Lal, P.N. Bartlett, J.J. Baumberg, A.E. Russell, *Chem. Commun.*, **2011**, *47*, 6335.

- [10] F.M. Huang, D. Wilding, J.D. Speed, A.E. Russell, P.N. Bartlett, J.J. Baumberg, *Nano Lett.* **2011**, *11*, 1221.
- [11] M.E. Abdelsalam, P.N. Bartlett, T. Kelf, J. Baumberg, *Langmuir* **2005**, *21*, 1753.
- [12] B.P. Lloyd, P.N. Bartlett, R.J.K. Wood, *Langmuir* **2015**, *31*, 9325.
- [13] F. Birembaut, N. Perney, K. Pechstedt, P.N. Bartlett, A.E. Russell, J.J. Baumberg, *Small* **2008**, *4(12)*, 2140.
- [14] J.B. Shein, L.M.H. Lai, P.K. Eggers, M.N. Paddon-Row, J.J. Gooding, *Langmuir* **2009**, *25*, 11121.
- [15] M. Silvestrini, P. Ugo, *Anal. Bioanal. Chem.* **2013**, *405*, 995.
- [16] M. Zamuner, D. Talaga, F. Deiss, V. Guieu, A. Kuhn, P. Ugo, N. Sojic, *Adv. Funct. Mater.* **2009**, *19(44)*, 3129.
- [17] H. Schweppe, J. Winter, *Madder and Alizarin, in Artists' Pigments. A Handbook of Their History and Characteristics, Vol. 3* **1997**, 109-142, ed. E.W. Fitzhugh, Oxford University Press, Cambridge.
- [18] H. Schweppe, H. Roosen-Runge, *Carmines, Cochineal Carmine and Kermes Carmine in Artists' Pigments. A Handbook of their History and Characteristics Vol 1* **1986**, 255-283, ed. R.L. Feller, Cambridge University Press, Cambridge.
- [19] H. Schweppe, *Indigo and Woad, in Artists' Pigments. A Handbook of Their History and Characteristics, Vol. 3*, ed. E.W. Fitzhugh, Oxford University Press **1997**, 81-107 London.
- [20] P.N. Bartlett, J.J. Baumberg, P.R. Birkin, M.A. Ghanem, M.C. Netti, *Chem. Mater.* **2002**, *14*, 2199.
- [21] P. Maraffini, Bachelor thesis, University of Southampton, **2010**.
- [22] J. Fontana, J. Livenerec, F.J. Bezaresd, J.D. Caldwell, R. Rendell, B.R. Ratna, *Appl. Phys. Lett.* **2013**, *102*, 201606.

- [23] M.V. Cañamares, J.V. García-Ramos, C. Domingo, S. Sánchez-Cortés, *Vib. Spectrosc.* **2006**, 40, 161.
- [24] M.V. Cañamares, Ph.D. thesis, Universidad Complutense de Madrid, **2005**.
- [25] F. Pozzi, M. Leona, *J. Raman Spectrosc.* **2016**, 47, 67.
- [26] A.V. Whitney, F. Casadio, R.P. Van Duyne, *Appl. Spectr.* **2007**, 61(9), 994.
- [27] S. Bruni, V. Guglielmi, F. Pozzi, *J. Raman Spectrosc.* **2011**, 42, 1267.

Chapter 6

Comparison between different nanomaterials

6.1 Comparison between CuNWs and AuNWs

Two kinds of high aspect ratio nanomaterials were synthesized to be employed as SERS substrates: Cu and Au nanowires. They were decorated with AgNSs to build hierarchical nanostructures in order to maximize the Raman enhancement. Thereafter, the performances of the two substrates were compared in order to understand which was the most efficient metal between gold and copper. AgNSs@AuNWs and AgNSs@CuNWs were compared by employing BT at two different concentration: 10^{-3} and 10^{-5} M (Figure 6.1-A and 6.1-B). The comparison shows clearly that the Raman enhancement induced by AgNSs at AuNWs (Figure 6.1-A-a and 6.1-B-a) is stronger than the one induced at CuNWs (Figure 6.1-A-b and 6.1-B-b). In the case of 10^{-3} M solution, AgNSs@AuNWs produced an intense spectrum which shows the typical bands of BT: 1570, 1105, 1070, 1018, 996, 698 and 412 cm^{-1} (Figure 6.1-A-a) [1]. Instead, the spectrum recorded on AgNSs@CuNWs (Figure 6.1-A-b) presents bands which are remarkably less intense, defined and numerous. Note that the peaks at 1105, 689 and 412 cm^{-1} cannot be detected in this spectrum. When BT is adsorbed from the less concentrate solution (10^{-5} M) it can still be identified on nanostructured gold-based substrates (Figure 6.1-B-a), while this is hardly possible on copper (Figure 6.1-B-b). Therefore, one can conclude that gold represents the most suitable metal to be employed as substrate when decorated with AgNSs. The results obtained agree with what was observed in the literature for the case of nanostructures with different morphology, such as Ag NPs at powdered copper compared to Ag NPs at flat gold, which showed REF of $1.4 \cdot 10^5$ and $8.3 \cdot 10^5$ respectively [2-4].

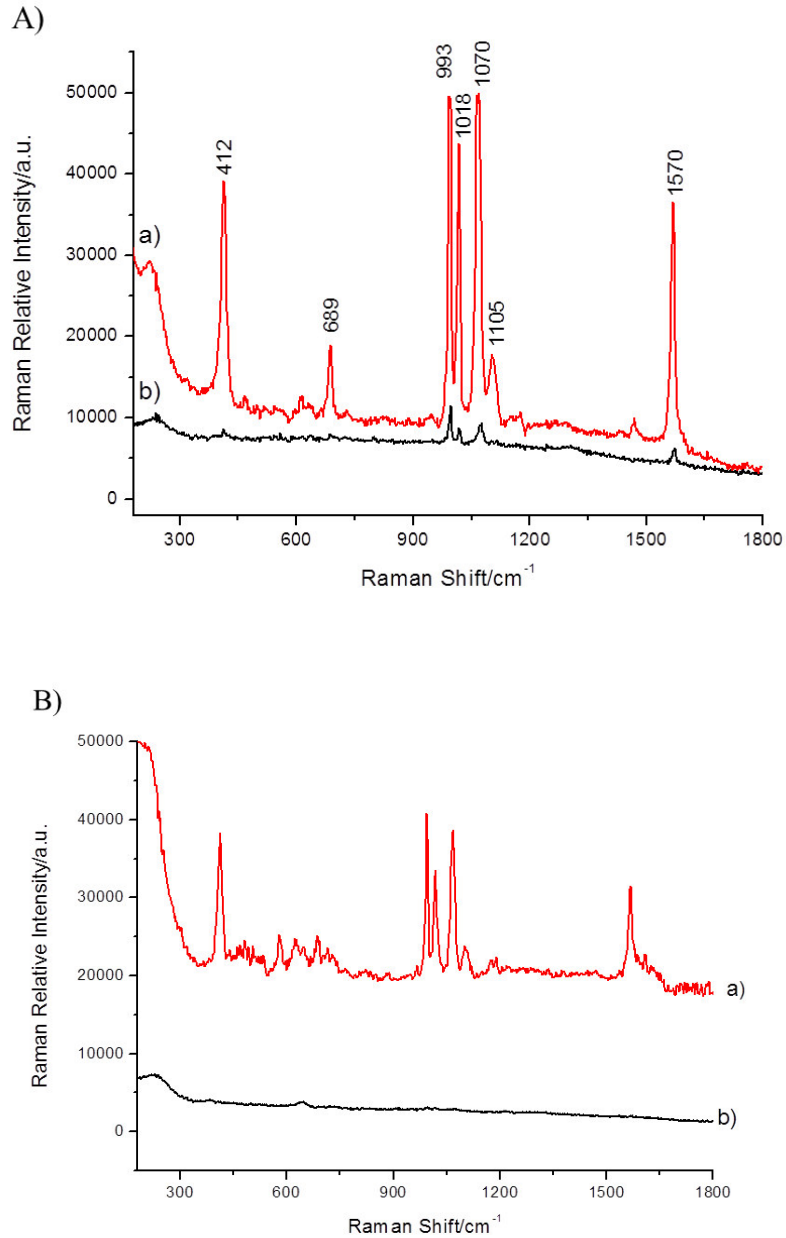


Figure 6.1 Comparison between SERS spectra of A) 10^{-3} M and B) 10^{-5} M BT acquired on a) AgNSs@AuNWs and b) AgNSs@CuNWs ($\lambda_{ex} = 785$ nm, $P = 15$ mW, $t = 3 \times 20$ s).

6.2 AgNSs@AuNWs vs. AgNSs@SSV

Once experimented that gold is the best metal to be coupled to AgNSs, one should compare the different nanostructured surfaces that we have coupled with the AgNSs, namely AuNWs [5,6] and

SSV [7,8]. Figure 6.2 compares the SERS spectra obtained after adsorbing the BT probe from a 10^{-3} mM solution on AgNSs@SSV (Figure 6.2-a), AgNSs@AuNWs (figure 6.2-b) and AgNSs@macro-gold (Figure 6.2-c), respectively. Even though the analyte can be detected on all the three substrates, the enhancement produced by AgNSs@SSV is dramatically increased. This result supports the idea that the presence of an ordered and homogenous substrate, made of cavities repeated periodically and able to host the Ag nanostars is the most suitable option among those examined here, able to maximize the SERS effect.

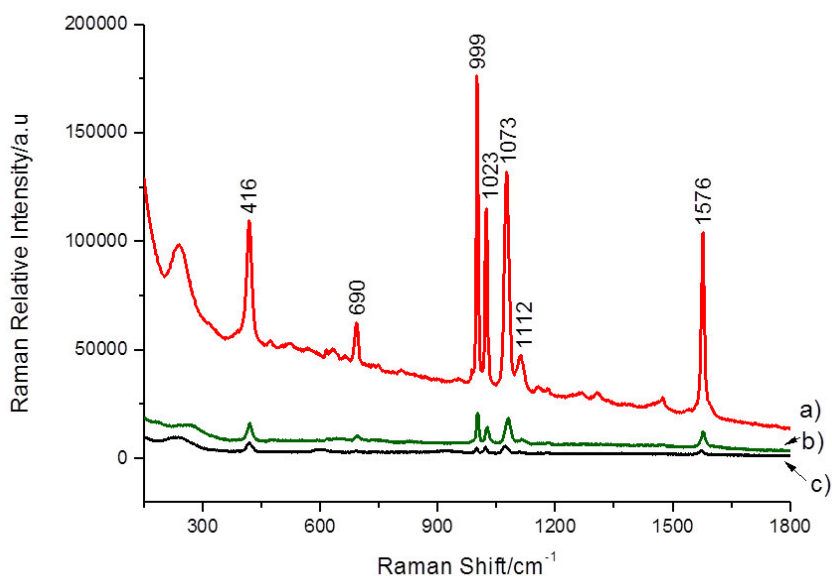


Figure 6.2 SERS spectra of 10^{-2} mM BT solution adsorbed on a) AgNSs@SSV, b) AgNSs@AuNWs and c) AgNSs@macro-gold ($\lambda_{ex} = 785$ nm, $P = 0.05$ mW, $t = 1 \times 10$ s).

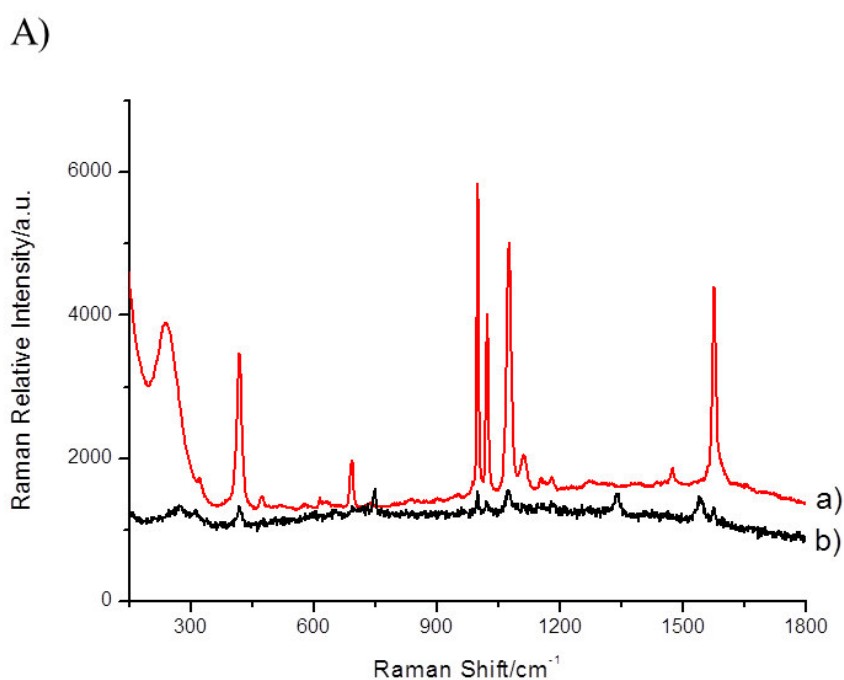
After the collection of the spectra on different SERS substrates and the qualitative comparison of the enhancements, we tried to provide a semiquantitative estimate to compare the performances obtained with the different nanostructures [9]. Using the same instrumentation and assuming that approximately the same number of molecules interact with the laser beam, a relative scale can be obtained by comparing what we named signal ratios (SR), calculated using the following equation:

$$SR = \frac{I_{SERS}}{I_{Raman}} \times \frac{P_{Raman}}{P_{SERS}} \times \frac{t_{Raman}}{t_{SERS}} \quad (6.1)$$

where the intensity I is the band intensity measured at 1072 cm^{-1} [10], P is the laser power and t is the exposure time. The SR values calculated for data shown in Figure 7.2 provided the following sequence: $SR_{AgNSs@SSV} = 1.4 \times 10^5$; $SR_{AgNSs} = 1.9 \times 10^4$; $SR_{SSV} = 6.2 \times 10^3$.

6.3 The performances of 600 and 220 nm SSV

The enhancement produced by the 220 nm size SSV were compared with that caused by the 600 nm size ones. Figure 6.3 compares the two sizes A) standing alone and B) AgNSs decorated SSV. First of all, one can note the entity of the enhancement which resulted around two orders of magnitude in the case of hierarchical structures. Generally the 220 nm SSV gave better results (Figure 6.3-A-a and 6.3-B-a) with respect to the 600 nm SSV (Figure 6.3-A-b and 6.3-B-b). The SERS spectrum recorded with undecorated 600 nm SSV presented weak bands, some of those not belonging to the analyte.



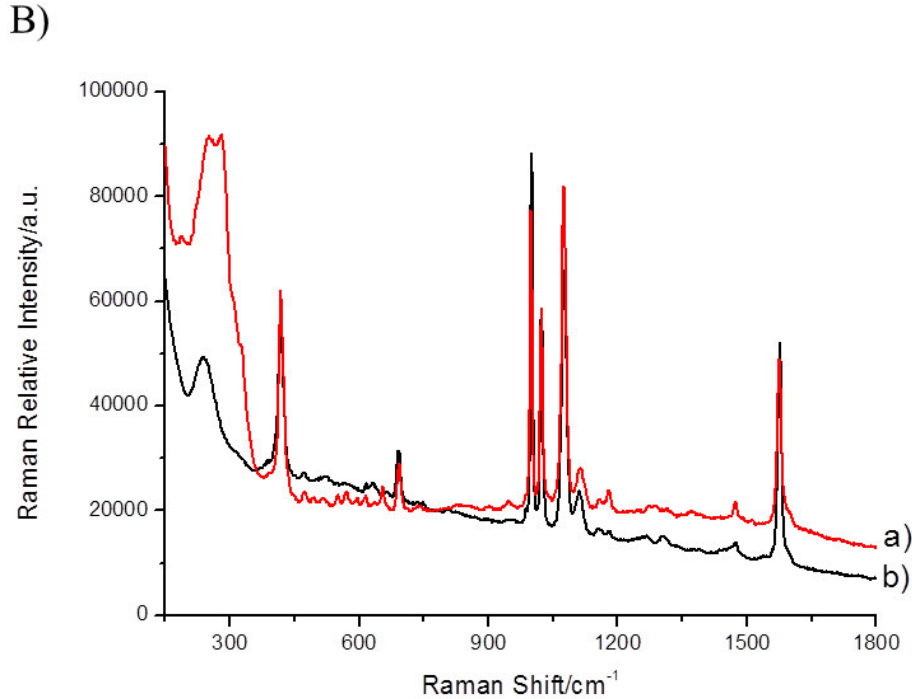


Figure 6.3 A) SERS spectra of a 10^{-2} mM BT solution recorded on a a) 220 nm and b) 600 nm SSV; B) SERS spectra of BT detected on a a) AgNSs@220nmSSV and b) AgNSs@600nmSSV ($\lambda_{ex} = 785$ nm, $P = 0.05$ mW, $t = 1 \times 10$ s).

The SSV with 220 nm cavities were compared with 600 nm SSV in terms of enhancements using CL as test analyte [11]. Figure 6.4 compares SSV of the two sizes, standing alone (A) and AgNSs decorated (B). As before, the first result to note is the further enhancement of the signal observed with the bimetallic structures. Even in this case, 220 nm SSV produced spectra of a better quality. Especially when undecorated (Figure 6.4-A), it was difficult to detect CL on 600 nm SSV (Figure 6.4-A-b) while it resulted easier on 220 SSV (Figure 6.4-A-a). On the contrary, the use of hierarchical structures made of the two sizes of SSV coupled to AgNSs improved in any case the sensitivity of signals, even if, as already described for BT, the 220 nm SSV generated stronger enhancements (Figure 6.4–B-a) with respect to the 600 nm SSV (Figure 6.4–B-b).

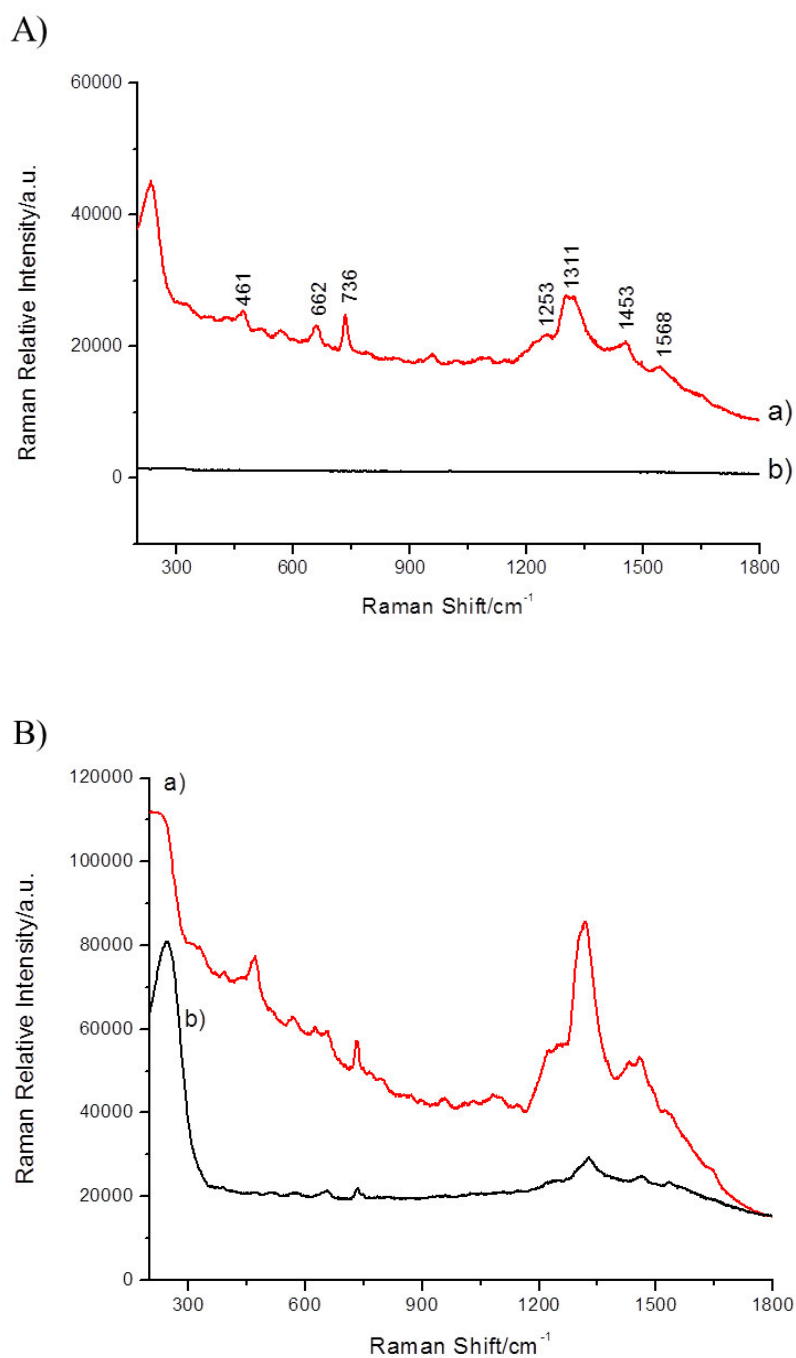


Figure 6.4 A) SERS spectra of a 10^{-3} M CL dispersion recorded on a a) 220 nm and b) 600 nm SSV; B) SERS spectra of CL detected on a a) AgNSs@220nmSSV and b) AgNSs@600nmSSV (λ_{ex} = 785 nm, P = 0.05 mW, t = 1 x 10 s).

Possibly this improvement of the quality of the enhancement is due to the almost perfect match between the dimensions of the nanostars and the 220 nm SSV cavities, when decorated, and a stronger interaction with the analyte, when undecorated.

6.4 Conclusions

The here presented experimental results and their comparison provided useful information on how to produce more and more efficient SERS substrates. Anisotropic nanoparticles (AgNSs) produce a higher Raman enhancement than isotropic nanomaterials (AgNPs); bimetallic hierarchical nanostructures generate a further enhancement (AgNSs@Cu/AuNWs); the best metal to be coupled with silver is gold (AgNSs@AuNWs); ordered gold nanocavities (AgNSs@SSV) represent a highly suitable substrate for silver nanostars, providing the best results when nanocavities match the size of AgNSs (AgNSs@220nmSSV).

References

- [1] J. Fontana, J. Livenerec, F. J. Bezaresd, J. D. Caldwell, R. Rendell, B. R. Ratna. *Appl. Phys. Lett.*, **2013**, *102*, 20160.
- [2] K. Kim, H.S. Lee, *J. Phys. Chem. B* **2005**, *109*, 18929.
- [3] K. Kim, H.S. Lee, *J. Phys. Chem. B* **2005**, *109*, 20731.
- [4] K. Kim, J. Choi, K.S. Shin, *J. Phys. Chem. C* **2013**, *117*, 11421.
- [5] V.P. Menon, C.R. Martin, *Anal. Chem.* **1995**, *67*, 1920.
- [6] P. Ugo, L.M. Moretto, *Template Deposition of Metals*. In C. Zosky (ed.), *Handbook of Electrochemistry*, **2007**, chapter 16.2, Elsevier, Amsterdam, The Netherlands.
- [7] M.E. Abdelsalam, P.N. Bartlett, T. Kelf, J. Baumberg, *Langmuir* **2005**, *21*, 1753
- [8] J.D. Speed, R.P. Johnson, J.T. Hugall, N.N. Lal, P.N. Bartlett, J.J. Baumberg, A.E. Russell, *Chem. Commun.* **2011**, *47*, 6335.
- [9] S. Cintra, M.E. Abdelsalam, P.N. Bartlett, J.J. Baumberg, T.A. Kelf, Y. Sugawarab, A.E. Russell, *Faraday Discuss.* **2006**, *132*, 191.
- [10] V. Guieu, F. Lagugne-Labarthet, L. Servant, D. Talaga, N. Sojic, *Small* **2008**, *4(1)*, 96.
- [11] M.V. Cañamares, J.V. García-Ramos, C. Domingo, S. Sánchez-Cortés, *Vib. Spectrosc.* **2006**, *40*, 161.


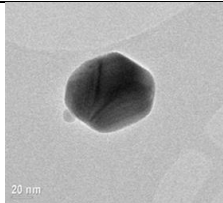
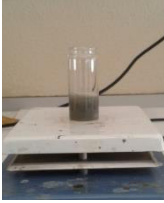
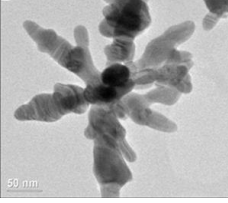
Chapter 7

Concluding remarks

7.1 Final comments and future prospects

The experimental results presented and their discussion and comparison led to significant conclusions, providing useful information about how to produce more and more efficient SERS sensors for diagnostics, conservation and restoration of Cultural Heritage. These tools can be easily applied to micro-samples such as powders, fragments, extracted micro-volumes or cross sections which, in particular, result extremely useful for an exhaustive analysis since they display the multilayered structure of artworks. The obtained SERS sensors can provide quick and reliable information about the materials which compose the analyzed work of art both in laboratory and on-site, even during restoration interventions and monitoring or sampling activities. Table 7.1 summarizes the synthesized nanomaterials which are employed in the preparation of the hierarchical nanostructures listed in Table 7.2.

Table 7.1 Summary of the synthesized nanomaterials.

Nanomaterial	Macroscopic image	TEM/SEM image	Characteristics
Ag nanospheres (AgNPs) (electroless soft template synthesis)			Spherical silver nanoparticles (diameter \approx 60 nm), widely employed as SERS substrate.
Ag nanostars (AgNSs) (electroless soft template synthesis)			Starry-shaped silver nanoparticles (from tip to tip \approx 200 nm) which cause a huge enhancement of the Raman effect.


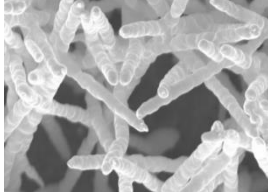

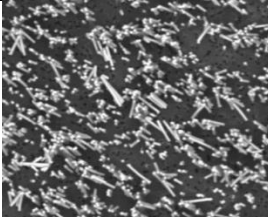

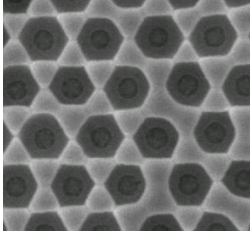
<p>Au nanowires (AuNWs) (electroless hard template synthesis)</p>			<p>High aspect ratio gold nanowires (diameter \approx 80 nm, length 6 μm) which can be functionalized or used as such as SERS substrate.</p>
<p>Cu nanowires (CuNWs) (electrochemical hard template synthesis)</p>			<p>High aspect ratio copper nanowires (diameter \approx 400 nm, length 10 μm) represent a cheaper alternative to AuNWs.</p>
<p>Au sphere segment void surfaces (SSV) (electrochemical hard template synthesis)</p>			<p>Ordered and homogeneous monolayer of spherical cavities (diameter 600 or 220 nm) organized in a beehive structure which can host analytes and other nanomaterials or be used as such as SERS substrate.</p>

Table 7.2 Summary of the hierarchical nanostructures obtained from the above described nanomaterials.

Hierarchical nanostructure	Description
AgNPs@AuNWs	Spherical silver nanoparticles bound to etched gold nanowires in shape of ensembles of nanowires.
AgNSs@AuNWs	Silver nanostars bound to etched gold nanowires in shape of ensembles of nanowires.
AgNSs@CuNWs	Silver nanostars bound to etched copper nanowires in shape of ensembles of nanowires.
AgNSs@SSV	Silver nanostars hosted in SSV with 600 or 220 nm cavities (particle-in-cavity architecture) and bound to their edges.

The successful detection of colorants such as cochineal lake-pigment, madder lake-pigment and indigo by means of these SERS sensors represents a promising result. In detail, we can hypothesize an efficient interaction between the target molecules and the nanomaterials: close to the surface of standing alone AgNSs, in the proximity of the network created by AgNSs@AuNWs or hosted in the cavities of AgNSs@SSV. Certainly, the ability of the nanostructures to create positive interactions with analytes, even of a complex nature, can be exploited in the future preparation of versatile sensors. In particular, the possible development of this study is the refined preparation of AgNSs@220nmSSV with the aim of filling as many cavities as possible with AgNSs, possibly improving the wettability of the SSV [12-14]. Indeed, this kind of hierarchical nanostructures represents the perfect candidate for the production of highly sensitive SERS sensors applicable as diagnostics tools in many contexts.

In some preliminary tests I was able to detect cochineal lake-pigment in cross sections taken from mock-ups by means of concentrated nanoparticles placed directly onto the samples. Even when the opposite analytical protocol was followed, that is a dispersion of the lake adsorbed onto standing alone or hierarchically organized nanomaterials, the results were positive. The expected development of this study is the application of these sensors to real samples in which the concentration of colorants can be extremely low and the presence of other substances, such as pigments, binders and varnishes, can hamper their detection. The experimental results achieved are surely encouraging since complex matrices seem not to interfere in the detection of dyes in real cross sections [15-17]. In particular, within the frame of this research, a detection limit of CL of 0.01 mg/mL was estimated which corresponds approximately to a molar concentration of carminic acid of $8 \cdot 10^{-6}$ M. Such a LOD, should be low enough for most real cases [18], but the difficulty of analyzing an aged artwork which underwent many restoration interventions and the natural degradation of the materials across the centuries can create unexpected issues. Moreover, it is rather difficult to predict the exact quantity of colorants that can be found from case to case since it is

highly variable and no specific indications about the amount of dyes is reported in historical sources [19]. The best possible approach is to assay each case in order to evaluate if it is necessary to extract the investigated colorant or it is more convenient to apply directly the nanomaterials onto the sample.

Thinking to practical applications of these nanomaterials for Cultural Heritage diagnostics purposes the AgNSs alone can be easily applied to enhance Raman signal from cross sections. Even if not tested yet, also metal nanowires, alone or in connection with AgNSs can be applied in a similar way since NWs provide stable colloidal dispersions. Because of the morphological characteristics of these hierarchical structures, supported on a solid substrate, the preliminary extraction of the analyte from the sample looks necessary. However, thanks to the satisfactory sensitivity obtained, very small microvolumes can be analyzed. In principle, these sensors can be employed not only for the detection of dyes and lake-pigments, but also for protein-based binders. The hierarchical structures can undergo an immuno/chemical functionalization for SERS detection of protein materials such as collagen, casein, egg yolk and albumen. After the functionalization of the nanomaterials with suitable thiols [20,21], such as cysteamine or thioctic acid, one can establish amide bonds with specific antibodies, labelled by a Raman-probe, able to bind selectively the target proteins (e.g. IgY or albumin present in the egg tempera) [22,23]. If the key-lock bond between the antibodies and their antigens occurs, it can easily be detected by SERS [24]. This experimental setup could be organized with a lateral flow immunoassay (LFIA) approach, creating a fast and easy-to-use sensor [25].

References

- [12] F.M. Huang, D. Wilding, J.D. Speed, A.E. Russell, P.N. Bartlett, J.J. Baumberg, *Nano Lett.* **2011**, *11*, 1221.

- [13] B.P. Lloyd, P.N. Bartlett, R.J.K. Wood, *Langmuir* **2015**, *31*, 9325.
- [14] F. Birembaut, N. Perney, K. Pechstedt, P.N. Bartlett, A.E. Russell, J.J. Baumberg, *Small* **2008**, *4(12)*, 2140.
- [15] A. Idone, M. Aceto, E. Diana, L. Appolonia, M. Gulmini, *J. Raman Spectrosc.* **2014**, *45(11-12)*, 1127.
- [16] K. A. Frano, H. E. Mayhew, S.A. Svoboda, K.L. Wustholz, *Analyst* **2014**, *139*, 6450.
- [17] K. Retko, P. Ropreta, R.C. Korošec, *J. Raman Spectrosc.* **2014**, *45(11-12)*, 1140.
- [18] M.V. Cañamares, J.V. García-Ramos, C. Domingo, S. Sánchez-Cortés, *Vib. Spectrosc.* **2006**, *40*, 161.
- [19] C. Cennini, *Il libro dell'arte*, end of the 14th century.
- [20] M. Silvestrini, P. Ugo, *Anal. Bioanal. Chem.* **2013**, *405*, 995
- [21] J.B. Shein, L.M.H. Lai, P.K. Eggers, M.N. Paddon-Row, J.J. Gooding, *Langmuir* **2009**, *25*, 11121.
- [22] F. Bottari, P. Oliveri, P. Ugo, *Biosens. Bioelectron.* **2014**, *52*, 403.
- [23] C. Gaetani, G. Gheno, M. Borroni, K. D. Wael, L. M. Moretto, P. Ugo, *Electrochim. Acta* **2019**, *312*, 72.
- [24] G. Sciutto, L. Litti, C. Lofrumento, S. Prati, M. Ricci, M. Gobbo, A. Roda, E. Castellucci, M. Meneghetti, R. Mazzeo, *Analyst* **2013**, *138*, 4532.
- [25] G. Sciutto, M. Zangheri, L. Anfossi, M. Guardigli, S. Prati, M. Mirasoli, F.D. Nardo, C. Baggiani, A. Roda, *Angew. Chem.* **2018**, *130(25)*, 7507.

Appendix A

Cochineal lake-pigment

Lakes are coloring agents quite challenging to be analyzed in painting media due to their composite nature. Indeed, they can be defined as complex pigments composed by an organic dye adsorbed onto solid particles of inorganic salts. Particularly important examples of this variety of pigments are represented by the anthraquinone-based red lakes such as cochineal, madder and kermes lake. Among the red lakes, cochineal lake (CL), also known as carmine or crimson lake, is particularly important for the scope of this thesis. Being a composite material, the analysis of CL is rather difficult and enhancing the Raman becomes necessary in most cases. On account of that, it was chosen as analyte for the experimental part described in this research work.

Let us now describe this class of colorants briefly. Anthraquinones, the most numerous group of natural quinones, are organic compounds derived from the structure of anthracene, a polycyclic aromatic hydrocarbon made of three fused benzene rings, with the substitution of two methine groups =CH- with keto groups -C=O in position 9 and 10 (Figure 1A) [1]. Due to this substitution, the central aromatic ring becomes a cyclic conjugated dione which is fundamental to determine the chromatic properties of anthraquinones, defined as chromophores.

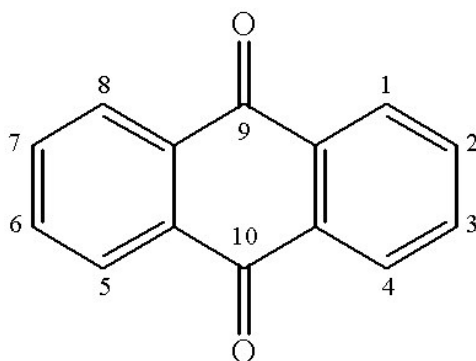


Figure 1A Scheme showing the general structure of an anthraquinone with the carbon numbering.

The chromatic properties of these molecules are widened by the possibility of substituting the hydrogens of the methine groups with auxochrome functions able to modify the both the wavelength and the intensity of absorption of the chromophores. They are characterized by lone pairs of electrons that can extend the conjugated system by resonance. In the case of anthraquinones the substitutions are operated mainly by hydroxyl functions and may occur in eight different positions. This causes a deepening of the color from red to dark brown, especially when the substitution occurs in α position with respect to the chromophore groups. Moreover, hydroxyl groups together with the carbonyl groups are fundamental to establish an interaction with an inorganic substrate. Metal cations behave as an acceptor or Lewis base, interacting with the lone pairs of electrons of the ligands, donors or Lewis acids. Therefore, establishing some coordination bonds, the cation get chelated in the structure created by the ligands around it [2]. According to the kind of metal and its oxidation state it was possible to obtain lakes of different colors and shades.

The most abundant molecule responsible for the color of CL is carminic acid ($C_{22}H_{20}O_{13}$), an anthraquinone with four hydroxyl groups, one methyl group and a carboxylic function, naturally found in form of glycoside. Thanks to the coloring properties of carminic acid (see Figure 1.2-a, Chapter 1), cochineal has long been used as colorant, both alone for dyeing textiles and adsorbed on particles to produce the lake pigment. Cochineal dye was first used in Mexico by the Aztec and imported in Europe in the 16th century during the Spanish conquest, being obtained from scale insects or cochineals (*Dactylopius coccus*) which thrive on cacti [3]. Due to its better coloring performances, cochineal substituted kermes lake in the Old World [4] and started to be cultivated in many areas, until when the artificial synthetization of carminic acid diminished the exploitation of the natural one [5]. The colorant used to be extracted from the dried insects by boiling and then it was fixed by complexation on the surface of an inorganic substrate, typically $KAl(SO_4)_2 \cdot 12H_2O$ (see Figure 1.2-b, Chapter 1). During this process, carminic acid interacts with the aluminum cation

generating a complex. The hydroxyl groups of carminic acid undergo deprotonation to interact with the metal [6].

References

- [1] P.H. Patel, *Handbook of Textile and Industrial Dyeing Principles, Processes and Types of Dyes Volume 1* **2011**, p. 395, Woodhead Publishing.
- [2] P. Atkins, L. Jones, *Chimica generale* **1992**, Zanichelli Ed., Bologna.
- [3] H. Schweppe, H. Roosen-Runge, *Carmines, Cochineal Carmines and Kermes Carmines in Artists' Pigments. A Handbook of their History and Characteristics Vol 1* **1986**, 255-283, ed. R.L. Feller, Cambridge University Press, Cambridge.
- [4] J. Mills, R. White, *Organic material in museum objects* **1999**, 2nd ed. Oxford, Butterworth Heinemann.
- [5] P. Allevi, M. Anastasia, S. Bingham, P. Ciuffeda, A. Fiecchi, G. Cighetti, M. Muir, A. Scala, J. Tyman, *J. Chem. Soc., Perkin Trans.* **1998**, 1, 575.
- [6] M.V. Cañamares, M. Leona, *Lasers in the Conservation of Artworks-Castillejo et al. (eds)* **2008**, Taylor & Francis Group, London.

Appendix B

Madonna della Misericordia: visual and non-invasive analyses

In this Appendix, visual and non-invasive analyses performed on the *Madonna della Misericordia* are reported as completion of Chapter 2- Part B, where one can find the result obtained from the sampled cross sections.

As required by the analytical sequence [1], the first examination of a painting is the visual one. This analysis revealed many conservation issues (losses of color, woodworm holes, etc.) and evidence of the past restoration interventions (Japanese paper on cracks, re-paintings, etc.) carried out in 1896 [2] and in 1951 [3] (Figure 1B).

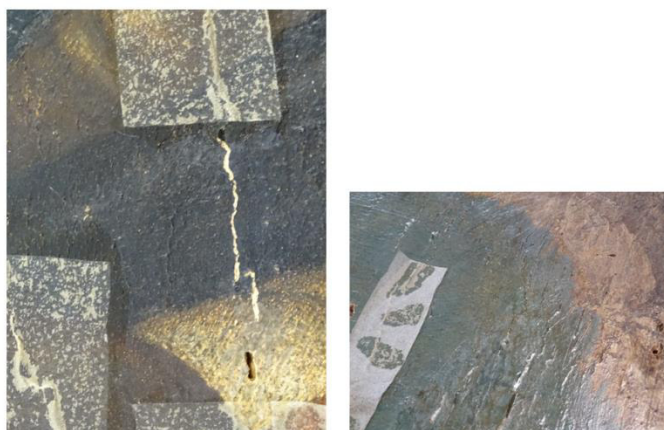


Figure 1B Picture showing some of the conservation issues of the *Madonna della Misericordia*: cracks, losses of color, lifting of the paint layer, woodworm holes.

Thereafter, IR reflectography was carried out, revealing the presence of well-defined underdrawings. Figure 2B shows the detail of one of the two kneeling ladies: her image was accurately drawn before painting and particular attention was given to the pearls of the necklace, her eyes and the voile which covers her hair.

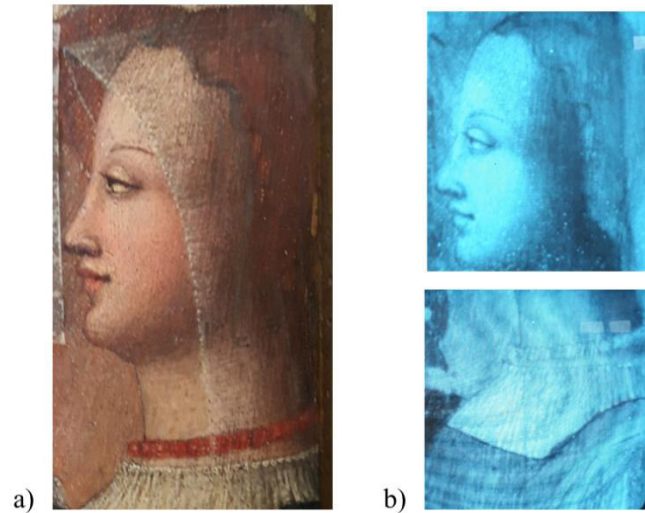


Figure 2B a) Detail of one kneeling lady and b) its IR reflectography image which underlines the presence of precise underdrawings (pearls of the necklace, eyes, voile).

The observation at UV light revealed the accurate location of many re-paintings which appears darker than the original paint and of a thick layer of restoration varnish characterized by the typical yellowish fluorescence [1] (Figure 3B).

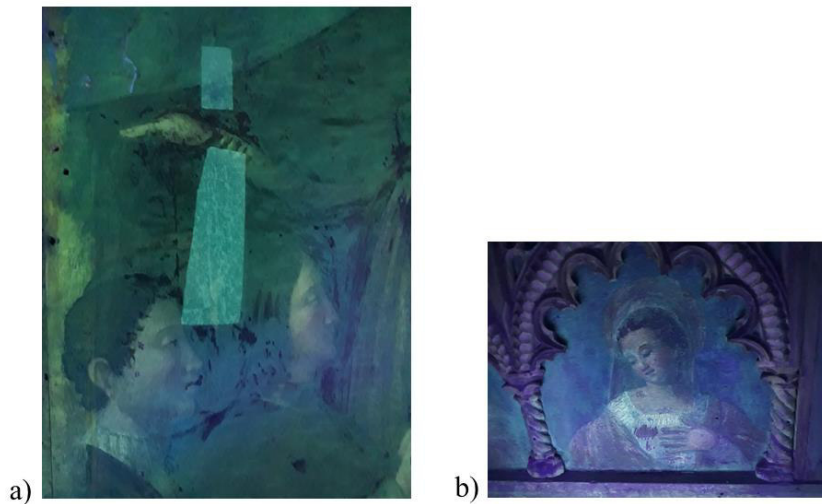


Figure 3B Detail of a) the two gentlemen and b) Santa Caterina in the *predella*: several dark areas indicate the position of re-paintings and the yellowish fluorescence is due to the presence of restoration varnish.

After these assays, some areas of interest of the painting were examined by optical microscopy in reflected light. The repainted details were easily recognized by examining the different kinds *craquelure*: the original paint shows an homogeneous network of shell-like cracks (Figure 4B-a) while the retouched details, plastered and repainted, present a scratched surface to mimic the aged pictorial layer [1] (Figure 4B-b).

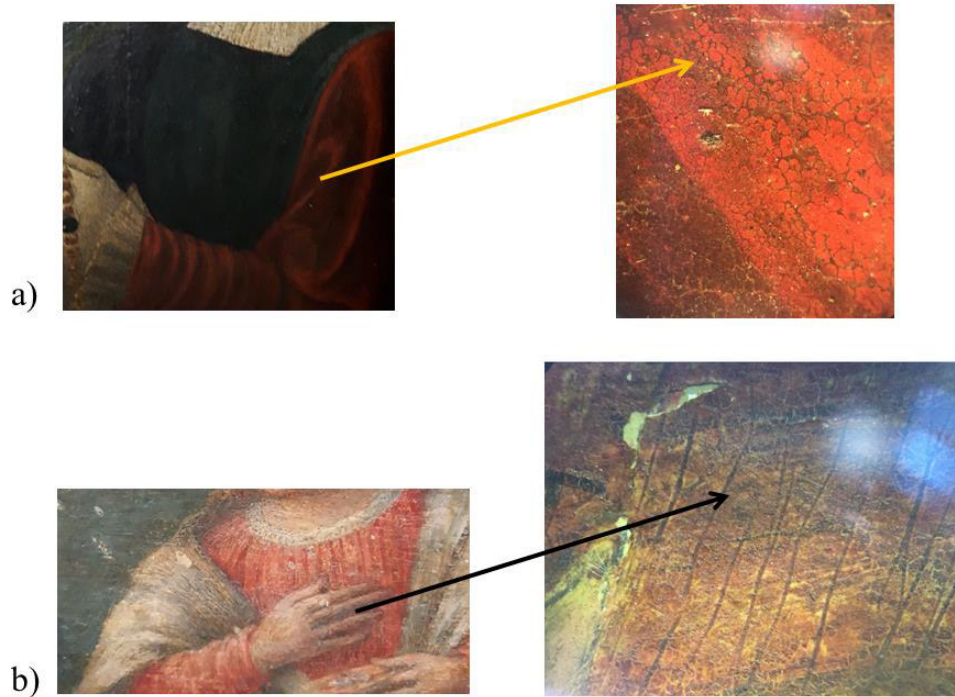


Figure 4B *Craquelure* of a) the original pictorial layer characterized by shell-like cracks and of b) a plastered detail where the ageing of the paint layer was simulated by scratches.

References

- [1] D. Pinna, M. Galeotti, and R. Mazzeo, *Scientific examination for the investigation of paintings. A handbook for restorers* **2011**, Centro Di Firenze, Italy.
- [2] C. Ricci, *La R. Galleria di Parma* **1896**, L. Battei, Parma.
- [3] L. Fornari-Schianchi, Galleria Nazionale di Parma, *Catalogo delle opere dall'antico al Cinquecento* **1997**, F.M. Ricci, Milano.

Acknowledgements

The morphological characterization of nanomaterials and nanoparticles was carried out thanks to the experimental assistance of Prof. Patrizia Canton, University Ca' Foscari & Electronic Microscopy Center "Giovanni Stevanato", Venice, Italy.

Dr. Lucio Litti and Prof. Moreno Meneghetti are thankfully acknowledged for their assistance in the performance of Raman and SERS analyses and for the implementation of the BEM calculations, supported by Cloud.Veneto (<http://www.cloudveneto.it>) and by the Computational facilities at the Chemical Sciences Department of the University of Padua, Italy.

The deposition of Cu nanowires was carried out thanks to the useful collaboration of Margherita Longoni and Dr. Angela Maria Stortini (University Ca' Foscari of Venice, Department of Molecular Sciences and Nanosystems) while Dr. Lavinia de Ferri and Prof. Giulio Pojana (University Ca' Foscari of Venice, Department of Philosophy and Cultural Heritage) are gratefully thanked for SERS measurements.

Nadir S.r.l. (Italy) (Dr. Paolo Scopece, Dr. Marco Scatto and Dr. Emanuele Verga Falzacappa) is gratefully acknowledged for providing instrumentation and assistance for plasma etching treatments on AuNWs with Nadir Stylus Plasma equipment.

Dr. Eleonora Balliana and Prof. Elisabetta Zendri (Department of Environmental Sciences, Informatics and Statistics, University Ca' Foscari of Venice) are thanked for the assistance in the preparation of cross sections.

I would like to thank Dr. Ines Agostinelli for her valuable supervision of my traineeship at the restoration laboratory of the National Gallery of Parma, during which I learned the main restoration techniques and I collected real samples from different works of art. I am really grateful to her for hosting me in her laboratory, sharing pleasant work and leisure time.

Prof. Philip N. Bartlett, Prof. Andrea E. Russell and all the researchers of the group of electrochemistry at the Department of Chemical Sciences, University of Southampton, United Kingdom, are thankfully acknowledged for the experimental assistance in the preparation of SSV substrates and for SERS measurements. In particular, I would like to thank Prof. Bartlett for hosting me in his group, where I met awesome people and I learned a lot.

I would like to give special thanks to my research group in Venice: Prof. Ligia Maria Moretto, Prof. Emilio Orsega, Prof. Maria Antonietta Baldo, Dr. Najmeh Karimian, Dr. Sabrina Fabris helped me every day of the Ph.D. and made this life experience enjoyable.

I would like to thank all my colleagues, Margherita Donnici, Maria Carmen Villoslada, Giulia Moro, Davide Campagnol, Thomas Scattolin, Claudio Costantino, Nicola Ceolotto, Sara Gandolfi, Roberto Sole, Cristina Pizzolitto, Giacomo Berton, Alessandro Bellè, Elisa Casagrande, Simone Cailotto, Lodovico Agostinis, Andrea Morandini, Chiara Gaetani, Giada Bedendi, Francesca Di Turo, Alessia Artesani and still many others with whom I shared unforgettable experiences.

I gratefully thank the coordinators of the Ph.D. in Chemistry, Prof. Alessandro Scarso and Prof. Barbara Milani, all the professors, technicians and the administrative staff (especially Francesca Guidi, Laura Oddi and Teresa Bettin) of University Ca' Foscari of Venice and University of Trieste who worked hard to make possible this course of study.

Special thanks to my parents, Vincenzo and Donatella, my siblings, Maristella and Samuele, my grandmothers, Ida and Rita, my friend Marco and my partner Fabrizio who have stood by my side in every moment, either bright or dark.

The last but not the least, my deepest gratitude is for my supervisor, Prof. Paolo Ugo, without whose help nothing of this would have been possible. I thank him for his teachings, his patience, his trust and, above all, for his humanity.